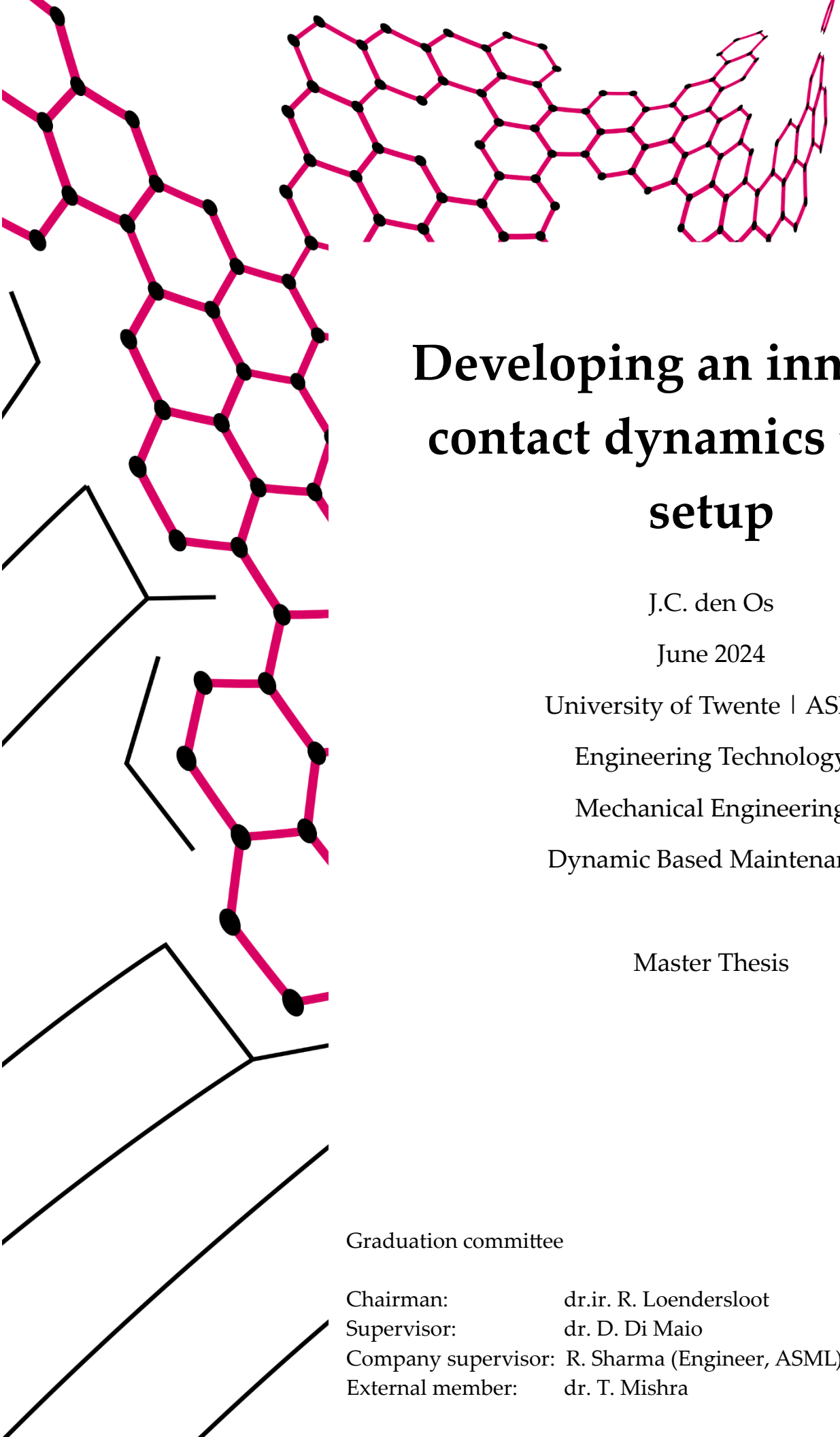

Developing an innovative contact dynamics testing setup

J.C. den Os

June 2024

University of Twente | ASML

Engineering Technology

Mechanical Engineering

Dynamic Based Maintenance

Master Thesis

Graduation committee

Chairman:	dr.ir. R. Loendersloot
Supervisor:	dr. D. Di Maio
Company supervisor:	R. Sharma (Engineer, ASML)
External member:	dr. T. Mishra

Summary

In order to improve the coherency between the current numerical models used by ASML and the constructed lithography machines, an experimental framework to extract relevant contact properties is constructed. The designed experimental setup is unique due to the ability to measure custom designed surface areas up to 1500 mm^2, while being able to apply a multitude of loading conditions. By adding a custom data filtering scheme, for each loading condition the contact properties of a flat on flat contact can be determined. The experimental data are used to conduct a comparative study, where the effects of contact pressure, contact surface area, tangential loading conditions on the contact stiffness, dissipated energy and friction coefficient is investigated. The trends observed correspond with theory found in literature, and the origin of the multiple trends within contact stiffness, friction coefficient and dissipated energy is discussed. In conclusion, this research showed the development of a contact dynamics testing setup, which by means of experimental data analysis is able to extract the contact properties of comparatively large contact surfaces. To further increase the accuracy of the testing device, iterations with regards to the contact alignment and load delivery should be performed.

Nomenclature

ΔE	Total change in energy
ΔU	Change in potential energy
ΔV	Change in kinetic energy
δ_{max}	Maximum deflection
ϵ	Shear correction factor
ζ	Damping ratio
η	Modal coordinate
θ	Phase shift
κ	Longitudinal correction factor
μ_f	Friction coefficient
$[\Phi]$	Modal matrix
$\{\Psi\}$	Numerical modal vector
ω_d	Damped natural frequency
ω_n	Natural frequency
A	Displacement amplitude
$A(f)$	Accelerance in the frequency domain
autoMAC	Modal Assurance Criterion between modal vectors of one system
c	Damping coefficient
E	Modulus of elasticity
EMA	Experimental Modal Analysis
FACT	Freedom and Constraint Topology
FEA	Finite Element Analysis
FEM	Finite Element Method

FFT	Fast Fourier Transformation
FRF	Frequency Response Function
F_{fri}	Friction force
F_n	Normal force applied by one spring plunger
I	Moment of inertia
$[K]$	Stiffness matrix
k_t	Tangential contact stiffness
LDV	Laser Doppler Vibrometer
$[M]$	Mass matrix
$M(f)$	Mobility in the frequency domain
MAC	Modal Assurance Criterion
MPC	Multiple Point Constraint
N_0	Normal load
s	Sliding distance
SDOF	Single Degree of Freedom
s	Sliding distance
SLDV	Scanning Laser Doppler Vibrometer
x	Generalised system coordinate
x_{rel}	Relative displacement
$\dot{Y}(f)$	Measured velocity
$\ddot{Y}(f)$	Measured velocity

Contents

Chapter 1

Introduction & objective

ASML produces lithography machines which are used by its clients to produce semiconductors. The movement of the internal components produces a significant amount of energy in the form of structural vibrations, which is ultimately transferred into the frame of the machine. These vibrations introduce a sliding motion into the joints used to assemble the machine, which leads to friction and energy dissipation between the two jointed surfaces. To achieve a high accuracy in producing semiconductors, it is paramount that these vibrations and their influence on the structure are correctly modelled to achieve a high correlation between simulations and assembled machines. Predicting these motions, friction forces and the amount of dissipated energy within these joints is of great importance, since these properties greatly affect the dynamic behaviour of the joint and therefore the structure itself. If this dynamic behaviour is not accurately modelled, the discrepancy between simulation and assembled machine can be large, which may result in unwanted dynamics and negatively impact the performance of the machine. In the worst-case scenario, inaccurately modelled joint dynamics may result in failure and downtime of the entire machine.

Currently, contact models based on Hertzian contact theory are used to derive the contact properties. However, since these Herzian-based models are primarily applicable to point or line contacts, these models are not applicable for all load cases experienced in the current assemblies. The friction due to the sliding of surfaces in the structure introduces strong non-linear behaviour, which is exceedingly difficult to capture with theoretical models alone. To accurately describe the non-linear behaviour, the need arises to create contact models which are able to replicate the physical phenomena within the joint, and predict the overall dynamic behaviour of the system. Typically, contact parameters used in such contact models are the friction coefficient, damping coefficient and contact stiffness [1]. These parameters can be extracted from a hysteresis curve, which is considered by the academic field as the most representative way of displaying and investigating the underlying contact dynamics between two surfaces [2]. The hysteresis curve shows a load versus deflection curve for an oscillating surface under cyclic load, where the friction force between the two surfaces is plotted against the relative displacement. The aim of this thesis is to create an experimental testing device that is able to measure this hysteresis curve for a wide range of loading and interface conditions. These hysteresis curves will consequently be used to extract the contact stiffness, dissipated energy and friction coefficient, from which a better contact model can be constructed for various joint designs. This predictive behaviour of designed joints will ultimately aid to the improvement of the design and operation of the lithography machines produced by ASML.

Objective

The main objective of this research is to create an experimental framework in which different configurations of large, clamped connections can be measured. Current research focuses primarily on small contact interfaces, in the order of 10 mm^2, however it is unclear if the contact properties extracted from these small surfaces can be extrapolated to larger contact surfaces to extract and predict the contact properties accurately. The experimental framework should extract the relevant contact properties from the clamped connect, which can then be used as a numerical input to improve the accuracy of dynamic simulations. Additionally, the experimental setup should be designed and validated, such that the validity of the resulting contact properties can be verified with existing models.

To achieve this objective, the main research is formulated as:

How can a contact surface be designed, such that the tangential stiffness, dissipated energy and friction coefficient can be predicted accurately to improve existing contact models?

To answer the research question, this thesis will answer the following sub-questions:

1: How can a testing setup be designed, which reliably produces a dominant single degree of freedom motion, and is able to accurately measure a sliding contact?

2: How can a framework be designed, which is able to extract the relevant contact parameters from experimentally gathered contact interface data?

3: How are the joint contact parameters affected by the loading conditions, based on data gathered from the constructed testing device and experimental framework?

To answer these questions, this thesis is divided into multiple chapters. Chapter two elaborates on the current research in the field of contact dynamics, and what type of devices are constructed to measure the contact properties. Chapter three presents the design and validation of the test setup which will be used to perform the desired experiments. In chapter four the design of experiments and post-processing of the measured data will be discussed. Chapter five will subsequently elaborate on the constructed hysteresis curves and how the desired parameters are extracted from these curves. Lastly, chapter six will perform a more detailed analysis where the effect of varying loading and surface area on the contact parameters will be determined.

Chapter 2

Literature review

The following chapter reviews relevant research into the field of contact dynamics and non-linear interfaces. It will first give an insight in the industrial relevance of this research field, and what this research field tries to accomplish. Then, an overview of testing devices from different institutes is presented to illustrate the current development of this field. It will then elaborate on the paper which is the main inspiration for this thesis and what adaptations are made to dive deeper into the field of contact dynamics. Finally, the chapter will conclude with providing relevant background theory used in this research.

2.1 Industrial relevance

In engineering, the vibrations within structures have always been a concerning subject when designing and using a machine or technology. This is largely because of the associated damage and disturbances experienced by the structure due to induced vibrations. In time, a considerable understanding of the physics behind vibrations within structures has been acquired, and modelling techniques have been developed to understand the effect of vibrations on for example motors, vehicles and structures [3]. Linear models can be used to predict the vibration pattern in continuous materials, however when introducing joints into the system several non-linear characteristics arise. Furthermore, in typical vibration testing the excitation is often kept in the linear regime, where linear models are applicable. However, under actual service loads also non-linear effects may be present in the material and joints. An example of this effect is given in Figure 2.1.1b where the resonance frequency of the mode shape of the jointed turbine casing, depicted in Figure 2.1.1a, decreases with increasing load.

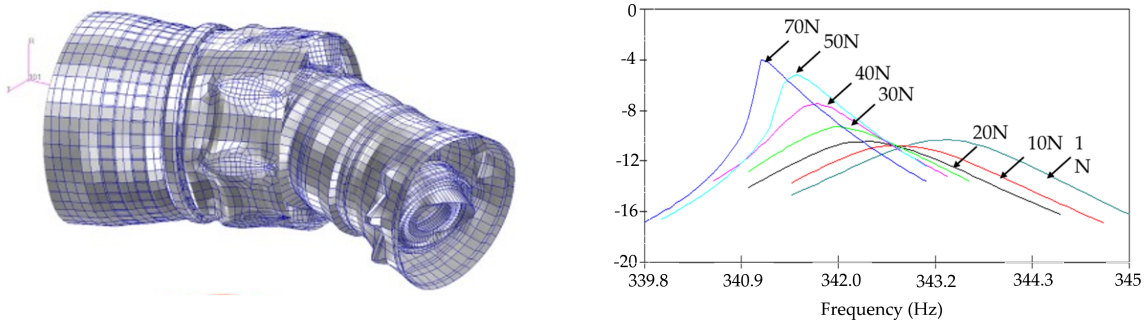

(a) Mode shape of turbine casing

(b) Diminishing resonance frequency

Figure 2.1.1: Evidence of non-linearity with increasing load [3]

To correctly model the influence of joints on a structures dynamics still poses a major challenge, and it even has been proven that many conventional joints possess highly unrepeatable dynamic characteristics, for example when disassembling and consecutively reassembling the joint [3]. It has also been shown that in time, due to wear or material characteristics, joints may change their dynamic behaviour making it challenging to accurately create a dynamic model of a joint for design purposes.

Also at ASML, which produces high-precision lithography machines, the influence of incorrectly modelled joint dynamics can give rise to unwanted dynamic behaviour. A straightforward solution to many vibration and dynamic problems between jointed structures is to increase the stiffness between the assemblies of the machine [4], but due to space or design requirements of high precision machines, this may not always be possible. In particular due to these design requirements, vibrations within these structures are usually badly damped [4]. While large amounts of research is focusing on active vibration control, for example by using active structural elements for vibration control with co-located sensing [5, 6], correctly predicting how the jointing of individual assemblies influence the dynamics of the structure could greatly increase the understanding of the dynamic behaviour within an assembly. Being able to correctly model the joint parameters will increase the predictability of the system during the design phase, which inherently decreases the complexity of the validation phase when designing a new machine. Furthermore, by correctly identifying the dynamic behaviour of a system, fewer control schemes have to be applied, which in turn leads to a more robust end product.

Commonly used practice to model a joint is to describe the interface as a low-order effective stiffness and/or damping. However, the values of these springs and dampers can only be determined by using indirect experimental measurements [7], which for large structures can often be expensive and time-consuming. Here the need arises to develop modelling techniques of joints not based on indirect experimental data, but on physics. To this end, multiple academic institutes have created testing devices, which aim to capture the contact behaviour of joints subjected to varying loading conditions and interface parameters, such as roughness and material. Section 2.2 will dive deeper into the creation of these test rigs and how they extract joint characteristics.

2.2 Test devices in literature

Many interface models require (in)direct experimental data to accurately model stiffness and damping within joints. These experiments are carried out, under the presumption that the underlying physics of many interfaces can be represented to a reasonable degree by a cyclic load-deflection curve, also known as hysteresis [2]. The effectiveness of these types of experiments depends on the ability to reliably provide quantitative data on the characteristics of the interface details, such as normal loads, surface roughness and friction behaviour [8]. Multiple groups have been developing test equipment to generate their own quantitative data, which is consecutively used to simulate joint behaviour. The following sections will provide some examples of test rigs and the experimental data which is gathered from these setups, to create an understanding of how contact properties can be determined experimentally.

2.2.1 Friction rig at Imperial College London

At the Imperial College London a friction test rig has been designed in order to extract the friction coefficient (μ), and the tangential contact stiffness (k_t) for nonlinear analysis of a contact [8]. Figure 2.2.1 shows the friction rig fully assembled.

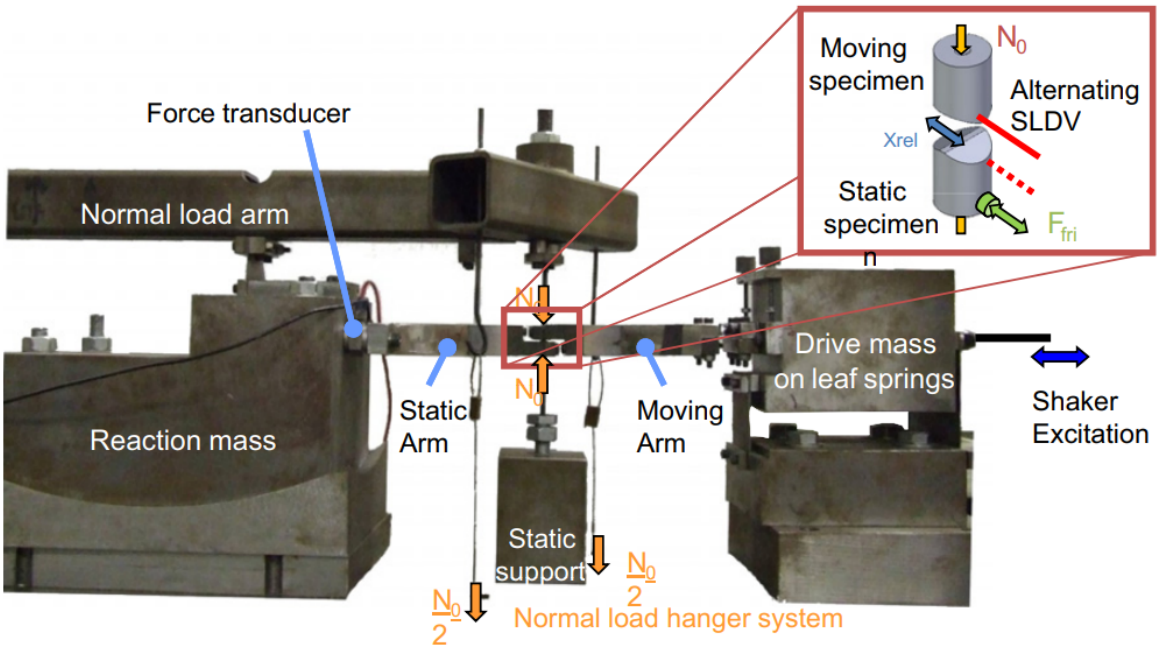

Figure 2.2.1: First generation testing rig at the Imperial College in London [8]

The function of the rig is to provide a one-dimensional relative sliding motion (x_{rel}) between two material samples, with a known normal load (N_0) applied across the contact. When simultaneously measuring the relative displacement and the transmitted friction force (F_{fri}), a hysteresis loop can be plotted from which the friction interface parameters can be extracted. An example of such a hysteresis loop and its characteristics is given in section 2.4. To provide the motion in the test rig, the drive mass is excited with a shaker at a frequency of 100 Hz, resulting in a relative motion with an amplitude ranging between 20 and 40 µm. Contacts of 1 mm^2 are used nominally, but other widths and contact areas have also been investigated. A normal force can be applied to the two specimens ranging from 5 to 75 N, and by changing the contact area pressures of up to 350 MPa have been tested. Additionally, a furnace can be used to allow for measurements up to 1050 °C. The relative displacement between the sliding contacts is measured using a Scanning Laser Doppler Vibrometer (SLDV), at points very close to the contact areas. The transmitted friction force is measured using two force transducers between the static arm and the reaction block.

2.2.2 Friction rig at Politecnico di Torino

Similar to the test rig at the Imperial College London, the test rig at the Politecnico di Torino was developed to perform hysteresis loop measurements from which the contact stiffness, dissipated energy and friction coefficient can be extracted [2]. It was further improved in order to perform fretting tests with relative displacement control. Also similar, the test rig is able to work at high temperatures of up to 1000 °C. A schematic overview of the test rig is given in Figure 2.2.2.

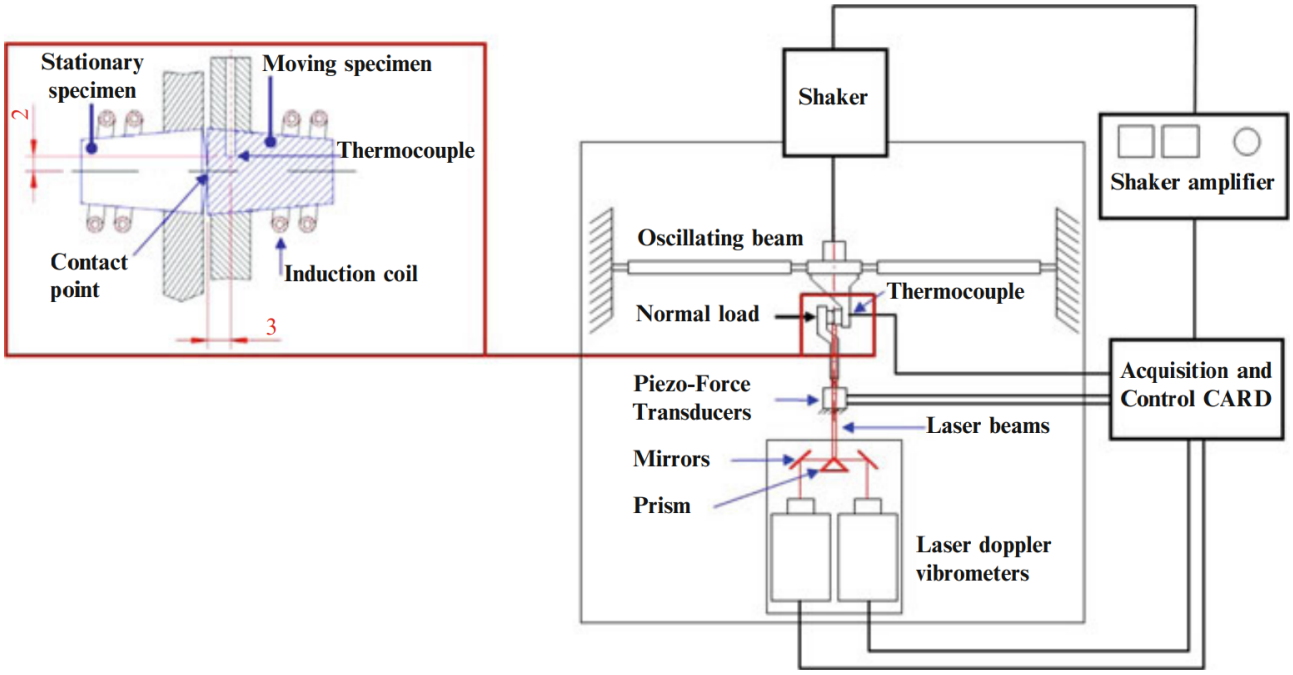

Figure 2.2.2: 1st generation test rig at Politecnico Di Torino [2]

In this test rig, two specimens form a point contact which is rubbed against each other with a displacement, typically ranging from 1 to 250 µm, with a constant normal loading applied. The system is excited using a shaker attached to a leaf spring, and two LDVs are measuring the displacement of each individual surface. The displacement can be prescribed in this setup, due to the position feedback control applied to the shaker [9]. To provide the temperature range, two induction coils are wrapped around the test specimens. From these measurements, the same interface parameters can be extracted as the Imperial College London test rig.

2.3 Novel fretting test apparatus

The main inspiration for this study into contact properties comes from a novel fretting test apparatus designed by Li et al. [10]. In this research, a relatively small and simple test device has been constructed, which uses the principle of flexure mechanics and a piezoelectric actuator to produce the needed displacement between a bolted connection to form a hysteresis curve. Compared to the devices described in the previous section, this device has a relative small footprint with an enclosed frame that is easily machinable. Additionally, in this device a novel technique that only uses a single LDV laser is used to directly measure the relative displacement between the two contacting surfaces. In hysteresis research, it is common to use two LDV's to measure the movement of the individual surfaces, after which the relative displacement is found by post-processing and subtracting the movement of one surface from the other surface. Using this new technique however, a single measurement

is sufficient to capture the movement of the joint, eliminating the uncertainty of post-processing the data. Together with a direct measurement of the tangential force present in the contact, the hysteresis curve is directly presented. A schematic overview of the device and the resulting hysteresis curves is given in Figure 2.3.1.

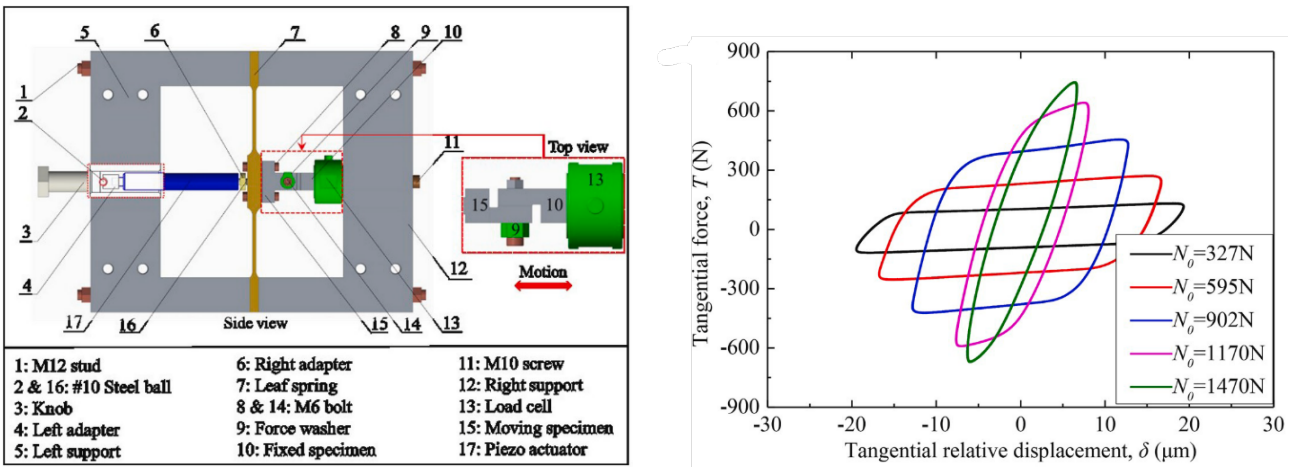

(a) Schematic overview of the fretting device

(b) Measured hysteresis curves

Figure 2.3.1: Designed fretting apparatus and measurement results [10]

The goal of this research is to extract all relevant knowledge in designing a fretting device from literature, and adapt it to such a degree that the contact properties of larger, custom-designed contacts can be determined experimentally. Due to the new approach of the research performed by Li et al., where a relatively small and machinable fretting apparatus is designed, this design ideology for constructing an experimental fretting device forms the basis of this study. However, compared to the devices constructed by the Imperial College London, Politecnico di Torino and Li et al. which focus on small contact areas, this research will distinct itself in moving away from a bolted connection and construct an experimental setup that will focus on large, custom-designed flat on flat contact joints. The constructed device will also be used to determine the effects of contact pressure, excitation frequency and surface roughness on the contact stiffness, energy dissipation and friction coefficient.

2.4 Background theory

This section describes the relevant background theory used throughout the thesis and serves as a theoretical foundation on which the experimental results will be based.

2.4.1 Frequency response analysis

The frequency response of a system shows how a system behaves across a range of frequencies. Typically the vibrations are measured against a sinusoidal input force, which are then characterised in terms of both magnitude and phase. The magnitude describes how the amplitude, or strength, of the output signal varies with frequency, and shows at what frequencies the system amplifies or dampens the input signal. The phase response describes the phase shift introduced by the system at different frequencies. Phase shift refers to the delay or advance in the timing of the output signal relative to the input signal.

A mathematical derivation of the magnitude and phase that construct a Frequency Response Function (FRF) is given in Appendix A, while a graphical representation of the frequency response is given in Figure 2.4.1.

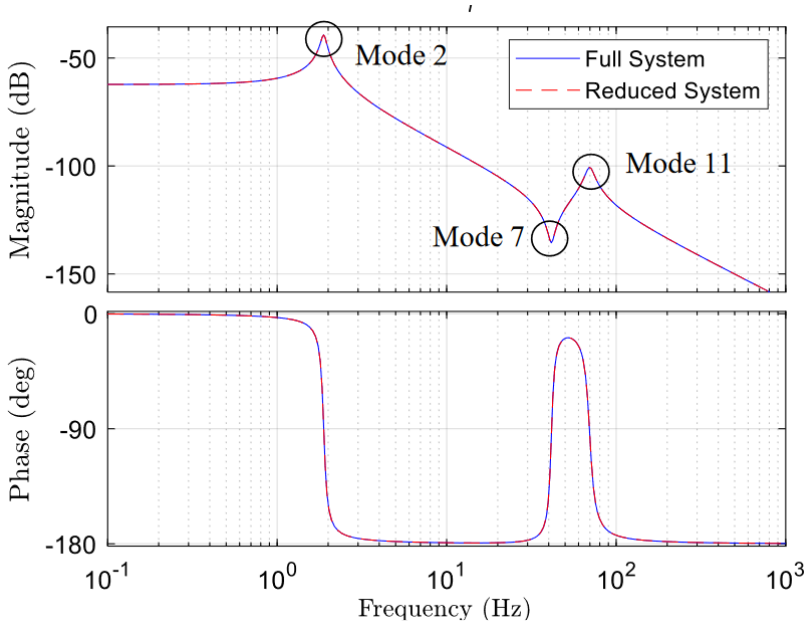

Figure 2.4.1: Example of a Frequency Response of a system [11]

A frequency response can be determined experimentally by applying a known input signal by either a shaker or a modal hammer and measuring the resulting output acceleration using accelerometers.

An additional distinction can be made between accelerance, mobility and compliance, where acceleration, velocity and displacement are plotted against input force respectively. For this research the accelerance $A(f)$ and the mobility $M(f)$ are of interest, which are mathematically described in the frequency domain as

$$A(f) = \frac{\ddot{Y}(f)}{F(f)} \quad \text{and} \quad M(f) = \frac{\dot{Y}(f)}{F(f)} \tag{2.1}$$

in which

- $F(f)$ is the input force onto the system
- $\ddot{Y}(f)$ is the measured acceleration of the system
- $\dot{Y}(f)$ is the measured velocity of the system

2.4.2 Modal analysis

The goal of a modal analysis of a system is to find the eigenfrequencies and mode shapes of a structure. The eigenfrequencies, also denoted as resonance or natural frequencies, is a system characteristic frequency at which the system naturally oscillates or vibrates. These frequencies are determined by the physical properties of the system such as mass, stiffness and applied boundary conditions. The eigenfrequencies can be calculated by solving the eigenvalue problem, derived from the equation of motion with an applied modal coordinate transformation,

$$\{x\}_i = [\Phi]_{ij} \{\eta\}_j \tag{2.2}$$

In which

- $\{x\}$ represents the generalised coordinates of the system
- Φ represents the modal matrix
- η represent the modal coordinate vector.

First the eigenfrequencies, derived from the equation of motion of the system is determined for an undamped system, solving the equation

$$\det\left([K] - \omega_n^2 [M]\right) = 0 \tag{2.3}$$

in which

- [K] represents the stiffness matrix of the system
- [M] represents the mass matrix of the system
- ω_n is the natural frequency

To find the mode shapes (or eigenvectors) of the system, the eigenfrequencies are back substituted into Equation 2.3 and solved for $[\Phi]$.

In structural dynamic problems, the response of a system can typically be described by the summation of a small number of uncoupled modes or mode shapes. By formulating the dynamic behaviour of the system as a combination of modal contributions and scaling factors, a much more efficient method for calculating the response of a system is achieved. This approach is typically used when a harmonic response over a certain frequency region is of interest. Using this modal superposition method, the complete system response is expressed as a summation of all mode shapes as

$$\{x\}(t) = \sum_{i=1}^{n} [\Phi]_{ij} \{\eta\}_i. \tag{2.4}$$

2.4.3 MAC analysis

To have a quantitative measure of the correlation between modes of a between a numerical model and an experimental data set, a Modal Assurance Criteria (MAC) analysis can be performed [12]. The formula for a MAC between the rth mode of test modal vector $\{\phi\}$ and the qth mode of a numerical modal vector $\{\psi\}$ is given by

$$\text{MAC (r, q)} = \frac{|\{\phi\}_r^T \{\psi\}_q|^2}{(\{\phi\}_r^T \{\phi\}_r)\left(\{\psi\}_q^T \{\psi\}_q\right)} \tag{2.5}$$

The MAC value ranges from 0 to 1, where 1 indicates a perfect correlation between mode shapes and 0 indicates no correlation. If the MAC values are high, it suggests good correlation and confidence in the numerical model. If the values are low, it may indicate discrepancies between the numerical and experimental model that need to be addressed, such as model updating or adjustments to the experimental setup.

It is also possible to correlate the mode shapes of only a numerical model to each other, where the mode shape vector of the experimental data is replaced by the same numerical modal vector. This is usually referred to as an autoMAC, and will give a representation of similarity between individual modes within a numerical model. Ideally, only the same modes should have a MAC value of 1, while all other correlations have a value of 0. This means that all modes are orthogonal to each other, and no linear combination of modes can result in a different mode shape.

2.4.4 Hysteresis curve

To create a hysteresis curve, two surfaces are connected together after which a cyclical loading is applied to one of the surfaces to induce sliding within the contact. This loading profile is illustrated in Figure 2.4.2a, and a typical hysteresis curve as measured with the testing rigs is depicted in Figure 2.4.2b. In Figure 2.4.2 the force reversal points are indicated for both the tangential force and

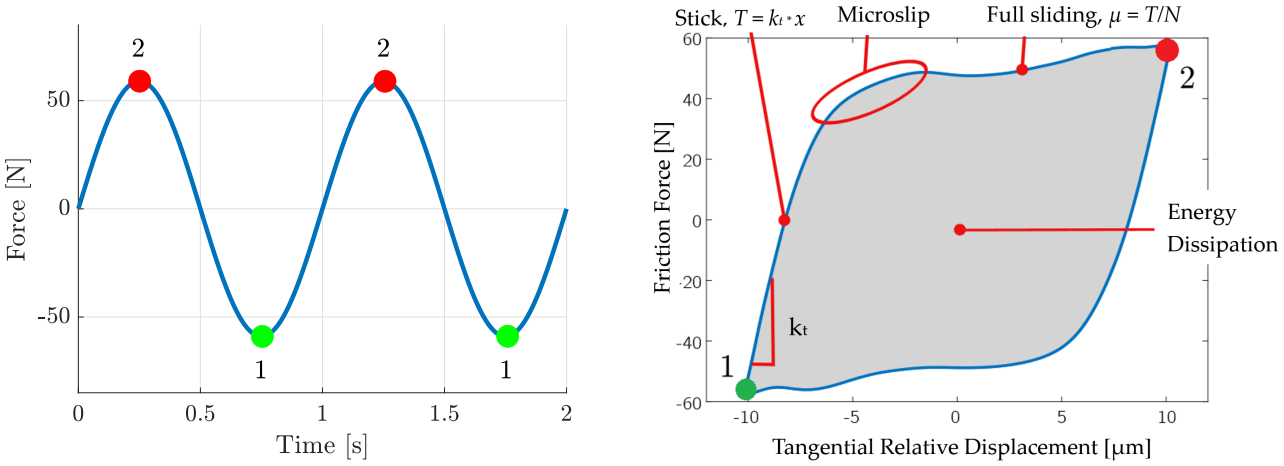

(a) Loading profile

(b) Standard hysteresis curve from experiments [13]

Figure 2.4.2: Resulting hysteresis from excitation force

the resulting displacement. The moment the force changes direction, the relative displacement of the contact also changes direction, and experiences three distinct stages of stick-slip motion. These are also indicated in Figure 2.4.2b. At the stick regime (i), which occurs immediately after the reversal of the direction of motion, linear displacement-force dependency due to the elasticity of the rough interface is dominant. Region (ii) denotes the micro-slip stage, where some parts of the contact start to lose cohesion and transition from stick to slip. At (iii), the entire contact has lost contact and transitioned from stick to slip, such that macro-slip occurs. During this stage, it can be observed that the transmitted friction force remains relatively constant. The tangential contact stiffness can be extracted by curve fitting a straight line onto the lower section of the stick regime, since the displacement here is purely due to the elastic behaviour of the two material surfaces in contact. The second contact property that can be extracted from the hysteresis curve is the friction coefficient. This is determined by dividing the tangential force measured during the macro slip regime by the applied normal load, according to the standard formula for friction force

$$F_{fri} = \mu_f N_0. \tag{2.6}$$

The final property that can be extracted from the hysteresis curve is the amount of energy dissipated within one cyclic motion of the contact, which corresponds to the surface area of the hysteresis curve. This energy is dissipated in the form of plastic deformation of the asperities of both surfaces in contact, or as heat.

2.4.5 Damping ratio

When two surfaces start sliding while in contact, the kinetic energy is used to elastically and plastically deform the asperities in contact, and is dissipated as heat due to the friction work. Therefore, the dissipated energy extracted from a hysteresis curve is a measure for the damping present within the contact.

However, to model the damping present in the joint, it is preferred to determine the damping ratio of this connection. To relate the damping ratio to the dissipated energy, the joint is represented as a simple spring-mass damper system, where the position of the mobile stage (x), can be expressed as a harmonic function of time as

$$x = Ae^{-\zeta\omega_n t}\cos(\omega_d t - \phi) \tag{2.7}$$

in which ω_n denotes the natural frequency of the undamped system, ω_d represents the natural frequency of the damped system and ζ is the damping ratio. The parameter A stands for the maximum amplitude of the displacement and ϕ represents a phase difference, which both can be determined through the initial position and velocity of the mass. The other parameters are related to the system's physical parameters, such as stiffness (k), damping coefficient (c) and mass (m), according to

$$\omega_n = \sqrt{\frac{k}{m}} \tag{2.8}$$

$$\zeta = \frac{c}{2m\omega_n} \tag{2.9}$$

$$\omega_d = \omega_n\sqrt{1-\zeta^2} \tag{2.10}$$

Without loss of generality, $t = 0$ can be set to a point that $\phi = 0$, such that Equation 2.7 can be simplified to

$$x = Ae^{-\zeta\omega_n t}\cos(\omega_d t) \tag{2.11}$$

and with its derivative as

$$\dot{x} = -A\omega_n e^{-\zeta\omega_n t}\left(\zeta\cos(\omega_d t) + \sqrt{1-\zeta^2}\sin(\omega_d t)\right). \tag{2.12}$$

To relate the displacement and velocity of the energy within the system, the total energy can be described as the summation of potential energy (U) and kinetic energy (V), which are described as

$$U = \frac{1}{2}kx^2 = \frac{1}{2}kA^2\left[e^{-\zeta\omega_n t}\cos(\omega_d t)\right]^2 \tag{2.13}$$

and

$$V = \frac{1}{2}m\dot{x}^2 = \frac{1}{2}m\omega_n^2 A^2\left[e^{-\zeta\omega_n t}\left(\zeta\cos(\omega_d t) + \sqrt{1-\zeta^2}\sin(\omega_d t)\right)\right]^2 \tag{2.14}$$

where according to Equation 2.8 the spring stiffness can be substituted to get

$$V = \frac{1}{2}kA^2\left[e^{-\zeta\omega_n t}\left(\zeta\cos(\omega_d t) + \sqrt{1-\zeta^2}\sin(\omega_d t)\right)\right]^2. \tag{2.15}$$

The summation of these contributions describes the measured dissipated energy within the contact, as measured with the experimental setup. The natural frequency of the system, i.e. when no loading is applied to the contact, can be determined when no contact pressure is present. The damped resonance frequency can be determined for each level of contact pressure desirable. With all these parameters, the numerical change in energy determined as $\Delta E = \Delta U + \Delta V$ and the measured dissipated energy are used to determine the damping ratio.

Chapter 3

Setup design and validation

This chapter describes the steps taken on designing a testing device, which is able to accurately measure the contact interface parameters between two surfaces in contact. It explains what requirements are set in place to perform the desired experiments, and how these design requirements translate to design choices. Once all requirements are met, it will elaborate further on how the numerical model is constructed and what the simulated dynamic response of the system is. Subsequently, an experimental identification is conducted on the assembled device, after which the correlation between numerical and experimental model will be investigated in further detail.

3.1 Design of testing rig

In order to develop an experimental device which is able to accurately measure the contact parameters such as contact stiffness, friction coefficient and damping between two surfaces, several requirements have been set. These are based on the requirements found in literature and combined with application-specific requirements, and are described below after which each requirement will be explained in further detail.

- Producing a dominant Single Degree of Freedom motion
- Application of normal and excitation forces
- Experimental data acquisition
- Properties of contacting surfaces
- Operating ranges

Producing a dominant Single Degree of Freedom motion

As the main requirement the experimental device should behave as a dominant single-degree-of-freedom (SDOF) excitation rig, in which only a cyclical, small-amplitude sliding motion between two connecting surfaces is realised [14]. If multiple directions of sliding are present during testing, the measurement of contact stiffness in the tangential direction will no longer capture the full behaviour of the interface. Instead of accurately capturing the normal and tangential stiffness components, vectors with both components in normal and tangential directions will occur on the interface, which are difficult to separate from each other. The design has to ensure that the first mode of the system is purely translational, and that its eigenfrequency is at the end of the desired frequency measuring range to reduce the effect of resonance of the system as much as possible in the measurements.

Furthermore, to ensure that only the first mode is dominant, the design has to ensure that the eigen-frequency of the higher-order modes are placed well above the desired frequency measuring. This is to ensure that these modes do not introduce any unwanted dynamics, such as bending and torsional effects into the desired measuring range.

Application of normal and excitation forces

The test rig should be able to infer two distinct forces onto the contact, a normal force and a tangential force. The normal force is needed to apply contact pressure between the two surfaces and should be able to be set at various force levels. This is to ensure that multiple loading conditions can be tested, ranging from barely any contact pressure up to full contact, i.e. high contact pressure. Secondly, the device needs to apply a tangential loading onto the contact surface, such that an (almost) sliding motion can be realised.

Experimental data acquisition

To capture usable and reliable data from the performed experiments, multiple continuous measurements should be taken during the experiment. To determine the friction coefficient, tangential stiffness and damping characteristics of the interface, a measure of relative displacement between the two connected surfaces should be present. Furthermore, transmitted force through the contact should be measured directly. The following physical properties will need to be measured:

- Acceleration of the mobile contact block
- Acceleration of the rigid contact block
- Excitation force delivered onto the system
- Force in sliding direction transmitted through the contact onto the rigid block

Properties of contacting surfaces

To capture usable and reliable data from the performed experiments, multiple continuous measurements should be taken during the experiment. To determine the friction coefficient, tangential stiffness and damping characteristics of the interface, a measure of relative displacement between the two connected surfaces should be present. Furthermore, the tangential force which is being transmitted through the contact interface should be measured directly.

Operating ranges

From literature it has become clear that contact hysteresis experiments are generally conducted under a specific range of loading conditions. These, together with the application range of the lithography machines, the following requirements have been set over which the input parameters should be able to perform.

- Normal force: 0 - 250 N
- Displacement amplitude: 0 - 100 µm
- Tangential force: 0 - 100 N
- Frequency range: 0 - 150 Hz

The following sections will elaborate further on the individual requirements, and what design choices were made to ensure that the final conceptual testing device met these set requirements.

3.1.1 Producing a dominant Single Degree of Freedom motion

To realise the SDOF motion, the translational sliding of the two surfaces, it was chosen to use a double leaf spring assembly. A double leaf spring assembly is chosen to constrain any rotation around all axis, while also constraining translation in the unwanted directions. This assembly is based on the Freedom and Constraint Topology (FACT) method to design flexure mechanisms, developed by Hopkins et al. [15, 16]. This double leaf spring approach differs from the experimental setups used in literature, where typically a single leaf spring is used to constrain the unwanted motion of the mobile stage [10]. Furthermore, preliminary testing with a single leaf spring assembly showed the appearance of unwanted rotation around all axes, thus the application of the double leaf spring assembly is necessary to achieve the desired motion. The test device uses a 100 N electro mechanical shaker to excite the system. This shaker is connected to to the leaf spring assembly via a threaded rod, guaranteeing a stiff and secure connection. Since the shaker has a maximum force output of 100 N, the leaf spring assembly needs to be designed in such a way that at 100 N a displacement of 100 µm is reached.

To determine the total deflection of the leaf spring, and thus the maximum relative displacement of the contact interface, a calculation based on the beam equations is performed. To calculate the total maximum deflection in the center of a double-sided clamped beam, the equation

$$\delta_{max} = \frac{FL^3}{192EI} \tag{3.1}$$

is used. In which

- F is the applied excitation force
- L is the length of the leaf spring
- E is the modulus of elasticity of the material
- I is the moment of inertia of the beam

By designing an assembly with two connected leaf springs, each with a thickness of 2 mm, an effective thickness of 4 mm is used for this calculation. When applying a load of 100 N in the center of the assembly, it shows that a leaf spring with a height of 50 mm and a length of 200 mm produces a center deflection of 78.1 µm. In literature, depending on the loading conditions are present, a relative displacement between 20 µm [10] and 300 µm [17] is preferred. While this deflection is in the desired displacement range, a thinner leaf spring would lead to a larger deflection under a load of 100 N, thus allowing for testing of larger displacements if needed during experiments. To verify the calculation, a static analysis is performed. Here also the contacting block is added, to simulate the added weight on the leaf spring present during testing. Using Ansys Workbench, a leaf spring assembly consisting of two 200 mm by 50 mm leaf springs with a thickness of 2 mm has been modelled out of structural steel, its properties are listed in Table 3.1. This table also provides the material properties of the contacting surfaces, which are made out of 7060-grade aluminium.

The analysis shows a total mass of the system of 10,824 kg, which corresponds with the weight of the later constructed system. The element types used in this simulation consist of both SOLID186 and SOLID187, both higher-order 3D elements to ensure that all deformations, especially damping, are accounted for. To create the contact surfaces on these elements, both CONT174 and TARGE170 elements are used. More detailed information on the used elements, and how the connections are realised within the assembly, is given in Appendix D. An overall mesh size of 0.5 mm is chosen in this analysis, to ensure that at least two elements are present over the thickness of the leaf springs.

Table 3.1: Material properties used in simulation [18]

Property	Structural steel	AL 7060
Poisson's ratio [-]	0.3	0.33
Young's Modulus [GPa]	207	71
Density [kg m^{-3}]	7830	2770
Yield Strength [MPa]	250	280

To ensure that the solution has converged, two refinement steps based on the residual strain energy have been added to the mesh size of both leaf springs and the contacting surfaces, resulting in a total element count of 331133. The simulation shows that the double leaf spring assembly has a total deflection of 220 µm. This is in the same order of magnitude as the hand calculation, however differs by a factor of three. This can be attributed to the addition of the spacer block between the leaf springs, which adds extra mass to the system which is not taken into account for the hand calculation. Since both results are however in the desired displacement range, leaf springs with a length of 200 mm, a thickness of 2 mm and a height of 50 mm are chosen to be used in the test device. If a larger deflection is needed during experiments, the leaf springs should be interchanged with a 0.5 or 1 mm thick leaf spring. Furthermore, during the experiments based on these displacements, different excitation forces will be used, such that the contact will go through the stick, micro and macro slip regimes.

To determine if an SDOF motion is realised, a modal and consequential harmonic analysis has been performed. The modal analysis determines the eigenmodes present in the device, and at what eigenfrequency these modes occur. It is necessary that the first eigenmode is the same motion as forced by the shaker, such that experiments can be performed up to and including that first resonance frequency. The other eigenmodes, which are unfavourable due to their bending and torsional behaviour, should have their eigenfrequency relatively far from this first resonance, such that they do not contaminate the desired motion of the moving stage. The solution from the static analysis has been used as a pre-stressed input state of the simulation, which provides the modal response of the assembly under load.

The first eigenmode is depicted in Figure 3.1.1a, where it can be seen that the first eigenmode behaves as the desired motion of the experimental device.

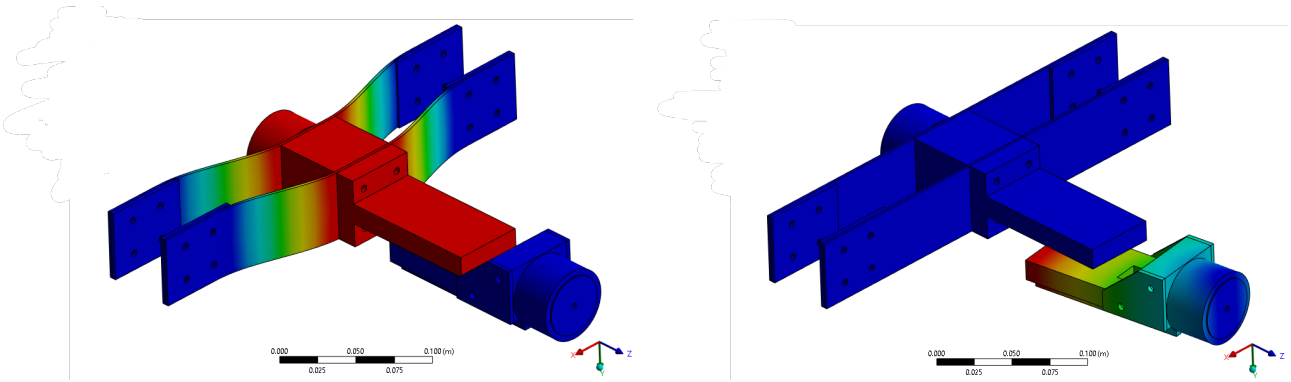

(a) Mode 1: 69.5 Hz

(b) Mode 2: 246.9 Hz

Figure 3.1.1: First two eigenmodes of experimental setup

This mode occurs at 69.5 Hz, which is lower than the desired 150 Hz stated in the requirements of the testing device. However, this first eigenfrequency is highly dependent on normal loading conditions within the contact. In this simulation, a contact force of 5 N has been placed on the contact, while a simulation without any contact force resulted in a first eigenfrequency of 128 Hz. Therefore, during testing each contact force level should be investigated to determine at which frequency the resonance occurs. Figure 3.1.1b shows the second eigenmode, which has an eigenfrequency of 246.9 Hz. Since the contacting bodies are sliding across each other perpendicular to the desired sliding motion, this mode is unwanted and should therefore be placed out of the desired frequency range as far as possible.

Table 3.2 characterises the remaining 4 eigenmodes, their motion and their corresponding eigenfrequency. While there is a 128.6 Hz difference between the first and second eigenmode, the second mode will most likely still influence the behaviour of the system in the range of 0 - 150 Hz. To determine this influence, and if the desired motion in z-direction is dominant over the movement in the other directions, a harmonic simulation is conducted.

Table 3.2: First six eigenmodes and their eigenfrequency

Mode	**Frequency** [Hz]	**Type**	**Axis**
1	69.5	Translational	z
2	246.9	Bending	y
3	344.5	Bending	y
4	356.6	Bending	x
5	365.6	Bending	y
6	461.5	Bending	x

The performed harmonic simulation uses the same numerical model as in the model analysis and calculates a continuous response of the system based on modal superposition. The accelerance, i.e. force against acceleration, for each individual direction is determined for a single point at the end of the mobile stage. This location is selected since it will resemble the section of the mobile stage which is in contact with the rigid stage. If there is a large acceleration in any unwanted direction, this will be transmitted onto the contact and render the experiment unusable. The indicated point and corresponding accelerance for all directions is given in Figure 3.1.2.

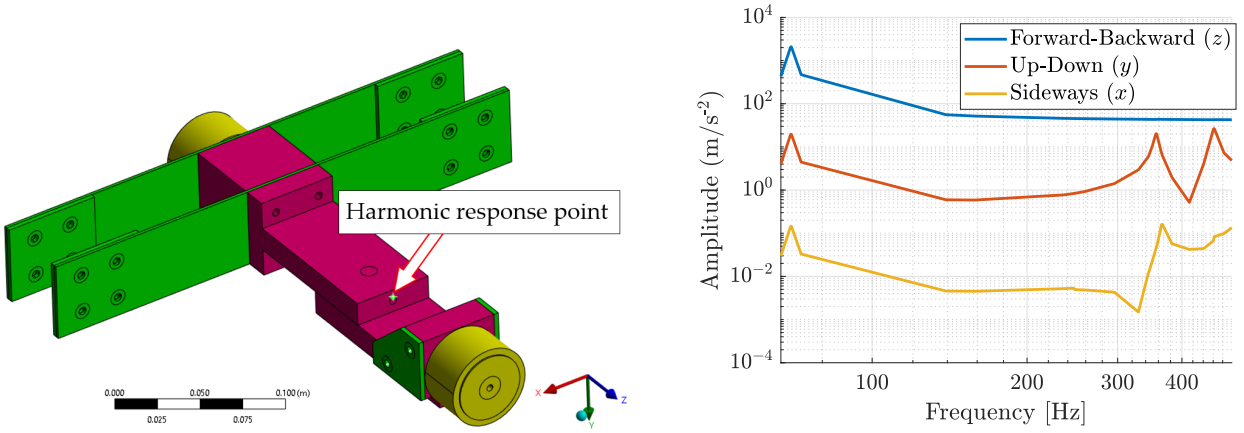

(a) Harmonic response location

(b) Simulated harmonic response

Figure 3.1.2: Harmonic response

Figure 3.1.2b shows that the mobile stage has a mostly translational motion up to around 215 Hz, where the acceleration in z-direction is orders of magnitude larger than the acceleration in either x or y-direction. This is a positive result since it shows that the leaf spring is constraining most of the bending and translational degrees of freedom, and only the desired motion is realised.

Next to the numerical model the double leaf spring assembly is also experimentally validated. After construction of the test setup, the movement of the mobile stage has been measured to an excitation force applied by the shaker, from which the response is presented in presented in Figure 3.1.3.

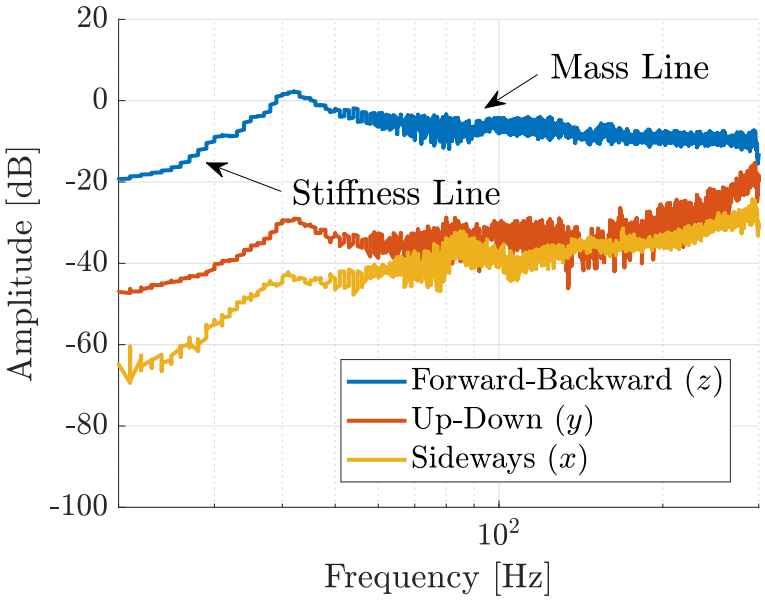

Figure 3.1.3: Experimental accelerance of double leaf spring configuration

Here it is also clearly visible that with a double leaf spring configuration, the desired motion is dominant over the sideways and up and down movement of the mobile stage, which both have a significantly smaller amplitude.

As stated earlier, from subsequent testing it was determined that the resonance peak of the double leaf spring configuration changes with contact pressure between the two surfaces. Since this resonance can have a significant effect on the contact properties due to an increase in displacement, the exact resonance peak should be identified for each loading configuration, and conclusions based on the experimental data should clearly distinguish between results before, during and after this resonance.

3.1.2 Application of normal and excitation forces

As already described in the previous section, the tangential excitation force is provided by a shaker which is attached to the double-leaf spring assembly with a threaded rod. To be able to apply a varying contact pressure onto the contact, an assembly that produces a variable normal force onto the contact should be constructed. However, the application of the normal force should not be a rigid contact, since this would introduce an additional source of stiffness in the measurements, which will contaminate the experimental data. Furthermore, the normal force should be in contact with the mobile and rigid stage at all times, to ensure even loading conditions onto the contact at all times.

The solution to this problem is to use spring plungers. These apply the normal force to the surface by means of a ball bearing loaded with a spring. The ball bearing ensures that a point contact is used to transfer the force while being able to slide across the surface to not introduce any stiffness. The spring plunger ensures that during testing the ball bearing will always be in contact with the mobile and rigid stage. An illustration of such a spring plunger is given in Figure 3.1.4a.

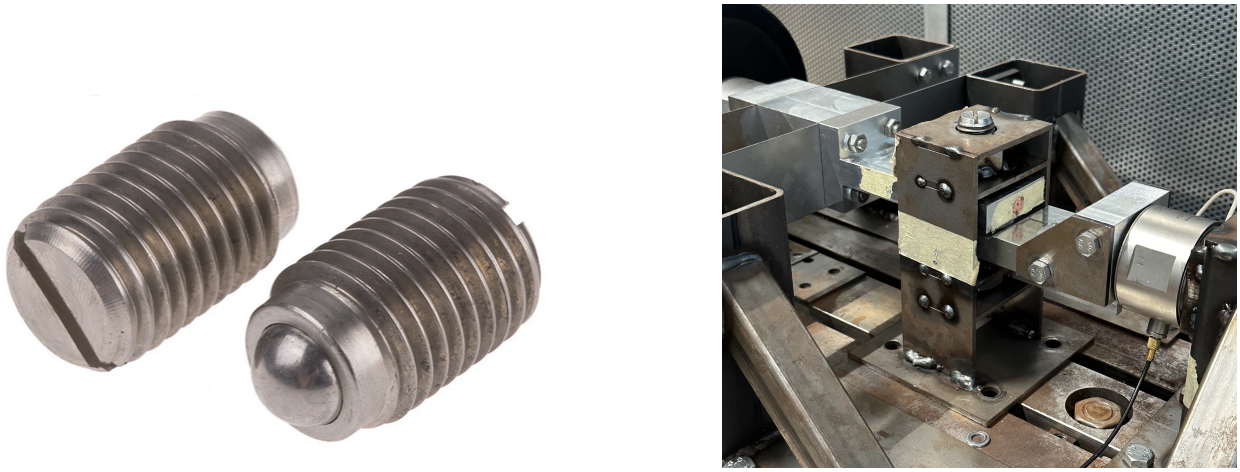

(a) Spring plunger to apply normal force

(b) Normal force assembly

Figure 3.1.4: Construction to apply a contact pressure

The spring plungers used are screwed into an assembly, placed around the two stages. Due to the linear spring, each rotation of the spring plunger results in an 18 N increase of normal force, with a maximum of 72 N until the housing of the spring plunger touches the contact block. Two spring plungers are used on either side of the contact to ensure symmetric loading conditions. A depiction of the complete assembly is shown in Figure 3.1.4b.

3.1.3 Experimental data acquisition

To create a hysteresis loop, from which the contact parameters can be extracted, both the tangential force and the relative displacement need to be captured. Additionally, to determine the response of the shaker and draw conclusions on the relation between applied force and tangential force, also the shaker input force should be measured. To measure the contact forces, two Dytran 1061 V2 dynamic force transducers are used. The input force sensor is directly attached to the shaker and leaf spring assembly. The tangential force sensor is mounted to the rigid stage and the supporting structure. It is also ensured that this force sensor is directly in line with the contact surface, such that the tangential force is in line with the sensor, resulting in a direct measurement of the tangential force present in the contact.

To measure the relative displacement, two accelerometers are placed at the end of each stage, similar to the point used in the harmonic simulation. These accelerometers register the acceleration of each contact surface, which can be integrated twice and subtracted from each other to provide the relative displacement. During experiments typically the rigid stage is assumed to be fixed. However, due to the small order of displacement values, and the easy implementation of a second acceleration sensor, during this research it is chosen to subtract the motion of the rigid stage from the mobile stage to eliminate this assumption. During experiments, the sensors should be placed as closely to the contact surface as possible, to reduce the effect of bulk stiffness in the measurements.

3.1.4 Properties of contacting surfaces

To answer the research question if a contact surface can be designed with predictable contact properties, the influence of a change in contact area needs to be investigated. To this end, three separate rigid stages have been constructed. The largest contact area consists of a circle with a diameter of 40 mm and a contact area of 1256.6 mm^2. The two other contact blocks each consist of a ring with an outer diameter of 40 mm, and a contact area of 2/3 and 1/3 of the first surface, respectively. This reduction in surface area is made to have a linear diminishing trend in contact area, such that later results in contact properties can be related to this trend. A sketch of the three contact interfaces is given in Figure 3.1.5.

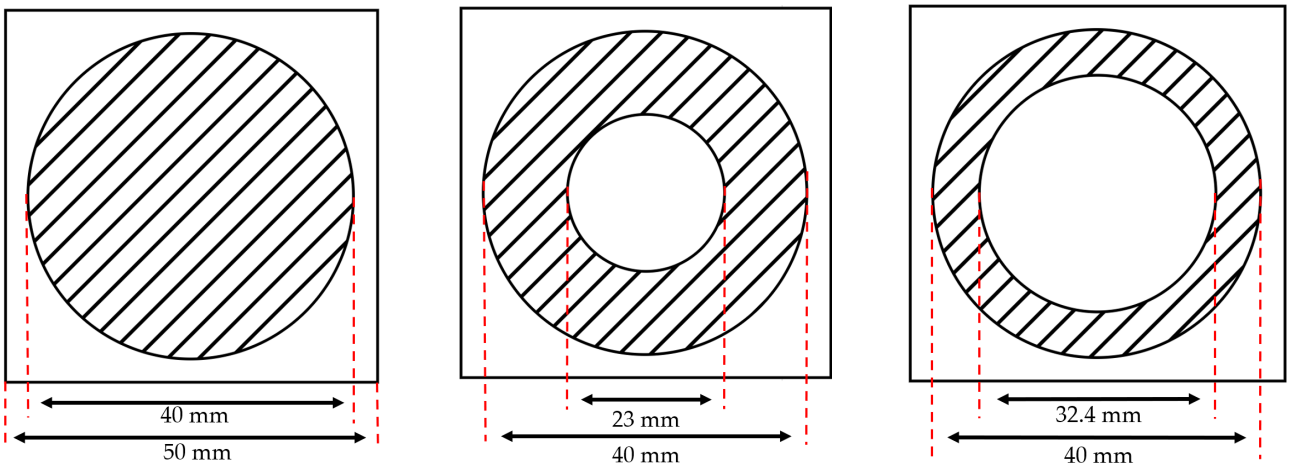

(a) Largest contact area (b) Medium contact area (c) Smallest contact area

Figure 3.1.5: Different contact surfaces

With the force plungers delivering a maximum normal force onto the contact of 72 N, the contact pressure for each of the contact areas can be calculated. For the full circle with a contact area of 1256.6 mm^2 a maximum contact pressure of 57.3 KPa can be achieved. For the contact areas with medium and small contact area, a maximum pressure of 85.9 KPa and 172 KPa can be reached respectively.

It was chosen to create three individual blocks with fixed contact areas instead of one block with interchangeable contact area. This is to ensure that no contact stiffness due to the connection between the contact surface and rigid stage is introduced into the measurements. The blocks are machined from 7060 grade aluminium, and are all produced simultaneously to decrease the chance of different surface roughnesses, which may affect the measured properties. The roughness value of these surfaces will later be determined when designing the experiments.

3.1.5 Operating ranges

To achieve the frequency operating range of 0 - 150 Hz, the influence of structural modes originating from the support of the leaf spring and force transducers should be minimised. These supports are therefore designed to be as stiff as possible with the available materials. Cold drawn 60 mm x 60 mm is used to provide the height and stiffness of the structure. During simulations however, this did not provide the required stiffness in the device. The design has subsequently been reinforced by adding additional diagonal support beams onto sections which showed the largest amounts of deformation under harmonic loading conditions, indicated by point 8 in Figure 3.1.6. Apart from the diagonal

supports, also a reinforcement plate needed to be added to the tangential transducer support, to prevent internal torsion modes from the tube influencing the measurements. This plate is indicated with point 9 in Figure 3.1.6. The vertical assemblies are welded together to a base plate, which is secured to a concrete slab with multiple bolted connections. This is to ensure that no rigid body modes will occur during measurements. The leaf springs and force transducers are fixed to the support structure with a bolted connection, which are tightened by hand to not damage the components.

To increase the repeatability of the system, the rigid block is designed to be easily interchangeable by loosening one bolt. A different specimen can subsequently be put in place fairly easily, by re-tightening the locking bolt. All other components used to create the full model are indicated in Figure 3.1.6. section 3.2 will elaborate on the testing device constructed based on this design, and further describe how the assembled system is validated for the operating ranges set in the requirements.

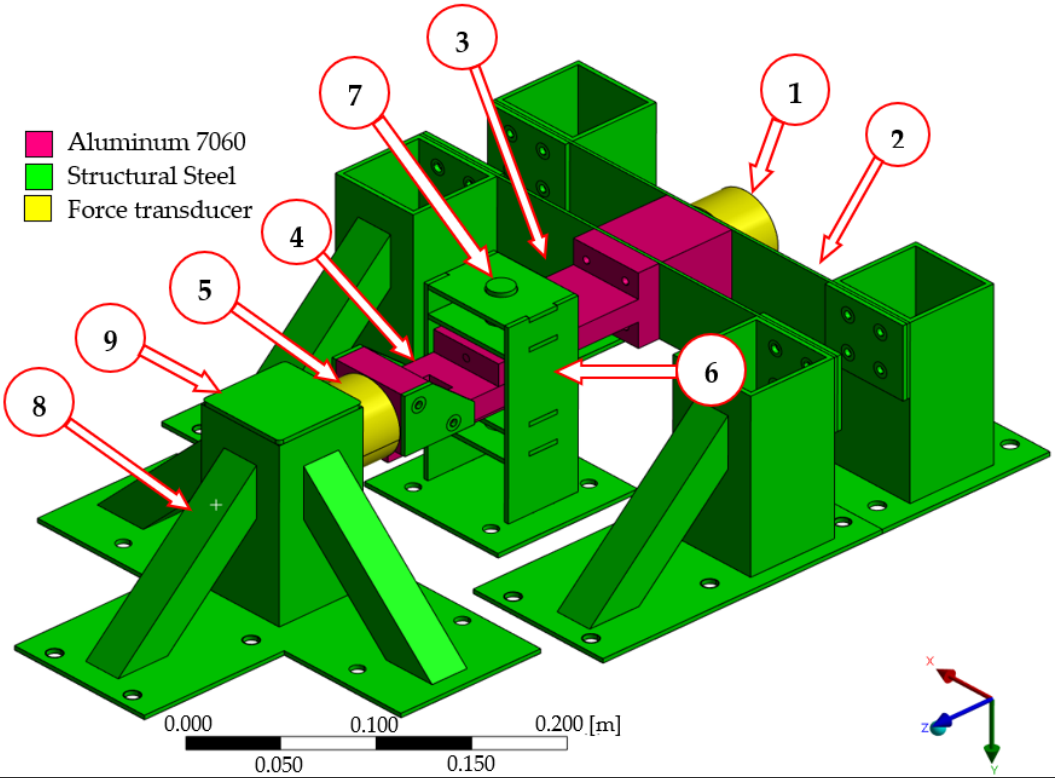

1: Shaker force sensor	4: Rigid stage	7: Force plunger
2: Leaf springs	5: Tangential force sensor	8: Diagonal reinforcements
3: Mobile stage	6: Normal force assembly	9: Reinforcement plate

Figure 3.1.6: Designed test setup

3.2 Validation of the design

3.2.1 Numerical model

To determine the correlation between the numerical FEM model and the experimental model, first a dynamic simulation of the entire test device needs to be conducted. As stated earlier, most of the connections between the steel structures are welded, for example between the leaf spring supports and base plates. These connections are modelled as bonded Multiple Point Constraints (MPC) contacts. The same contact definition is used for the bolted connections within the structure, where it will be acting on the effective radius of the thread, as defined in Roloff Matek [19]. The interface connection between the two contacting surfaces has been modelled as a frictionless contact. It is assumed that the contact experiences no friction, since during these simulations the movement of the mobile stage is of interest. The model could be expanded by introducing friction in the contact, however that would be too complex for an eigenfrequency analysis and for this research all friction parameters will be evaluated experimentally.

Since the entire setup, including the shaker, is fixed rigidly to a concrete block to simulate a static connection to the ground, the base plates are also fixed rigidly in space during simulations. The base plates are connected to the concrete slab using bolts, thus these connection are fixed in all translations and rotations. The mesh used on the system is not uniformly dispersed, since several areas are not of interest and to reduce the computation time of the model. The leaf spring is subjected to the largest deformation, thus a fine mesh size with an element sizing of 1 mm has been used, such that at least two elements are distributed over the width of the leaf spring. Mesh refinement based on residual strain energy shows that a further refinement of the mesh yields no significant change in results, but increases the computational time significantly, so no further refinement is made.

To relate the numerical model with an experimental model, first the response of the model to a harmonic excitation force needs to be determined. In Figure 3.2.1a the harmonic response points are indicated, from which the accelerance to a harmonic input at the shaker location is determined. Note that the location of sensor three is on the rigid stage in z-direction. The response of these six measurement points around the entire testing device is given in Figure 3.2.1b.

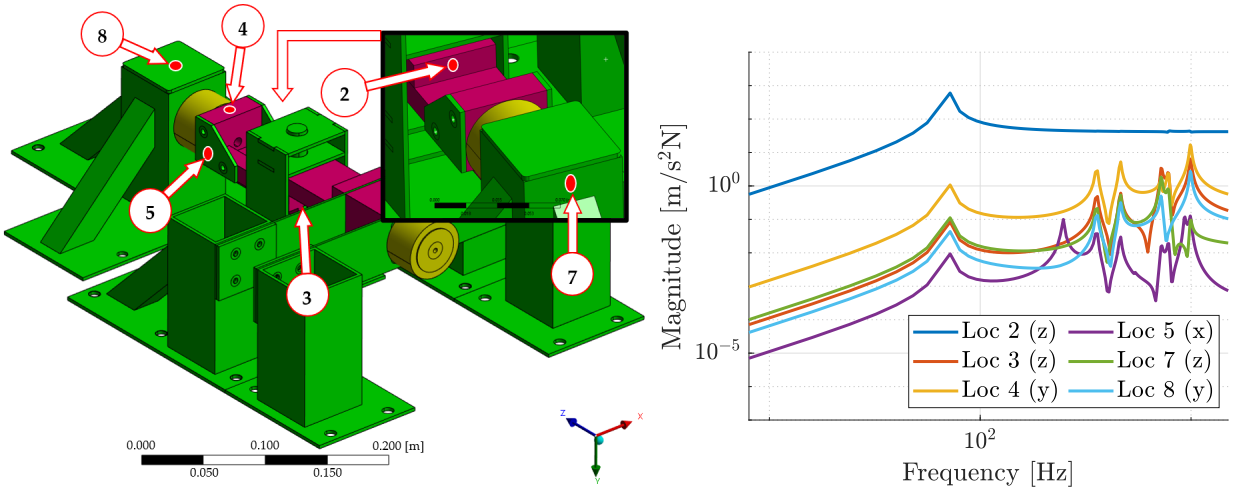

(a) Sensor locations on test device

(b) Numerical accelerance of six measurement points

Figure 3.2.1: Sensor locations on the setup and corresponding accelerance

All sensors are uni-axial sensors, meaning that they only measure the acceleration normal to the surface they are attached to. It can clearly be seen that all sensors are measuring a relatively low response from 0 to 150 Hz, after which they are excited by the first mode at 69.5 Hz which shows a high accelerance for all sensors. The peak in sensor two shows that the desired translation of the moving stage is clearly dominant over the other motion of the system. Moving to higher frequencies, the magnitude of the desired motion remains relatively constant while the magnitude of the other sensors increases. From this simulation it becomes clear that the response of sensor three, which is a measure for the translation of the rigid stage, shows a very low amplitude as desired. Sensor four is a measure for the y-axis bending behaviour (up and down motion), since this sensor is measuring the vertical displacement of the rigid stage. Sensor 5 measures the direction perpendicular to the desired lateral motion, sensing any bending motion of the rigid stage. Sensors 7 and 8 are placed on the back support, in order to determine what forces and displacements are transmitted through the force transducer onto the supporting structure. It can be concluded from this simulation that this testing device produces a dominant SDOF motion across the contact, with unwanted dynamics only appearing after 250 Hz, which is outside the desired operating range of the device.

3.2.2 Experimental model

The simulation is validated by means of experimental testing. An illustration of the assembled testing device is given in Figure 3.2.2.

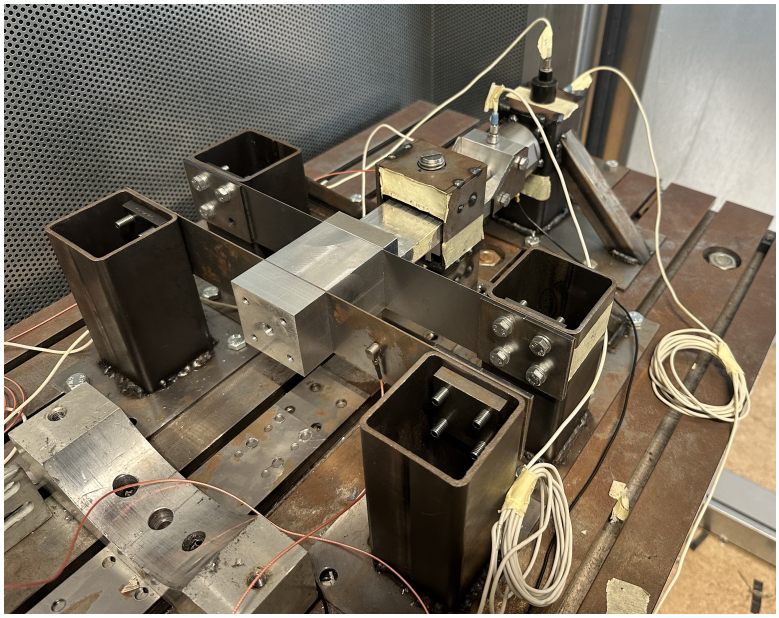

Figure 3.2.2: Assembled test device

By means of a roving hammer modal analysis, the response of the testing rig to an excitation was determined. During a modal hammer test, the sensors remain stuck on their individual sensor location, while the hammer is used to excite multiple positions around the device. The aim is to excite as many modes as possible, such that a clear picture of the eigenmodes and their corresponding eigenfrequencies of the assembled device is acquired. The sensor data is processed to extract the modal parameters, which provide the modal vector of each mode and the corresponding eigenfrequency. Using this data, a Modal Assurance Criteria (MAC) is performed on the numerical modal vectors and experimental modal vectors, which will determine how accurate the numerical model corresponds to the assembled device.

Figure 3.2.3 shows the response of six sensors to an excitation force in the middle of the leaf spring, where the shaker will be attached to provide the cyclical excitation force. A sharp peak is observed for the situation where no contact pressure is applied, which corresponds to the desired translational motion of the mobile stage. When a contact pressure is applied, this peak vanishes and the acceleration drops in amplitude. This is to be expected, since the contact pressure locks the contact in place, and the energy is distributed through the entire device, instead of solely on the mobile stage.

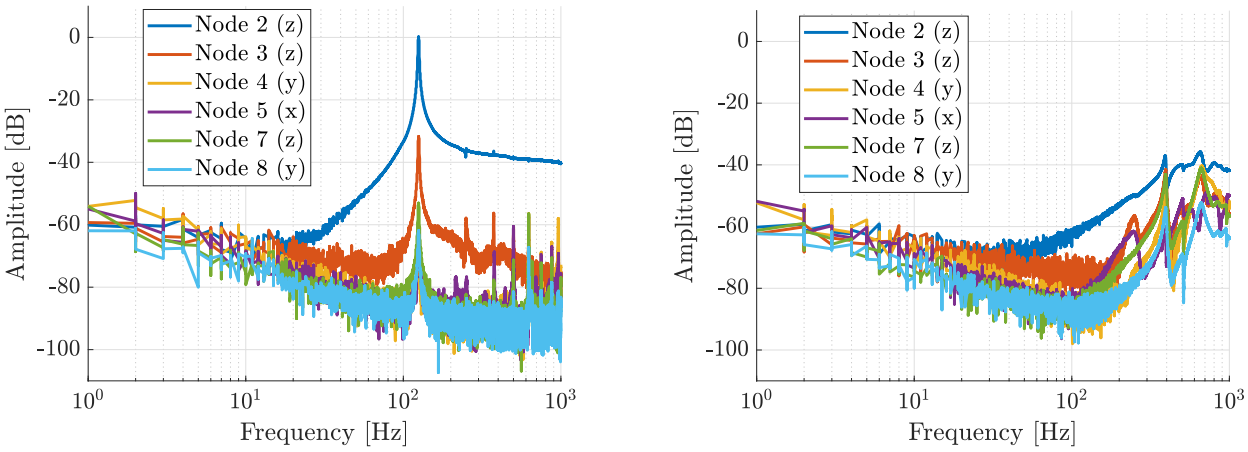

(a) Roving hammer: No contact pressure

(b) Roving hammer: With contact pressure

Figure 3.2.3: Experimental response for two loading cases

Another observation from the roving hammer test, is that the sensors located at nodes 7 and 8 show a low amplitude for both loading conditions, meaning that the back support can be assumed to be rigid. Compared to Figure 3.2.1b, all responses have a lower absolute amplitude which is caused by different scaling of the data. It can however be seen that the sensors follow the same trend, with the sensor on the driving block having a resonance at 151 Hz. This is higher than the numerical resonance of the first mode, which could possibly be explained by a difference in material properties and contact definition between the experimental setup and the numerical model. When moving to higher frequencies, starting from 400 Hz to 1000 Hz a similar trend in accelerance is seen between the two data sets. The numerical data shows sharper peaks, which is attributed to a set damping coefficient of 0.01, while in real life this damping may not be proportional and has or may have a different value, resulting in more damped peaks. However the shape of the response, especially of the first sensor on the driving block, bears resemblance. To achieve a better understanding of the mode shapes and correlation between numerical and experimental data, a MAC analysis is performed.

3.2.3 Correlation numerical and experimental model

To determine what eigenfrequencies and mode shapes are present in the assembled test setup, the sensor data is processed in FEMtools to acquire the modal parameters. In the FRF of each sensor, the peaks correspond to a certain natural frequency and accompanying mode shape. Once all peaks have been identified and the modes stored, an autoMAC is used to determine which modes have a high correlation and may thus describe the same mode. Where possible, similar modes are rejected from the experimental data to achieve a MAC which primarily consists of orthogonal mode shapes. What is left is a reduced modal approximation of the test data, which shows the behaviour of the testing setup over a certain frequency range. The reduced autoMAC of the assembled device is given in Figure 3.2.4a. The first three modes have a low autoMAC value with each other making them

nearly orthogonal to each other, and thus each identified mode describes a different mode shape of the system. This is a positive conclusion, since the first identified mode has an eigenfrequency of 118.3 Hz, but the second already has an eigenfrequency of 246.9 Hz. From this autoMAC it can thus be concluded that the first three modes are distinct from each other, but their proximity to each other may result in higher-order modes effects in the desired test range.

With both mode shape vectors known of the numerical model and the experimental setup, a correlation analysis can be made as described in section 2.4. The constructed MAC is displayed in Figure 3.2.4b. The properties of the modes used for this MAC are described in Table 3.3 and an overview of the participation factor and effective mass in each principle axis is given in Appendix D.

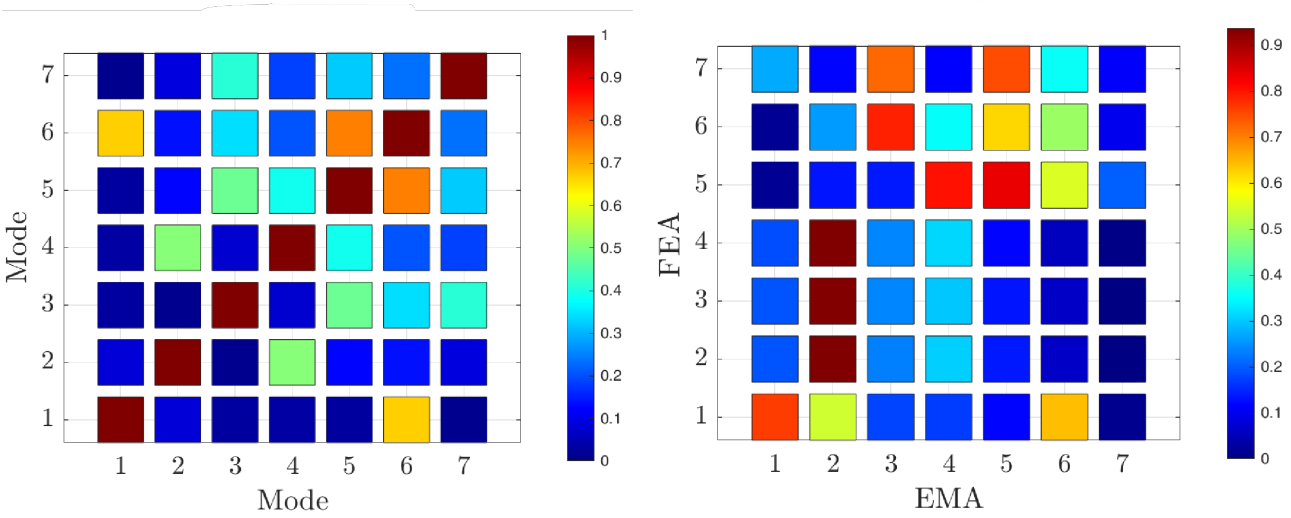

(a) AutoMAC of experimental data

(b) MAC between experimental and numerical data

Figure 3.2.4: autoMAC for EMA and MAC between EMA and FEA

Table 3.3: Modes compared during MAC analysis

Mode	**Numerical frequency** [Hz]	**Experimental frequency** [Hz]	**Type**	**Axis**
1	118.3	126.1	Translational	z
2	246.9	252.08	Bending	y
3	344.5	374.2	Bending	y
4	356.6	387.56	Bending	y
5	365.6	526.62	Bending	x
6	461.5	626.9	Bending	x
7	539.1	750.6	Bending	y

This MAC shows that there is a correlation between the first and second modes of the experimental and numerical data, but higher-order modes seem to have no correlation. This is most likely due to the misalignment of modes at higher frequencies, which are difficult to distinguish from each other due to noisy sensor data and insufficient energy to excite higher-order modes. However, as stated before only the first two modes act within the desired frequency range. It can thus be concluded that the system behaves mostly like the modelled system for frequencies up to 200 Hz, and based on the experimental data the system is validated up to 200 Hz, after which the second parasitic mode renders most experimental data unusable.

3.3 Concluding remarks

From both the design phase and the validation stage it can be concluded that the constructed device functions adequately, meeting most requirements. During assembly, it did became apparent that the normal force plungers are only able to exert 36 N each onto the surface, so a maximal normal force of 72 N can be used during testing. If the effect of larger contact pressures need to be investigated, different force plungers need to be installed. Furthermore, while the requirement on the frequency range was set to 0 - 150 Hz, the system is validated up to 200 Hz based on the experimental data of the constructed device and MAC correlation. However, since the resonance of the mobile stage changes with contact pressure, during the experiments these resonance peaks need to be identified for each normal force level.

Chapter 4

Experiment design and data analysis

This chapter will elaborate on how the measurement data acquisition system works, what type of data is gathered from the testing device and how this data is subsequently processed. The various methods of data filtering will be discussed from which the desired hysteresis curves are constructed. It will further elaborate on the design of the experiments and why certain input parameters are of interest. The chapter will close with a discussion on the validity of the data processing and preliminary results of the experiments.

4.1 Experiment design

With the testing device assembled and validated, the experiments in which different loading and interface conditions are applied need to be designed. The different experiments take into account the following variables:

- **Range of contact area:** To investigate what effect a change in contact area has on the contact properties, the three blocks as described in section 3.1 are used. Due to the complexity of the blocks and the limited time, only these three specimens are available for testing. This means that each block needs to be assembled and tested for all different parameters, before switching to the next specimen. Due to the large excitation and loading forces, the surfaces will experience fretting which renders the specimens unusable after disassembling. If the same contact area needs to be tested in the future, additional specimens will need to be produced.

- **Range of normal force:** As explained in section 3.1, the normal force onto the surface will be delivered by two force plungers on each side of the contact. Since these plungers apply force linearly with each rotation of the screw, the different levels of normal force will be corresponding to degrees of rotation. The experiments will vary in normal force levels ranging from 0 N, where the ball point is just touching the surface, up to 72 N where both springs are almost completely compressed and each applies a force of 36 N onto the stages. Note that both force plungers are always in the same position, which otherwise would result in uneven loading conditions.

- **Range of cyclic motion:** The motion of the driving block is due to the cyclic force exerted onto the leaf spring by the shaker. To have a range of displacement, the shaker input voltage can be set to multiple levels. The level is determined by the acquisition panel, after which it is amplified and sent into the shaker. The level of the amplifier is not changed over the entire range of experiments, which would otherwise result in different excitation forces between tests. The lowest panel input is set to 0.6 V, which in combination with the amplifier corresponds to a peak force of 40 N. The highest panel input is set to 1.8 V, which corresponds to a peak force of

roughly 75 N. To obtain a high enough resolution between displacement levels, an increment between experiments of 0.3 V is chosen.

- **Range of excitation frequency:** One of the main areas of interest is to investigate if the contact properties change with displacement frequency. The experiments will range from 15 Hz up to 150 Hz, to investigate the effect of excitation frequency on the contact properties. From the validation of the device, a resonance in the desired motion was detected which changes with contact pressure. Therefore, during the experiments also the frequency at which this resonance occurs will be documented. To obtain an adequate resolution between experiments, a frequency interval of 3 Hz is chosen to be sufficient.

The contact blocks are constructed from 7060-grade aluminium, on which a roughness test will be performed before and after testing, to determine how the surface roughness has changed during the experiments. These roughness profiles are presented in Appendix B. In future research, blocks constructed from varying materials can be tested to determine the effect of material properties on the contact properties.

4.2 Data acquisition and processing

4.2.1 Initial measurements

During experiments, a custom-developed program will excite the system using a National Instruments 9234 sound and vibration capture card over the predetermined range of frequencies and voltages. Simultaneously, it records the acceleration of both contact surfaces and the forces on the contact at a sample rate of 10 kHz. To ensure that no non-linear excitation effects are present in the system, the cyclical excitation signal increases linearly from zero to its maximum value in one second at the beginning of the test. This is to ensure that no immediate large forces are exerted on the surface, which may lead to fretting and excessive wear of the surfaces. This also ensures that the individual consecutive tests have no influence on each other, since at the end of one certain test the signal returns to 0 V. A visualisation of this excitation signal is given in Figure 4.2.1a.

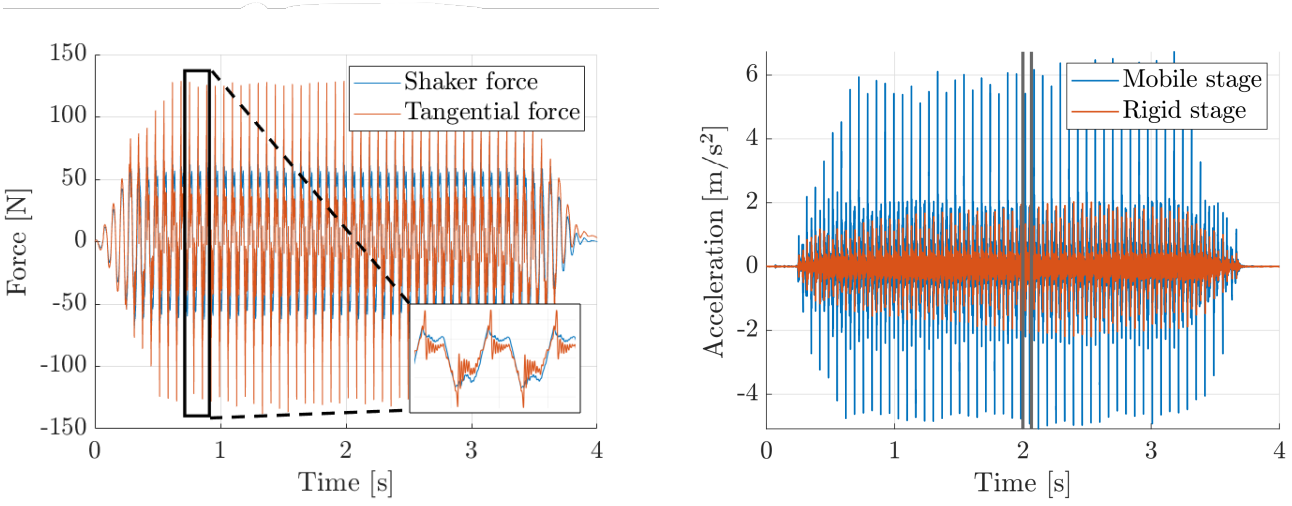

(a) Measured forces

(b) Raw acceleration of both stages

Figure 4.2.1: Input and output signals during measurements

To construct a hysteresis curve, first the acceleration data of both stages needs to be integrated twice. Subsequently, the difference in displacement is calculated to find the relative displacement between the two surfaces. Together with the directly measured tangential force, a hysteresis curve can be created. Only a single cyclical motion during steady state motion is needed to construct the curve, thus the area indicated by the black bars in Figure 4.2.1b is selected. The resulting hysteresis curve is depicted in Figure 4.2.2a. Compared to the hysteresis curves found in literature, an example is given

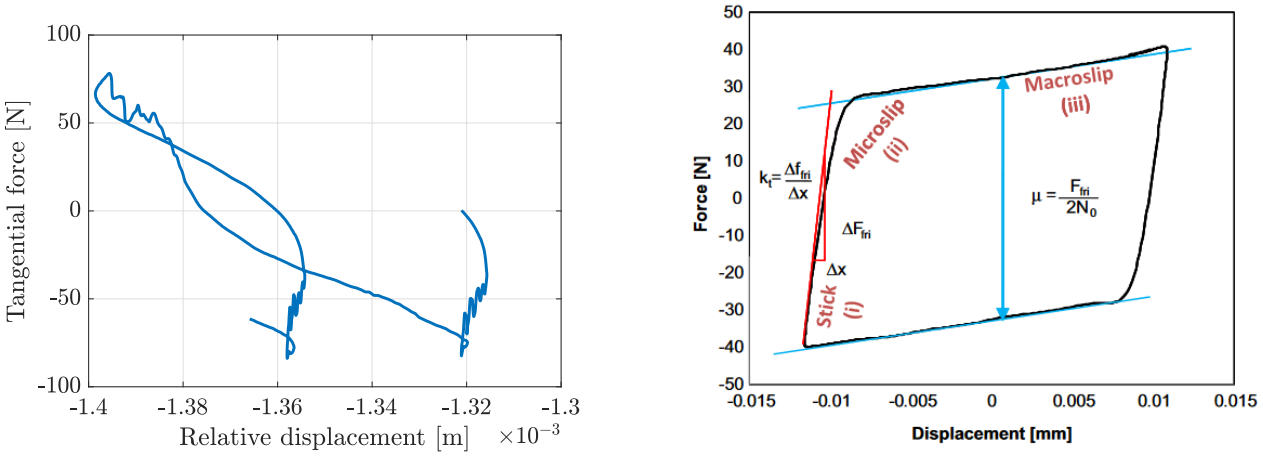

(a) Hysteresis based on raw experimental data

(b) Hysteresis curve from literature [8]

Figure 4.2.2: Comparison between experimental hysteresis and hysteresis found in literature

in Figure 4.2.2b, it shows that the raw experimental data is unable to present clear region distinction, and produces an unrecognisable shape. Furthermore, when plotting multiple loops, it shows that the consecutive curves are moving away from one another, which is an effect not present during steady-state cyclical motion. To prevent this effect from occurring, the acceleration and tangential force data need to be processed using filtering techniques, which will be explained in detail in the next section.

4.2.2 Data processing

To visualise the multiple processing steps performed on the raw data, a single data set has been chosen. This data set contains the data where the smallest contact area is tested, with a normal force of 18 N. This specific visualisation is for the test performed at 1.8 V and 48 Hz.

To construct the hysteresis loop, the relative displacement needs to be extracted from the acceleration data of both sensors placed on the individual surfaces. To extract the displacement of each block from this acceleration, a cumulative trapezoidal integration scheme is applied twice. This technique is validated by comparing the results to an analytical solution for a simple sinusoidal function and a numerical time integration scheme using Simulink, which both returned the same result. However, when directly applying this integration scheme to the raw data from the experiments, a displacement profile as visualised in Figure 4.2.3a is obtained. For clarity, the Fast Fourier Transformation (FFT) of the raw acceleration of the driving surface is also given in Figure 4.2.3b.

This displacement profile shows a large displacement sinusoidal, with a smaller displacement present on top of this sinusoidal which has a higher frequency. This smaller displacement with a higher frequency, which is the driving frequency of the shaker, is the actual displacement of the surface. Since the accelerometers have a finite accuracy, a discrepancy between actual acceleration and measured acceleration is present in the signal. This uncertainty is not constant during the measurement, but is

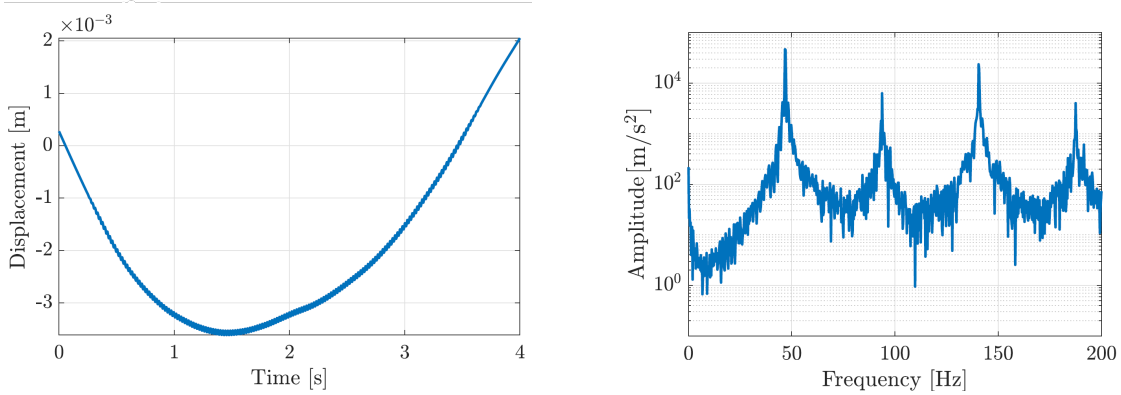

(a) Displacement from raw acceleration data

(b) FFT of raw acceleration data

Figure 4.2.3: Double Fourier Integration results

integrated twice resulting in an integration constant on the displacement curve. This uncertainty displacement is visible in Figure 4.2.3a as a sinusoidal profile with an approximate frequency of 0.28 Hz. To find the actual displacement of the surface, this frequency has to be filtered out of the FFT, after which the double integral can be taken again, effectively removing this integration constant due to sensor uncertainty. Two filtering techniques are discussed, one based on the deletion of low frequencies and one based on the harmonic multiples of the shaker driving frequency. A similar approach is applied to the measured tangential force.

Option 1: Deletion of low frequencies

The first and most straightforward technique is based on deleting the contribution of frequencies lower than the driving frequency from the signal, in this example 48 Hz. Figure 4.2.3a shows that the large displacement curve has a far smaller frequency than the driving frequency, so removing the lower frequencies should result in a more logical, zero mean displacement. The amplitude of the frequencies lower than the driving frequency is set to zero, and by only retaining the frequencies after the driving frequency an FFT displayed in Figure 4.2.4a is created. Here only the area of interest is shown, but all frequencies above 200 Hz up to the Nyquist frequency are also retained in the signal. By using the double integration technique again, the displacement as shown in Figure 4.2.4b is found.

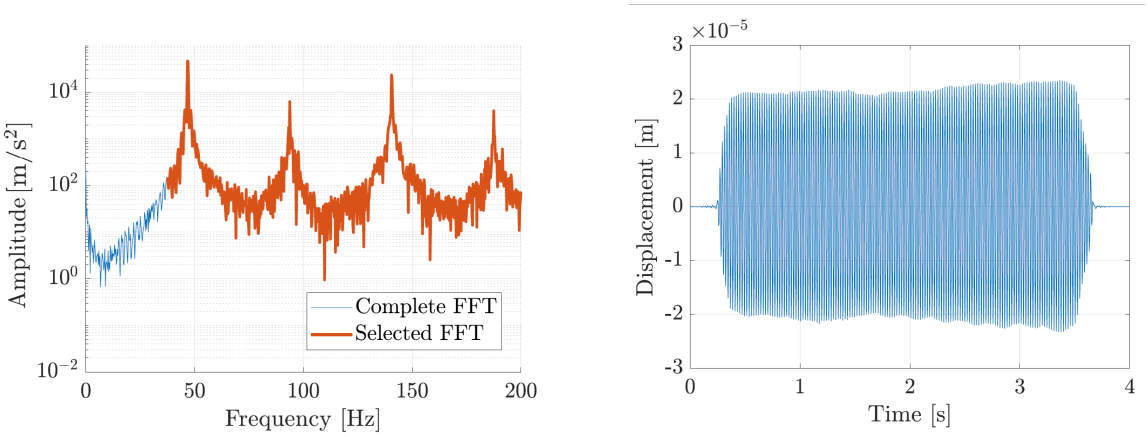

(a) Deletion of low frequent behaviour

(b) Displacement from filtered acceleration

Figure 4.2.4: Filtered signal and resulting displacement

Compared to Figure 4.2.3a this order of magnitude is much more coherent with the simulations and visual observations during the experiment. It is also clear that the displacement is now a zero mean signal, which is in line with the expectations of the testing device. If this would not be the case, the mobile stage would creep further onto the rigid stage, which is not observed during experiments.

By retaining only a fraction of the signal due to the filtering, the overall energy of the signal is diminished. To ensure that the derived displacement is still in the same order of magnitude as the actual displacement of the mobile stage, the signal is scaled up to match the original acceleration data. This scaling is a constant factor, which is determined by extracting the maximum value of the original acceleration data for the window in which the hysteresis is evaluated. Then the magnitude of the filtered data at that point is extracted, from which the scaling factor is determined. The scaling factor is subsequently applied to the entire filtered acceleration data, after which the signal is a near-perfect match with the original acceleration data. The scaling factor for all experiments lies between 2 and 2.3, where 2 is the minimum amplification due to the removal of all frequencies above the Nyquist frequency, and the remaining constant is dependent on how much frequencies are retained based on the filtering technique. A comparison between the filtered acceleration signal for the mobile stage, and the raw acceleration is displayed in Figure 4.2.5a, and the resulting hysteresis curve based on the filtered data is shown in Figure 4.2.5b.

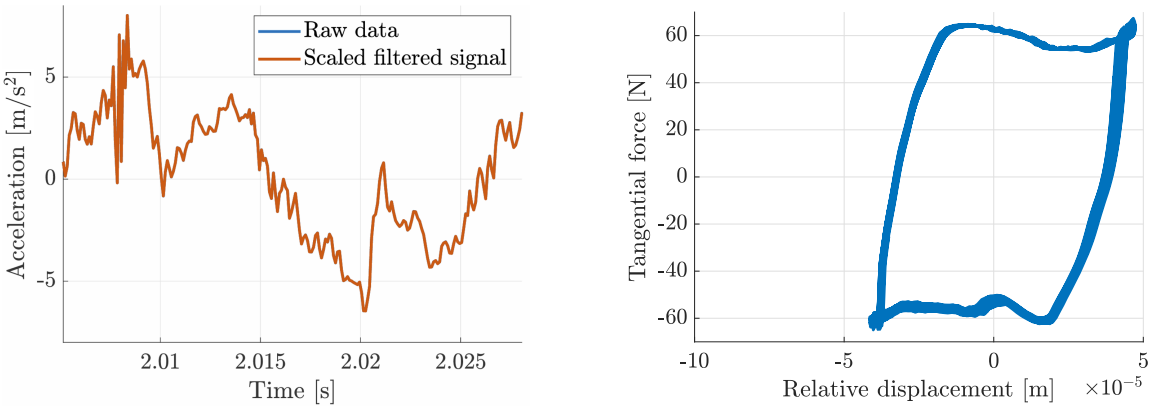

(a) Deletion of low frequencies

(b) Resulting hysteresis curve

Figure 4.2.5: Filtered acceleration profile and resulting hysteresis curve

Figure 4.2.5a shows that the filtered signal is almost indistinguishable from the raw experimental data. Furthermore, note that the hysteresis in Figure 4.2.5b is plotted for multiple cycles, while the hysteresis curve follows the same trajectory for each cycle. This is an expected result since during steady state motion the hysteresis curve should form a closed loop.

Option 2: Filtering based on driving frequency

A second selection technique is based on the driving frequency with which the device is excited. This technique only permits the primary excitation frequency and the harmonic multiples of this frequency to be retained in the filtered signal. This is to remove the noise inherited by the frequencies with a small amplitude, and based on the philosophy that the driving frequency and its non-linear harmonic multiples capture the essence of the original signal. First the driving frequency is determined, after which all multiples up to the Nyquist frequency are selected. Subsequently, a band of frequencies is selected around these frequencies. This is to ensure that enough of the non-linear effects are taken into the signal, and not only the exact driving frequency multiple.

As can also be seen in Figure 4.2.3b, around each multiple frequency there is a band of higher amplitude frequencies which also contribute to the characteristics of the signal. A visualisation of the selected frequencies is given in Figure 4.2.6a, again with the corresponding displacement found in Figure 4.2.6b.

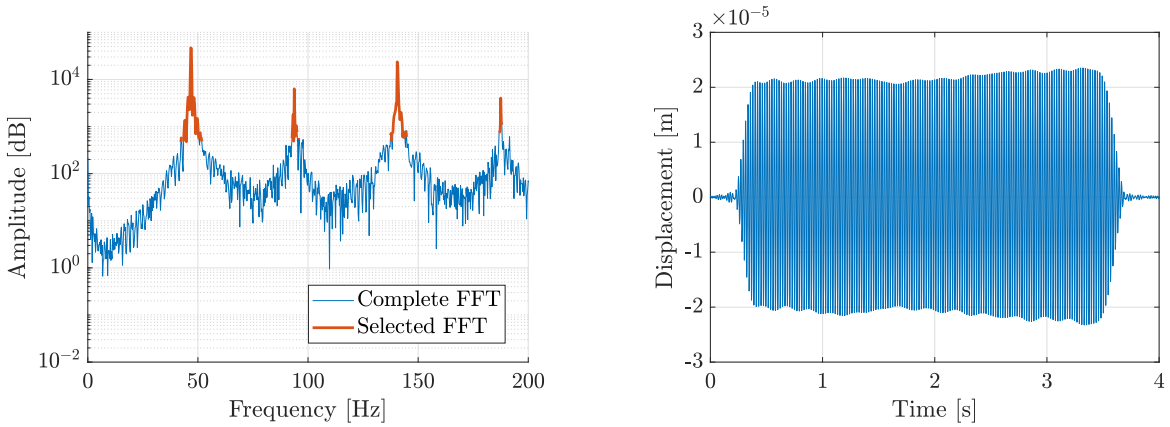

(a) Deletion of low amplitude frequencies

(b) Displacement from filtered acceleration

Figure 4.2.6: Filtered signal and resulting displacement

This filtering technique solely focuses on the driving frequency and the non-linear effects due to its harmonic multiples, which may present a more accurate representation of the original signal compared to retaining all frequencies above the driving frequency. Again the scaling technique discussed in the previous filtering approach is used to obtain an accurate representation of the original acceleration data. Figure 4.2.7a shows the comparison of this filtered acceleration data with the original experimental data, and Figure 4.2.7b shows the corresponding hysteresis curve.

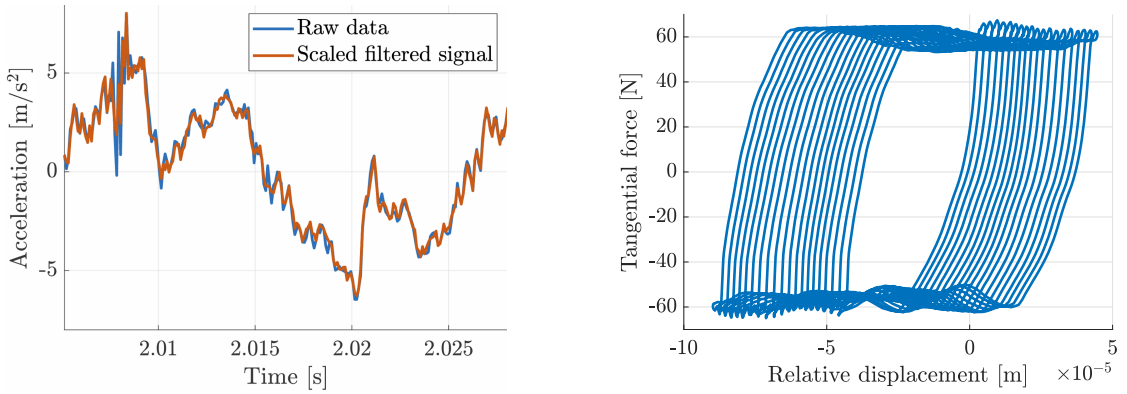

(a) Selection of harmonic frequencies

(b) Hysteresis based on second filtering technique

Figure 4.2.7: Comparison between raw and filtered acceleration and corresponding hysteresis

Figure 4.2.7a shows that the filtered acceleration deviates from the original acceleration, more then when the first filtering technique is used. This can be explained by the fact that the contribution of more frequencies is filtered out. However, both accelerations seem to overlay quite well and the filtered signal should be able to capture a correct hysteresis curve. Figure 4.2.7b shows however that even though the hysteresis curve is well defined and the three individual regimes are clearly distinguishable, plotting multiple cycles results in a mobile hysteresis loop. It was attempted to remove this motion by retaining more frequencies, but the results did not further improve.

In conclusion, even though both methods seem to be applicable, the first filtering technique based on the deletion of only the frequencies lower than the principal driving frequency gives the best results and shall be used during experiments. The acceleration profile is nearly identical to the experimental data, and the three individual regimes are distinguishable in the hysteresis curve, while no movement between multiple hysteresis cycles is present. This technique was further verified with different driving frequencies and input voltages, which yielded similar results.

Filtering of the tangential force

During the first experimental measurement, the data showed that the tangent force sensor was measuring a tangent force that varied significantly from the excitation force delivered by the shaker. This is visualised in Figure 4.2.8, where the tangential force is plotted against the input force delivered by the shaker for one hysteresis loop evaluated two seconds into the measurement. When plotting both forces against the filtered displacement, two different hysteresis shapes are constructed, as shown in Figure 4.2.8. The tangential force data shows the inclusion of much more non-linear harmonic

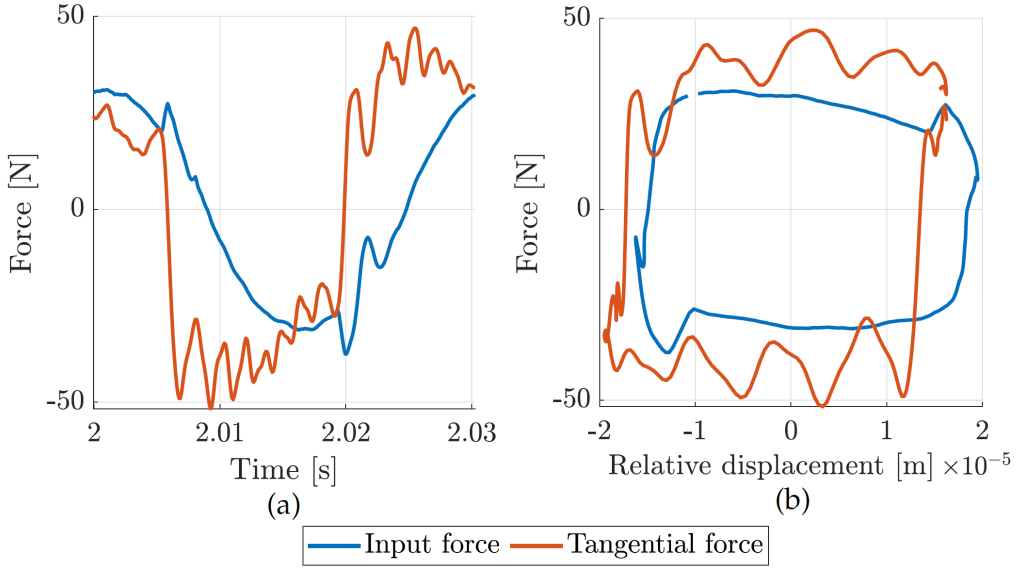

Figure 4.2.8: Both forces and their corresponding hysteresis

frequencies compared to the input force. This non-linear effect is most likely due to the assembly to which the force transducer and the rigid block are connected, which is not stiff enough and introduces unwanted dynamics into the signal. This effect is undesirable since it renders most of the measurements unusable. To construct hysteresis curves on which a more concise conclusion can be drawn, also this signal needs to be processed. From Figure 4.2.8 it becomes clear that a signal consisting of a single frequency or a few harmonic multiples yields the best results, therefore the same approach as for the acceleration data is used. First an FFT is applied to the data, and only the first driving frequency and two following harmonic multiples are retained in the filtered signal. The retention of these three signals provided the best results for a wide range of loading conditions, and will not vary between tests to ensure no differences occur during analysis.

The result is illustrated in Figure 4.2.9. The used filtering technique filters out a significant amount of nonlinear effects, which could result in a poor representation of the original signal. However, without filtering no contact properties can be extracted since no clear distinction between the three stick-slip regimes can be made. To determine the quality of the filtered data, for each experiment the filtered data is compared with the original data, to ensure that the tangential force reaches the same levels and the three regimes are present at the same location within the signal. The importance of these three regimes will be further explained in section 5.1.

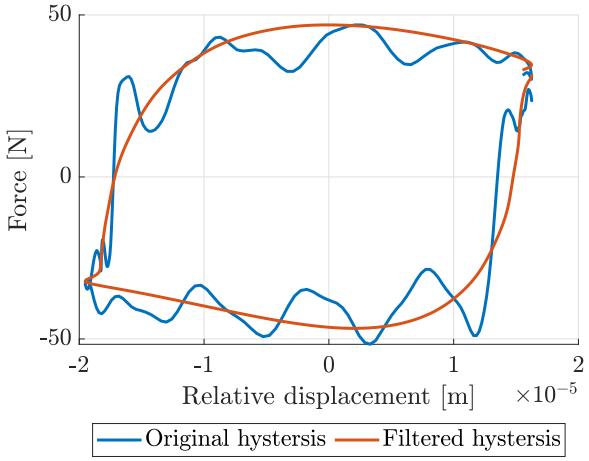

Figure 4.2.9: Comparison between original and filtered hysteresis

4.3 Concluding remarks

Using the filtering technique based on the deletion of low frequent behaviour for the acceleration data and the filtering of the tangential force, a reliable framework has been created. This framework will be used for all experiments, such that no change in contact parameters can be attributed due to incoherent post-processing of the data. From these hysteresis curves the contact properties at various combinations of contact conditions will be determined. Which hysteresis curves are created during the experiments, how the contact properties are extracted from these hysteresis curves and the difficulties experienced performing the experiments will be elaborated on further in chapter 5.

Chapter 5

Experimental results

This chapter focuses on the results gathered from the experiments as described in the previous chapter. It will elaborate on how the different contact properties are extracted from the hysteresis curve and will give various examples of hysteresis curves over the ranges described. It will further discuss the main challenges during the experiments, and additional comments on the collected data. This will create an understanding of the validity of the measurements, from which a more detailed trend analysis on the test data will be provided in chapter 6.

5.1 Hysteresis analysis

Before extracting any contact parameters from the hysteresis curves, first an understanding of the general shape of a hysteresis curve needs to be created. A standard hysteresis loop consists of three regions, as shown in Figure 5.1.1 where a hysteresis loop captured with the testing device has been annotated to indicate each section.

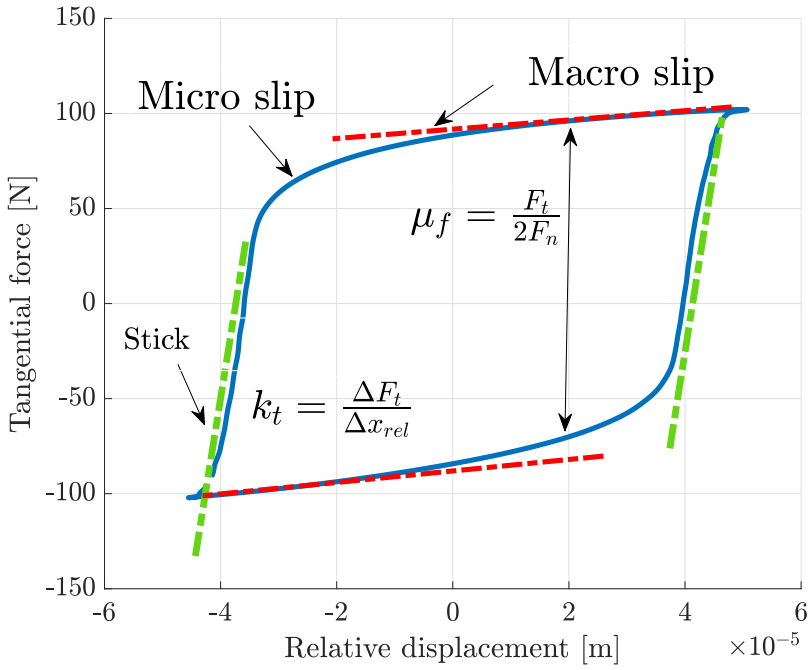

Figure 5.1.1: Different regimes in hysteresis

The force varies linearly with the relative displacement between the blocks while in the stick regime, and only elastic deformation occurs on the contact surface. When the displacement between the two surfaces increases, a fraction of the asperities lose adhesion and start sliding, which is called the micro slip regime. If the displacement between the two surfaces increases further the entire contact starts sliding, which is called the macroslip regime [10]. Figure 5.1.2 shows an example of multiple types of hysteresis curves taken at various frequencies and voltages, all with different shapes and properties.

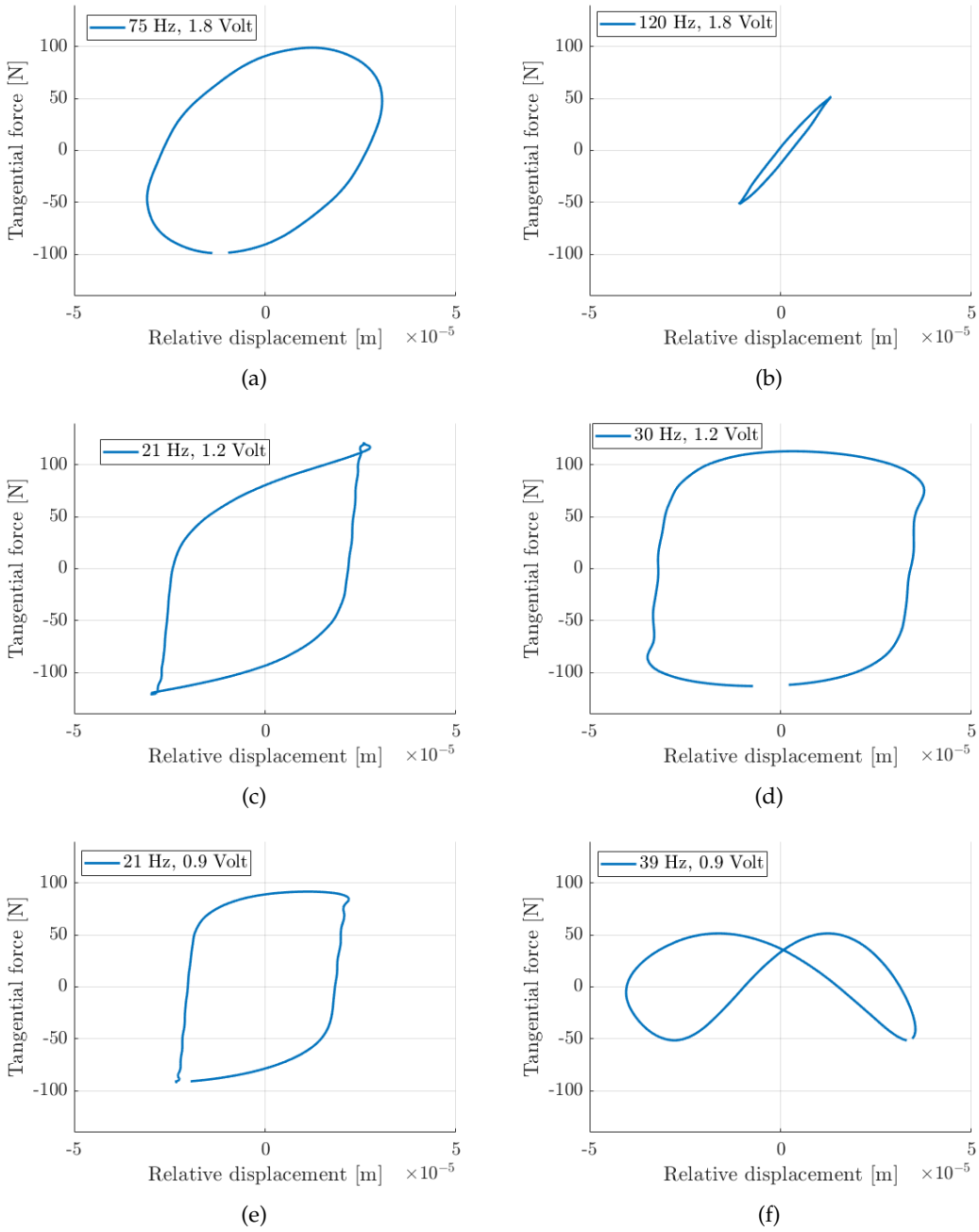

Figure 5.1.2: Different hysteresis curves

Compared to Figure 5.1.1 it is clear that not all of these examples show a clear distinction between the separate regimes. To be able to draw conclusions on the experimental data, care needs to be taken

which hysteresis curves are labelled as reliable due to their distinctive shape, and which ones are discarded as unusable measurements. A measurement can be unusable due to a variety of reasons. One reason is a misalignment issue between the two contacts, which results in an unpredictable contact area and therefore an unclear hysteresis curve. Another reason could be a filtering effect, where the filtering technique is unable to reconstruct the original data without removing the overarching trend. To ensure that only conclusions are drawn from reliable data, each curve is manually inspected and given a reliability rating. Additionally, each contact parameter extracted from the hysteresis curve is manually calculated to ensure that the information extracted from each curve is as reliable as possible. For the examples in Figure 5.1.2, (a) and (f) would be discarded since no clear distinction between stick, micro slip and macro slip can be found. (b) would be labelled as only containing elastic or stick behaviour, so the tangent line is simply taken between the minimum and maximum tangential force. For (c), (d) and (e) a distinction between the three regimes can be made, so these hysteresis loops are regarded as correct and taken for further trend analysis. The reliability rating for the experimental data used in this research is presented in Appendix C.

5.1.1 Tangent stiffness

To find any trends or correlations between experiments, first all the contact properties need to be extracted from the hysteresis curve. First the tangential contact stiffness (k_T) is extracted, which is defined as

$$k_T = \frac{\mathrm{d}F_T}{\mathrm{d}s} \tag{5.1}$$

in which

- F_T is the force transmitted through the contact
- s is the sliding distance between the surfaces

The tangential contact stiffness presents itself in the hysteresis curve as the tangent of the stick region. Especially in Figure 5.1.1 the stick region is clearly defined as a straight line after reversal of the cyclical motion. It is also clear where the microslip and macroslip regions begin and end, as explained in subsection 2.4.4. However, if the hysteresis loop is not as clearly defined, due to for example misalignment, adhesion between surfaces or excessive wear, the tangent of the stick region might be difficult to obtain. As an example, observe the two different tangent line possibilities presented in Figure 5.1.3.

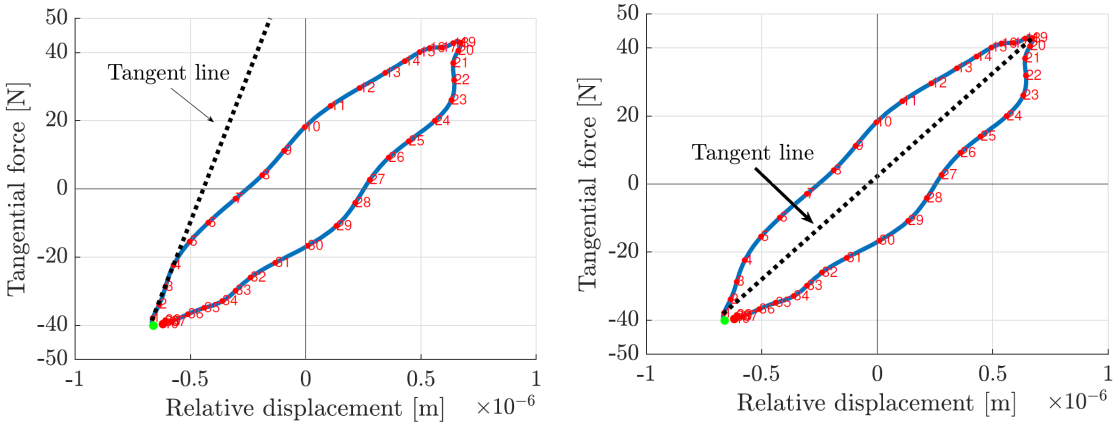

(a) First tangent line

(b) Second tangent line

Figure 5.1.3: Two possible tangent lines

Since the micro slip region is not properly defined, and it seems that there is either a small micro slip region or a small stick region, it is difficult to determine how the stiffness coefficient can be determined. Also when looking at the value of the tangent stiffness, the first tangent line, shown in Figure 5.1.3a, shows a value of $1.73{\cdot}10^{8}$ N m^{-1} and the second tangent line, shown in Figure 5.1.3b, shows a value of $6.06{\cdot}10^{7}$ N m^{-1}. This shows that the tangential contact stiffness can vary significantly depending on where the stiffness is evaluated. For lower excitation voltages, such as this example, it shows that there is almost no displacement between the two contact blocks, which results in a hysteresis curve that only captures the elastic region behaviour of the contact interface. In this situation, the most reliable technique is to use the second tangent line shown in Figure 5.1.3b, since a clear minimum and maximum can always be distinguished. This is also used in literature to capture the stiffness for small oscillations [20]. Once more displacement is forced onto the contact, by means of raising the voltage, the hysteresis curve assumes the form displayed in Figure 5.1.1. This effect can clearly be observed in Figure 5.1.4.

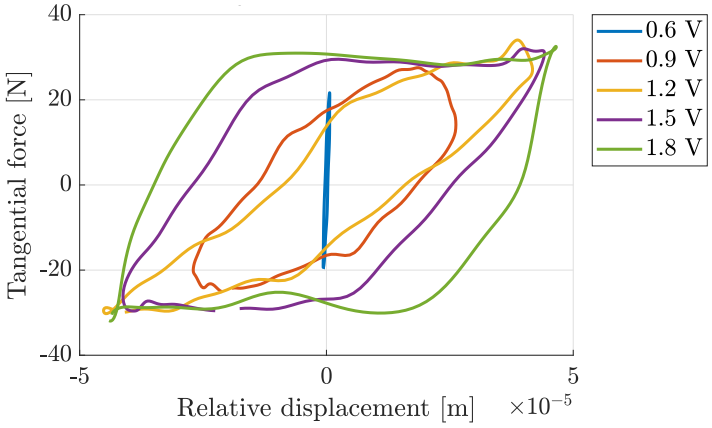

Figure 5.1.4: Development of hysteresis curve

The experiments are divided into datasets, where each set contains information of all frequencies and voltages for a specific contact area and normal force. When all the stiffness coefficients are extracted and plotted against one another, a clear stiffness line can be observed. For this example, the data set of the smallest surface with a normal force of 36 N is used and displayed in Figure 5.1.5.

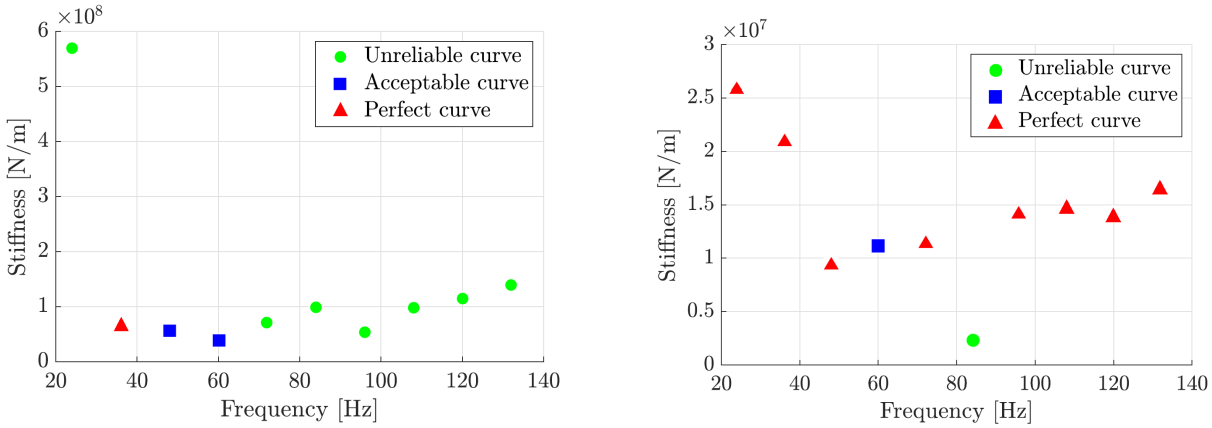

(a) Stiffness at 0.6 V

(b) Stiffness at 1.8 V

Figure 5.1.5: Stiffness development of small surface

As mentioned previously, each stiffness measurement is indicated with a reliability score, which expresses if the measurement is valid. Comparing both input voltage levels displayed in Figure 5.1.5, it shows that the measurements performed at the highest input voltage are more reliable than the measurements at the lowest input voltage. This is explained due to the fact that at the lowest input voltage, the system does not reach the required force for macro slip before the force changes direction, resulting in a very small displacement of the driving block. Since from these small oscillations no reliable measurements can be taken, these are all indicated as being unreliable hysteresis curves. At the highest input voltage level however, the force reaches the macro slip threshold far before reaching the peak excitation force, resulting in large displacements and reliable hysteresis curves. This trend can again be seen in Figure 5.1.4, where the low voltages have a much smaller surface area than the higher input voltage levels. Further investigation of trends between measurements will be given in chapter 6.

5.1.2 Normal stiffness

While tangential stiffness describes the displacement of two surfaces against a tangential force on the contact, normal contact stiffness describes the displacement of two surfaces against a normal force acting on the joint. In operations where non uni-axial loads are applied to the surface, predicting the normal contact stiffness will also further increase the accuracy of the system. Since this setup is configured to extract the tangential stiffness only, finding a relation between the experimental contact stiffness and normal stiffness can provide insight into the development of normal contact stiffness under varying loading conditions. Sherif and Kossa [21] determined that the normal and tangential contact stiffness relation is a function of the Poisson's ratio between two materials, based on the Greenwood and Williamson contact theory,

$$\frac{k_n}{k_t} = X\Phi(\nu) = \frac{\pi}{2}\frac{(1-\nu)}{2-\nu} \tag{5.2}$$

Other approaches in literature provided relationships identical to Equation 5.2, however with different values for X [22]. Yoshioka and Scholz [23] obtained a value of $X = 0.71$, while contact models by Baltazar et al. [24] expressed the coefficient as $X = \frac{2\epsilon}{\kappa}$, where ϵ and κ are factors correcting for misalignment with respect to shear and longitudinal direction. Raffa et al. [22] compared these models with experimental data and concluded that the stiffness ratio has a significant dependence on the contact pressure, especially at low contact pressures.

While these models can be used to determine the normal contact stiffness based on tangential contact stiffness, the uncertainties such as asperities deformation, adhesion and the varying real contact area can lead to an incomplete representation of the normal stiffness within a contact. Furthermore, all research into this field has been performed for small contacting areas in the order of a few squared millimetres, which does not scale to applications in industry, where large contact areas are present within systems. To achieve a correct prediction for the contact stiffness, a similar approach as extracting the tangential contact stiffness should be applied, where experiments at various loading conditions should be executed to extract the normal contact stiffness.

5.1.3 Dissipated energy

Another intrinsic property of the hysteresis curve is that it captures how much energy is dissipated in the contact interface during one cyclic motion by calculating the surface area of the hysteresis curve. This dissipated energy is due to the slipping of the surfaces, which transforms the kinetic energy of the device into heat. If a pulse would be given to the system and the contact was allowed to freely dissipate all energy, an approximation of the damping coefficient could be obtained, assuming that

the contact behaves as a spring-mass-dashpot system. A simplification of the relation between the damping coefficient and the kinetic energy is given by

$$E_k = \frac{1}{2}kA^2[e^{-\zeta\omega_n t}(\zeta\cos(\omega_d t) + \sqrt{1-\zeta^2}\sin(\omega_d t)]^2. \tag{5.3}$$

The full derivation is given in subsection 2.4.5. To determine the area underneath the hysteresis curve, a cumulative trapezoidal integration scheme is used. Using the same data set used to determine the stiffness, the development of dissipated energy over frequency is plotted in Figure 5.1.6a.

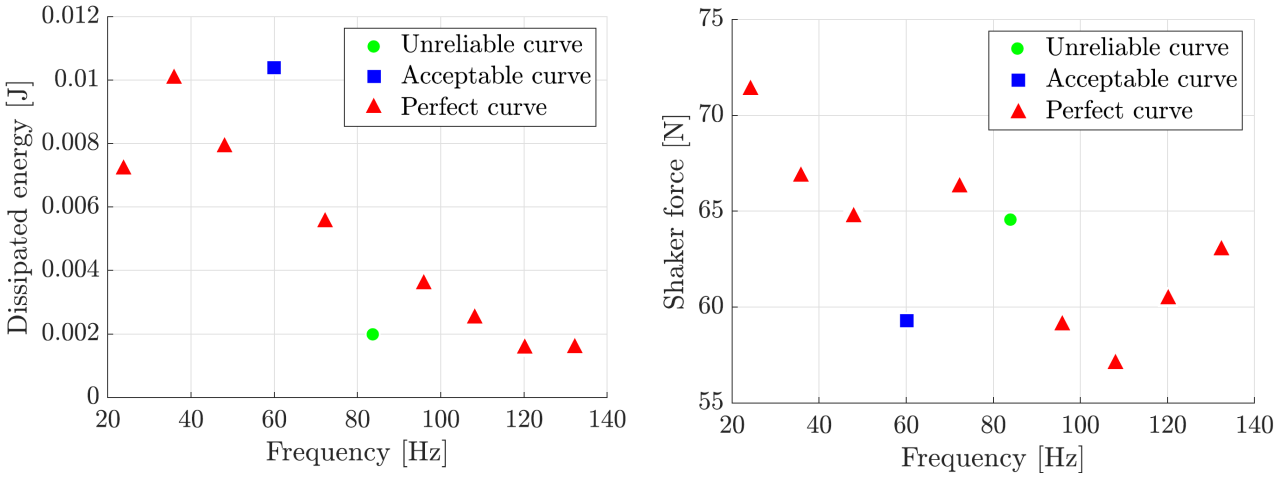

(a) Dissipated energy at 1.8 V

(b) Excitation force at 1.8 V

Figure 5.1.6: Dissipated energy measurement

Eventough in this measurement it seems that the dissipated energy decreases with increasing frequency, when comparing it to the input excitation force given in Figure 5.1.6b it shows that it follows the same trend. Upon further investigation it was concluded that the shaker decreases in excitation force with increasing frequency, which results in a decreasing dissipated energy. This effect also surfaces when examining the hysteresis loops of one measurement, where an increase in frequency results in a diminishing macro slip stage, resulting in a smaller surface energy. This effect will be further discussed in section 5.2, and any conclusions that can be drawn on this data will be discussed in chapter 6.

5.1.4 Friction coefficient

The last property that can be extracted from the hysteresis curve, is the friction coefficient experienced within the contact interface. By extracting the tangential force value at the horizontal section of the hysteresis curve, i.e. the macroslip region, and dividing it by the applied normal force this value can be obtained. This is described as

$$\mu_f = \frac{F_t}{2N_0}. \tag{5.4}$$

The normal force is here described as the force exerted on the system by one spring plunger, and subsequently multiplied by two. Similar to the contact stiffness and the dissipated energy, for each cycle the tangential force value is manually extracted and given a reliability score. Further trend analysis on the friction coefficient will be performed in the next chapter.

5.2 Experimental challenges

During the measurements of the experiment matrix, several undesirable traits of the testing device have been identified. Before conducting any analysis between measurements, these issues will need to be explained in detail to construct an understanding of where several effects originate from.

5.2.1 Compliance of the shaker

When creating the numerical model, the input force was assumed to be ideal and acting directly in line with the contact area. However, during initial experiments, the appearance of a resonance peak in the stiffness was detected around 59 Hz for each contact area block, regardless of input voltage or normal load. This stiffness behaviour is displayed in Figure 5.2.1a. Here only the stiffness development for the smallest contact area has been plotted, but the other two contact areas displayed a similar behaviour.

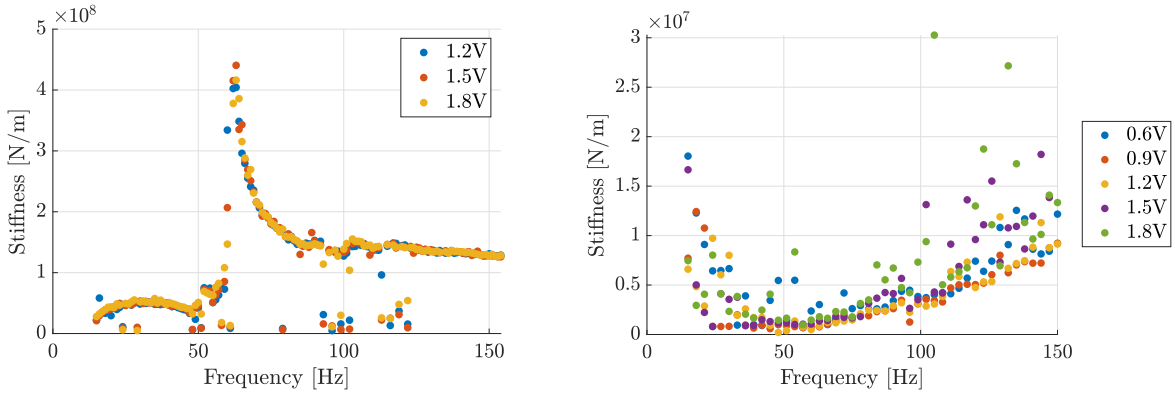

(a) Stiffness without reinforcement

(b) Stiffness with reinforcement

Figure 5.2.1: Stiffness for both configurations

Since a resonance in the stiffness versus frequency response equals an anti-resonance in the accelerance of the system, it showed that the force produced by the shaker was in fact used to excite the shaker itself instead of the contact interface. Therefore, a reinforcement structure to constrain the shaker was needed. By means of readily available materials a rudimentary support structure was constructed around the shaker. This structure is presented in Figure 5.2.2.

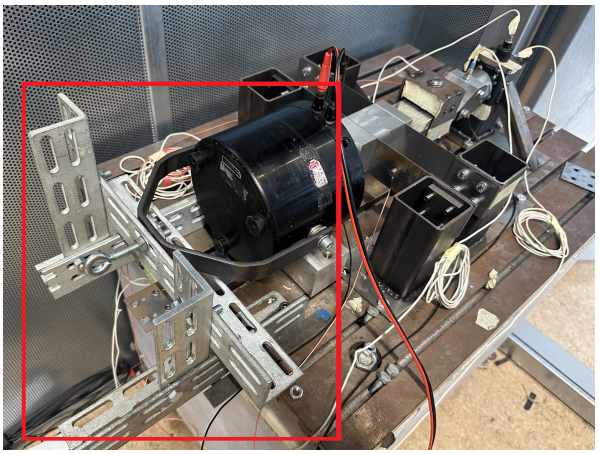

Figure 5.2.2: Additional reinforcement structure

The result of this added structure was a successful increase in the system's stiffness. The resulting stiffness for the same contact conditions is given Figure 5.2.1b. Here it can be seen that the resonance peak has completely disappeared, and the operating range of 150 Hz is free of unwanted dynamic behaviour. Figure 5.2.1b also shows that for higher input voltages, i.e. higher excitation forces, the stiffness measurements become much more scattered with regard to the lower input voltage levels. The hysteresis loops also show more inconsistency in shape and size, which is in part due to the increased displacement of the blocks and the inherent non-linear effects that those large displacements entail. Figure 5.2.1b also shows an increase of stiffness with an increase in frequency. This effect is also observed in other contact loading conditions and will be elaborated on further in chapter 6.

Now that the stiffness is examined and determined to be reliable, an additional check can be performed on the input force, tangential force and raw acceleration of the system. This will help to determine the validity of the measurement range, and if any undesirable effects are present. The following analysis is performed on the smallest contact area, with a normal force of 36 N. Figure 5.2.3a shows the force measured by the force transducer in plane with the contact, which thus effectively shows the tangential force in the contact. Each data point in this graph is determined by finding the maximum force value of the hysteresis loop and plotting this for the entire measurement range. There is not a clear trend visible in this data, and the data seems to have little to no coherency. One conclusion that can be drawn, is that at lower input voltages, the tangential force seems to have a smaller variance, while at higher input voltages this variance increases. Furthermore, the tangential force seems to saturate at a voltage level of 0.9 V. At higher voltages, the tangential force does not vary much in amplitude for each voltage level. This is to be expected since the tangential force will only increase until the macro slip region is reached, after which it will start sliding under the same tangential force. From this data it is clear that for this specific dataset, the contact reaches the macro-slip region only after voltage levels higher than 0.9 V.

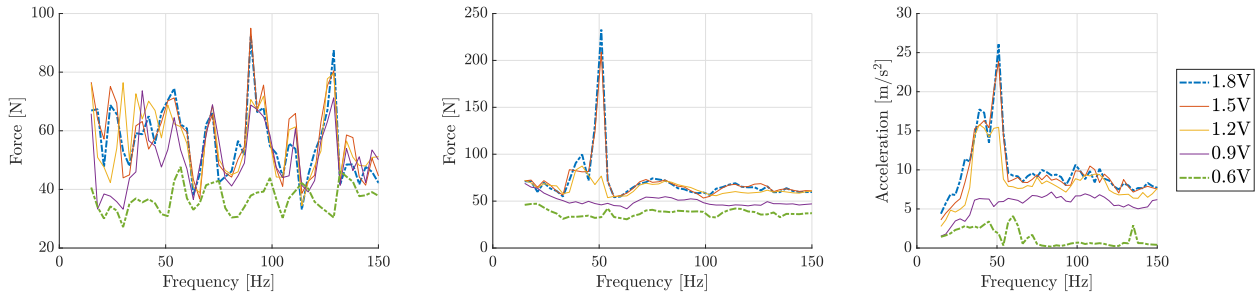

(a) Measured friction force (b) Shaker input force (c) Acceleration of moving block

Figure 5.2.3: Response of the testing device

Figure 5.2.3b shows the input force delivered by the shaker directly onto the leaf spring. A clear trend is visible that a larger force is exerted onto the leaf spring when the input voltage is increased, as is expected. For voltages higher than 0.9 V however, also a sharp peak appears at 50 Hz. Based on visual observation of the shaker vibrating at this frequency, this peak in acceleration is unfortunately still due to the compliance of the shaker, and is not mitigated by the reinforcement structure. This is directly related to the acceleration of the driving block, as shown in Figure 5.2.3c, where at the same frequency and voltage, a sharp increase in acceleration is visible.

To understand what this acceleration profile implies for the hysteresis shape, four frequency points and three voltage levels have been studied varying over the measurement range, and the results are presented in Figure 5.2.4.

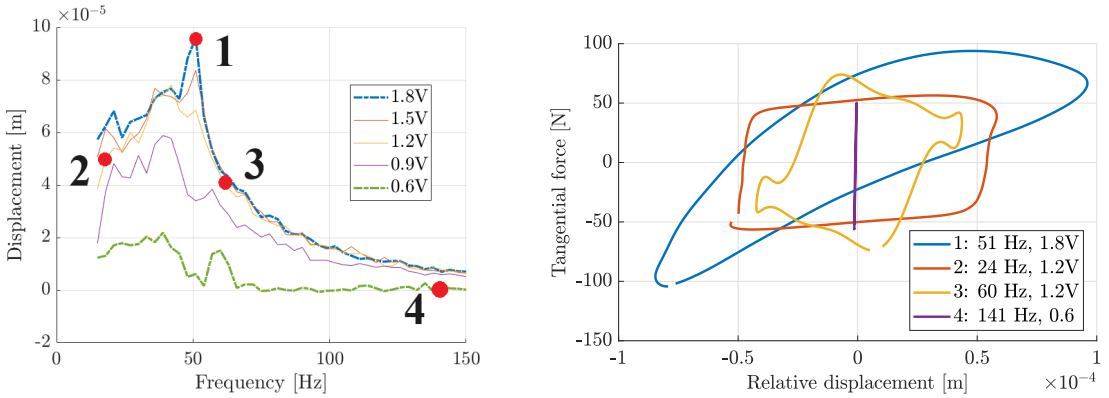

(a) Relative displacement over frequency

(b) Hysteresis at multiple frequencies

Figure 5.2.4: Hysteresis over the entire frequency range

Here it shows that the best result, which aligns the most with literature, is achieved at point two at the beginning of the measurement. After further investigation, it shows that for this particular dataset, so with the smallest contact area and a normal force of 36 N, the optimum displacement is around $6{\cdot}10^{-5}$ m with an accompanying tangential force of roughly 50 N. When the resonance peak at point one is approached, both the tangential force and relative displacement is increased, resulting in a purely macro slip regime. The force rises too fast for the device to register any stick or micro slip, thus resulting in the hysteresis shape shown in blue in Figure 5.2.4b. After the resonance peak, it is clear that the relative displacement diminishes. This is the result of the input force, which changes direction too quickly at higher frequencies to put a large enough displacement profile into the contact. In Figure 5.2.4b this is visualised by the macro slip regime shortening until at 141 Hz only the elastic region is present.

5.2.2 Input force alignment

The essence of the double leaf spring iteration on the design is to constrain the rotation of the mobile stage around all three axes. This is to ensure that only the desired longitudinal motion is present in the system, as explained in section 3.1. This does however also put the constraint on the shaker that its movement needs to be perfectly in line with the translational axis of the mobile stage, otherwise also its input force is acting in a constrained direction. This proved to be exceedingly difficult, especially since the shaker is rigidly attached to the mobile stage by means of a threaded connection. Even slight misalignment of the shaker body resulted in a faulty measurement, where all the generated force was directed to excite the shaker instead of the mobile stage. Initially the entire testing device was designed such that the contact would perfectly be in line with the threaded connection of the shaker, which was mounted on its own base assembly. However, since the double leaf spring assembly allows for near-zero misalignment in all directions except the desired motion, this proved to be insufficient. Several attempts were made to add spacing material between the base of the shaker and the shaker itself, but no perfect alignment was achieved. To be able to perform measurements, some spacing material was added after which the shaker was clamped in place. This setup was then used in all measurements to prevent any variation between measurements. To mitigate this effect during future testing it is advised to use another type of force generator, such as a piezoelectric actuator as used by Li et al. [10]. Here also an uncoupling system is used, which ensures that the

piezoelectric always exerts its force directly in line with the contact plane. Another advantage of adding a piezoelectric actuator instead of a shaker is that the piezoelectric actuator is capable of exerting a larger range of force onto the leaf spring. The shaker currently used has a maximum rated force of 100 N, while piezo actuators are capable of producing much higher forces [25]. Another advantage of using a piezoelectric actuator is the ability to apply a position feedback controller to the system, which would be able to prescribe a displacement of the mobile stage instead of an input force [10]. This approach can be used to ensure that under varying loading conditions still the macro slip regime can be reached, which is not necessarily the case for higher loading conditions in this testing device.

5.2.3 Normal force limitations

Instead of using regular pins or a bolted connection, the testing device uses the two spring plungers to exert a normal force on the contact. This solution was chosen such that the mobile stage can slide underneath the ball point of the spring plunger, and any unwanted movement up and down would be intercepted by the spring behind the ball bearing which ensures the point contact. However, these spring plungers are not designed to apply large loads to a surface and only have a small travel of the spring until a rigid connection is formed. This means that only a maximum force of twice 36 N can be applied to the surface, which in the case of the largest contact area results in a normal pressure of 64 kPa and for the smallest contact area a normal pressure of 192 kPa. This is sufficient for a few load cases and frequencies, as shown in Figure 5.2.4b, but limits the testing device to only small normal loading conditions. If assemblies with larger contact pressures need to be measured, either a spring plunger with a stiffer spring needs to be implemented or a bolted connection can be used. A bolted connection could however lead to bolt dynamics which need to be modelled to produce accurate measurement results.

5.2.4 Contact area alignment

Although great care was taken to design a testing device that has two surfaces perfectly inline, during measurements it became clear that the contact areas can move out of alignment after multiple tests, resulting in fretting behaviour and causing (excessive) wear on the surface. The surfaces are mounted together by pressing them together in alignment, after which the rigid block is securely mounted to the force transducer using a threaded connection. The force transducer itself is then connected to the supporting stud by means of another bolted connection. Due to the movement of the moving stage onto the rigid block, these threaded connections tend to loosen over time, allowing for play between the block, transducer and supporting stud. Even at high torques, over time the rigid block will vibrate loose, resulting in a misalignment of the contact area and resulting in fretting. This fretting is illustrated in Figure 5.2.5.

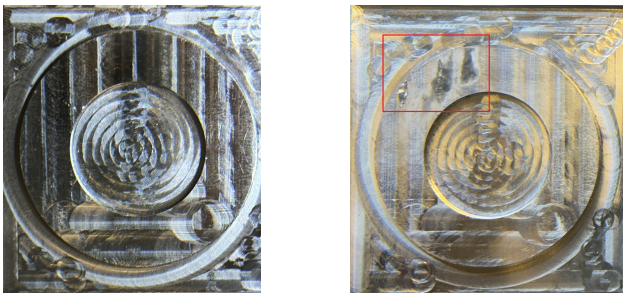

(a) Before testing (b) After testing

Figure 5.2.5: Surface after fretting

This design was chosen to have the least amount of interfaces in the system, which could affect the hysteresis measurement. A possible improvement to prohibit this alignment issue is to further constrain the rigid stage, similar to adding another leaf spring to the mobile stage. When additional constraints are implemented, the rigid stage should not be able to move out of alignment due to vibrations. Care should be taken that in this design no energy is used to deform the constraints, which would limit the force transducer in acquiring an accurate measurement of the tangential force in the contact.

5.2.5 Phase lag

A final remark on the measurement data is the dependence of phase lag between the displacement and the tangential force on the shape of the hysteresis curve. To form a correct hysteresis curve which experiences macro slip, the maximum tangential force should occur during the macro slip regime. If the tangential force and acceleration of the blocks are not synchronised, the hysteresis curve will show significantly different behaviour. This effect is illustrated in Figure 5.2.6, where a phase shift of 90° is added to the displacement by shifting the used displacement data with a quarter of a cycle. As can be seen, the shifted hysteresis curve shows a much clearer defined distinction between the stick, micro slip and macro slip regimes.

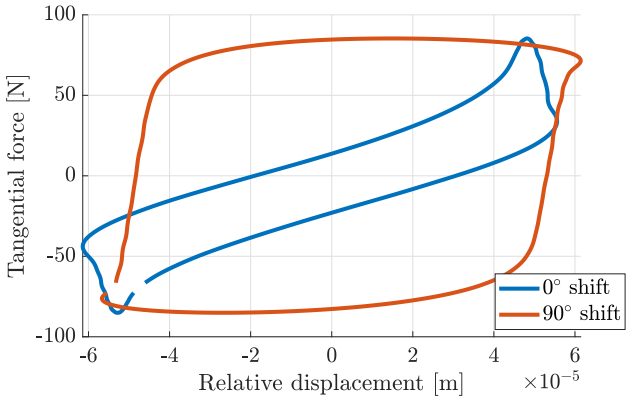

Figure 5.2.6: Effect of 90° phase shift

After further investigation, it became apparent that this phase shift under the right conditions does result in a better hysteresis curve, and especially for lower frequencies a clear change was visible. One possible explanation of this effect, although not further investigated, is the acquisition system used to capture the raw data. A National Instruments 9234 capture card is used to register the data, which captures the data for each input channel in series, meaning that first the first channel is captured, after which the second channel and so on. In this particular case, the acceleration data is captured on the first two channels, while the tangential force is captured with the eighth channel. This serial capturing and the acquisition channels being spaced apart may have resulted in a phase shift between the three signals, although no investigation into this effect has been conducted. To rule out any introduction of lag between the captured signals, it is recommended that a parallel acquisition system is used, which captures all channel signals simultaneously.

5.3 Concluding remarks

As described above, most challenges arise from the use of a shaker with voltage regulation as an excitation force source. As a preliminary recommendation, it is advised to replace the shaker with a position-controlled piezo electric actuator, which is able to prescribe the relative displacement for each measurement. Also, due to the misalignment of the contact surfaces drawing any valid conclusions on the value of the tangential stiffness, dissipated energy and friction coefficient is not possible. Instead, chapter 6 will investigate trends in the contact properties, which are valid even for a contact area that is not properly defined. This will give an insight into the development of the contact properties over frequency and contact pressure, which can be varied without changing the contact interface.

Chapter 6

Detailed analysis

This chapter will further dive into analysing the behaviour of the contact properties over a range of loading conditions and contact parameters. It will first explain which frequency bands can be compared to each other, and how a verifiable comparison between different contact conditions can be made. Afterwards, remarks on the tangential stiffness, dissipated energy and friction coefficient for different loading conditions will be given. It will conclude on what the main takeaways from the measurements are, and where improvements can still be made to improve upon the conclusions that can be drawn from the experimental contact data.

6.1 Region distinction

After carefully calculating the stiffness, dissipated energy and friction coefficient for each hysteresis curve, a trend analysis can be made. As displayed in Figure 5.2.1b, first a high stiffness is experienced by the contact up to 30 Hz, after which a sharp decline in stiffness is present up to 60 Hz. From here on, the stiffness linearly increases again. Another observation is that the stiffness experiences a substantial amount of variance between measurements, which is most likely due to uncertainty while determining the tangential line on the stick regime in the hysteresis curve. This is present for all datasets with different loading and excitation conditions.

As mentioned in section 5.1, certain combinations of loading conditions can either lead to hysteresis curves with a low or large macro slip regime. At low frequencies, the shaker is able to exert a large force over a longer cyclic motion, typically resulting in a hysteresis curve with a large microslip regime. At high frequencies, 60 Hz and upwards, the hysteresis curves showed a decline in displacement between the blocks and therefore a small or non-existent slip between the contacts. To be able to compare different loading conditions and contact areas, it is therefore decided that the measurements need to be divided into regions where the shape of the hysteresis curve is constant. Three regions can be distinguished to be before the resonance frequency, at the resonance frequency and after the resonance frequency which is present at roughly 51 Hz, depending on the normal load. This resonance peak for different normal loads is presented in Figure 6.1.1. When comparing this response to Figure 3.1.3, it can be concluded that the system still behaves as measured during the validation stage. This resonance peak at roughly 51 Hz will be the dividing factor for the three regions, since the increased acceleration of the mobile stage will affect the shape of the hysteresis loop and therefore the measured contact parameters. The region before and after the resonance also have their own characteristic behaviour. This behaviour needs to be identified since further (trend)analysis of these regions is only applicable compared to the same region.

It should be noted that the resonance peak is not present at all loading conditions. For example, at an applied normal force of 18 N only the small surface seems to experience the resonance of the mobile stage. At 36 N, both the smallest and the full surface experience the resonance, while at 72 N almost no resonance peak is present anymore. Since this effect seems to vary for different loading conditions, but especially at higher input forces, it is decided that every measurement is divided into these three regimes, with the resonance peak present at 51 Hz. These three examples are illustrated in Figure 6.1.1

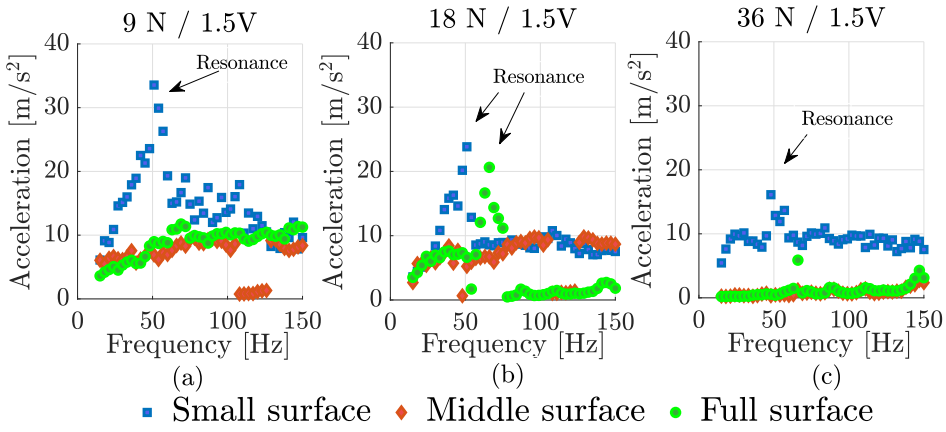

Figure 6.1.1: Resonance peak at different loading conditions

The three sections with their characteristics and hysteresis properties are identified as follows.

Region before resonance

The region before the resonance experiences large deformations since the cyclic force exerted on the leaf spring has a low frequency. This allows for longer periods of acceleration, resulting in a large relevant displacement. The largest force exerted in this region occurs at the lowest driving frequency, i.e. at 15 Hz. Afterward, it linearly decreases with increasing frequency. The tangential force follows a linear trend, which is far less scattered than the other regimes. Figure 6.1.2 displays a typical hysteresis loop found in this region, which shows the large relevant displacement and a clear distinction between stick, micro and macro slip.

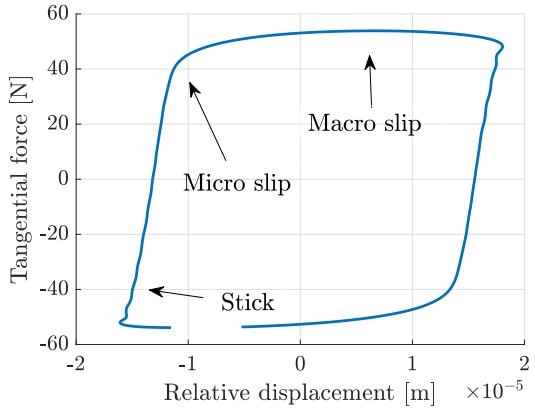

Figure 6.1.2: Standard hysteresis curve before resonance

Note that this behaviour is most notable at higher input voltages, since at high normal forces and low input forces, each contact area is still unable to slip and only stick behaviour is present.

Region around resonance

Around the resonance, so depending on the input force from 45 Hz until 60 Hz, the moving stage experiences a sharp increase in acceleration. This results in a hysteresis curve which is moving too fast through the stick regime that no stiffness can be derived. It is possible to determine the dissipated energy and friction coefficient, but due to the large amount of energy being applied by the shaker at the resonance frequency, it is uncertain if there are no unwanted dynamics affecting the movement of the moving stage. Therefore no conclusive statements can be made in this region, and conclusions based on this experimental data should only be drawn sufficiently before and after the resonance frequency. A standard hysteresis loop within this region is given in Figure 6.1.3. To illustrate the increase in displacement due to the resonance, a typical hysteresis plot from region one has been plotted as well. From Figure 6.1.3 it is also clear that during resonance, no distinct stick, micro and macro slip regions are identifiable.

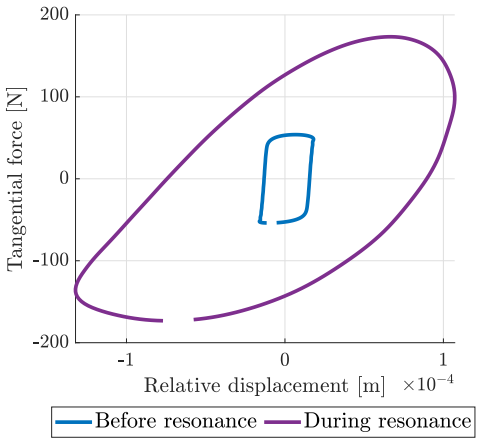

Figure 6.1.3: Typical hysteresis curves before and during resonance

Region after resonance

A typical hysteresis curve at this region is given in Figure 6.1.4. Here also a fitted tangent, or stiffness, line is plotted to illustrate how the stiffness is extracted at these frequencies.

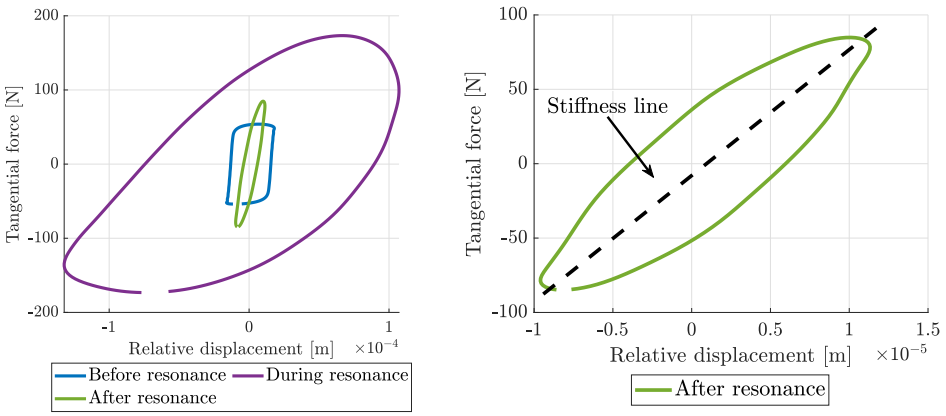

(a) All types of hysteresis curves

(b) Hysteresis curve after resonance

Figure 6.1.4: Standard hysteresis after resonance

After the resonance, the contact properties hardly change with frequency. It is also clear that the shaker is not able to push enough energy into the contact, which results in little to no micro and macro slip during measurements. Especially at higher frequencies, where the shaker is switching direction rapidly, the limited time between reversal of the force results in a very small displacement of the moving stage. This region is therefore dominated by the elastic regime of the hysteresis curve, and predominantly elastic tangential stiffness can be extracted.

Now that the three regions are defined, several points in these regions can be used to compare multiple measurements with varying contact conditions. In the next sections, trends in the development of the stiffness, dissipated energy and friction coefficient will be determined for changing the driving frequency, input force and normal force. Both individual points in each region will be compared to understand how the hysteresis curve changes, as well as the average values of each measurement per region to understand the global changes in contact properties when varying the contact (loading) conditions.

6.2 Stiffness analysis

To determine on which loading conditions the contact stiffness is dependent, the stiffness is determined for all available datasets with different variables. Each hysteresis curve is also given a rating on reliability, where a hysteresis curve with clearly distinct regimes is given a positive score, and a hysteresis curve with no distinction between stick, micro and macro slip is given a negative score. This reliability score for each set of loading conditions can be found in Appendix C. For the regions before, during and after the resonance a single frequency is chosen which has the best-defined hysteresis loops, such that a more decisive conclusion can be drawn when comparing the contact stiffness between datasets. For both excitation forces at 1.2 V and 1.8 V the development of the contact stiffness is given in Figure 6.2.1. To more clearly visualise the development of the contact stiffness, the average value at each loading condition has been calculated and a surface plot has been added.

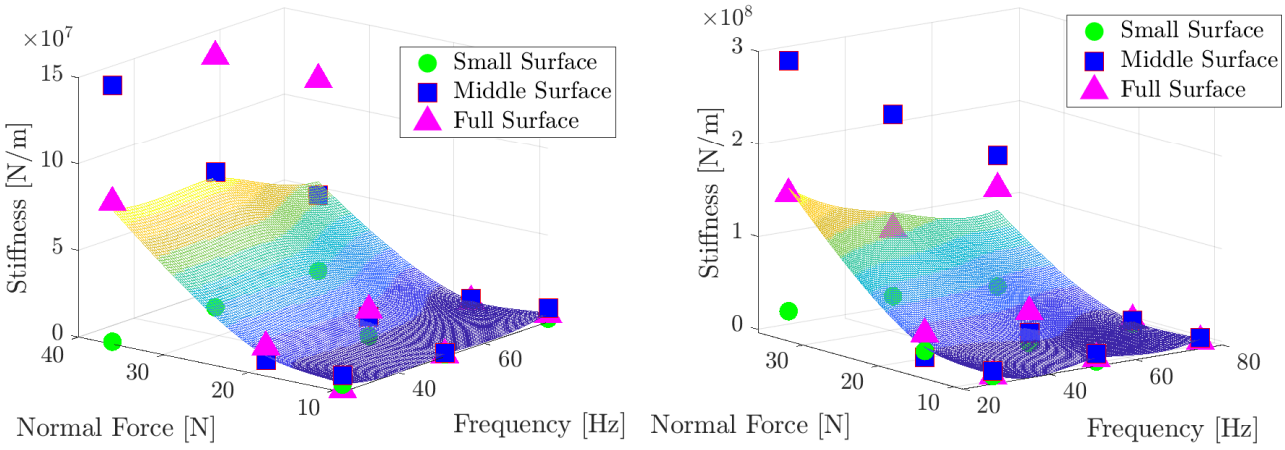

(a) Stiffness at 1.2V excitation

(b) Stiffness at 1.8V excitation

Figure 6.2.1: Stiffness for various loading conditions

Looking at both figures, an increase in stiffness is seen when increasing the normal force onto the surface. This is in line with expectations, where a higher contact pressure results in a larger stiffness between two surfaces. Due to the asperities of both surfaces coming more into contact due to larger normal loads, the adhesion between the two surfaces increases and the tangential contact stiffness also rises. This result confirms the theory that stiffness increases with normal load, and for industrial applications the contact stiffness needs to be modelled as a function of the normal load.

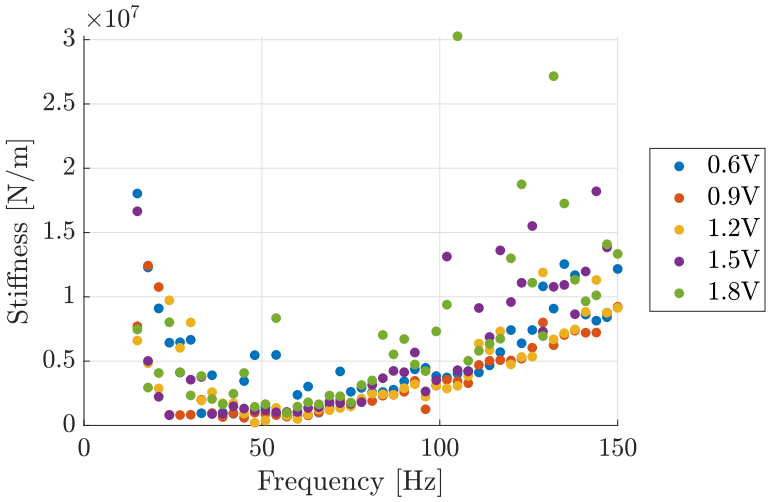

Figure 6.2.2: Stiffness development for one dataset

In Figure 5.2.1b, displayed in Figure 6.2.2 again for clarity, it can be observed that during the resonance in acceleration the stiffness drops, after which for higher frequencies the stiffness seems to linearly increase again. An explanation for this behaviour could be the plastic hardening of the asperities over time, reducing their elasticity, increasing the contact stiffness. Also Peng et al. [26] discovered a linear tangential stiffness increase when increasing the excitation frequency, for both a solid-to-solid and lubricated interface, similar to the higher frequency trend observed in Figure 6.2.2. This increase in contact stiffness with increasing frequency was also described by Bowden and Tabor [27], who stated that when a load is applied to a contact, either normal or tangential, the 'real' area in contact between the two surfaces has to increase to accommodate the applied load. This leads to the conclusion that if a large tangential load is applied, the number of asperities in contact should increase, therefore increasing the contact stiffness.

However, when looking at Figure 6.2.1, a slight decrease in stiffness with increasing frequency is observed for the highest normal load condition and all contact surfaces. This trend is opposite of the theory described before, and is not in line with expectations. This could merely be due to experimental uncertainty, but it is also theorised that the acceleration and velocity could be too high that not enough time is available for this increase in asperity contact described by Bowden and Taylor [27], thus resulting in a decrease in contact stiffness. This effect was studied by Penissi [9], who showed that the contact stiffness can decrease with an increase in sliding velocity. This effect is also visible in Figure 6.2.2, where at the resonance frequency the stiffness drops a significant amount, most likely due to the high velocity and acceleration compared to the region before and after the resonance frequency. To verify if the increase in velocity is truly the cause of the drop in stiffness, prolonged tests where the surfaces have been given a sufficient amount of time to run in should be conducted. Once this has been achieved, measurements with excitation at increasing velocity should be executed, to isolate the effect that velocity has on stiffness.

Penissi [9] also theorised that the contact stiffness increases during the running in period of the joint, since during this period a larger amount of asperities come into contact. After the running-in period, the asperities on the two surfaces have worn down and a smoother contact surface is present, which results in a lower contact stiffness. To determine if this effect is also present in the experimental data, subsequent testing with identical contact surfaces needs to be conducted, in which each specimen is subjected to the same running in period.

An additional observation from the experimental results is the stiffness dependency on nominal contact area. For all normal loads the stiffness appears to hardly change when the frequency in increased, and also between surfaces no clear difference is present. That the stiffness does not change with diminishing contact area is most likely due to the misalignment of the interfaces, as described in section 5.2. Since this misalignment has resulted in three almost identical surfaces, also the contact stiffness shows no apparent change between the three surfaces. To be able to draw conclusions on the effect of diminishing contact area, and answer the main research goal of this study, the test device should be iterated such that the contact area remains in full contact during the measurements.

A final comment on the contact stiffness is the presence of adhesion between the two contacting surfaces. Bazrafshan et al. [28] discussed that the friction hysteresis is greatly influenced by the surface roughness and adhesion of the two surfaces, and especially two similar materials with a high surface energy experience high adhesion. Since aluminium has a relatively high surface energy and two blocks of the same material are used in these measurements, the adhesion forces are high. In order to mitigate this effect, more tests need to be conducted with a range of materials. Different combinations of material in contact should be tested, to ensure that the true contact stiffness is measured.

Up to this point, the measured contact stiffness was assumed to be originating from the contact interface. However, even though the testing device directly measures the tangential force and the displacement of both stages, the interface stiffness is due to both the bulk stiffness of the material as well as the contact stiffness due to the two interacting surfaces. The bulk stiffness is defined as the stiffness experienced in a contact when the two opposing bodies are fused together, so no interface is present. This effect is also described by Mulvihill et al. [29], where the measured stiffness is a summation of both the bulk stiffness as the isolated interface stiffness, or

$$\frac{1}{k_{measured}} = \frac{1}{k_{bulk}} + \frac{1}{k_{interface}}. \tag{6.1}$$

To further improve the understanding of the change in isolated contact interface stiffness, a Finite Element model should be constructed, similar to models created by Li et al. [10] and Mulvihill et al. [29]. This model should determine the bulk stiffness for each type of loading condition, since this may vary depending on what normal load and excitation frequency is applied. Combined with the experimental data, the actual isolated interface stiffness can be determined.

6.3 Dissipated energy

As explained in previous sections, the dissipated energy is a measure of the damping between the contact areas. In Figure 6.3.1 the dissipated energy is plotted for the three contact surfaces, with varying normal load and excitation frequency, and the average value is plotted as a surface to indicate the trend between measurements.

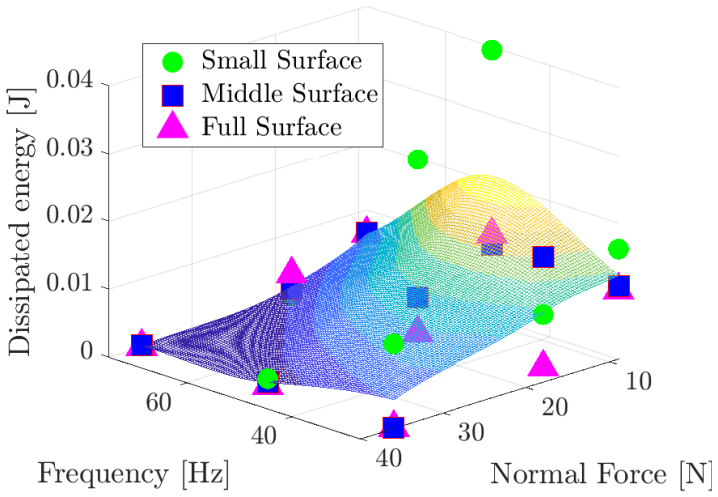

Figure 6.3.1: Master curve for dissipated energy

From Figure 6.3.1 it becomes clear that at lower normal loads the surfaces experience greater energy losses. Especially the smallest contact area, peaking at a conctact energy loss of 0.04 J. It is in line with expectations that the dissipated energy lowers with increasing normal load conditions. Since more force is exerted onto the surface, a larger tangential force is needed to make the contact area experience macro slip. This results in a lower relative displacement when applying the same excitation force with a higher normal load, thus less energy is dissipated from the contact.

In Figure 6.3.1, the highest dissipated energy occurs at the lowest normal load setting and at the resonance frequency. Since the resonance is still able to increase the accelerance of the moving stage, a large relative displacement occurs at these levels, inherently resulting in a high dissipated energy. The lowest energy loss occurs coherently with expectations, at the highest normal load level and in the third region. The high loading conditions cause a very small amount of relative displacement between the blocks, while the high excitation frequency of the driving force also causes small accelerations. These two factors result in almost zero energy dissipation for all three contact areas.

Unfortunately, as was also mentioned in the discussion of the stiffness trend, no clear distinction between contact areas can be found. From Figure 6.3.1 it could be concluded that the smallest and middle surface overall experience a larger loss in energy than the full surface, but due to the scatter of the data no definitive conclusion can be drawn upon this observation. Techniques to further improve the accuracy of the data, such that a conclusion on the effect that contact area has on dissipated energy within a contact will be given in section 7.3.

6.4 Friction coefficient

As expressed in Figure 5.1.1, the friction coefficient between the two surfaces in contact can be determined by finding the tangential force during the macro slip region, and dividing this value by the applied normal force, or in equation form as

$$\mu_f = \frac{F_t}{2F_n}$$

where F_n is here defined as the force applied by one force plunger. Figure 6.4.1 shows the determined friction coefficient for the three distinct regions for several loading and excitation settings, and the overall average trend as a surface plot.

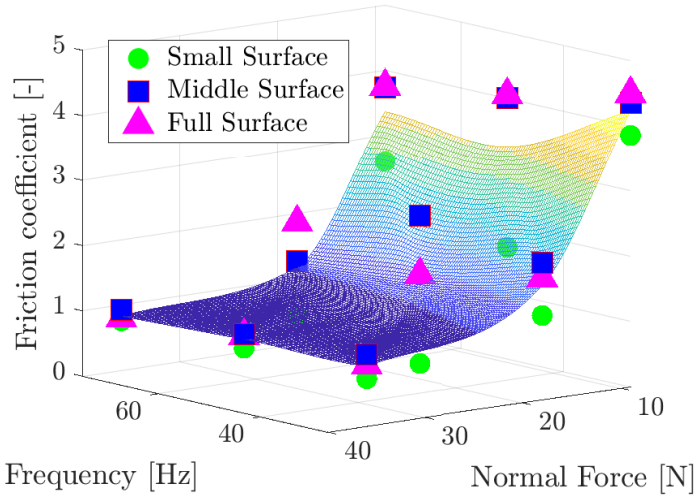

Figure 6.4.1: Master curve for friction coefficient

For all three contacts at a constant normal load, a fairly constant friction coefficient is observed when the excitation frequency is increased. This is in line with expectations, since in this testing device the shaker diminishes in excitation force with an increase in frequency, therefore also decreasing the tangential force in the contact. Since the normal force remains constant throughout the entire frequency range, the friction coefficient remains relatively constant when only increasing the excitation frequency. This observation is expected since the friction coefficient should in theory not change with an increase in sliding velocity, only when the surface topology within the contact changes. Since the friction coefficient is directly related to the topology of the two surfaces in contact, a change in normal force should show a change in friction coefficient due to the (plastic) deformation of the asperities. Due to this deformation of the asperities on both surfaces, a different real contact area forms, which could lead to either a decrease or increase in the friction coefficient. This could explain the trend seen in Figure 6.4.1, where the friction coefficient diminishes with increasing normal load. However, Li et al. [10] observed a rise in friction coefficient with increasing normal load in a bolted connection. This contradicts the findings in this research, which is most likely due to badly defined contact between the two surfaces. A deeper investigation into the deformation of the contact interface and the real contact area needs to be conducted in order to determine what effect the change in topology has on the friction coefficient, as well as on the other contact properties such as stiffness and damping.

Comparing the found values to literature, Bajpai et al. [30] showed a dry friction coefficient between two aluminium surfaces of 1.10 to 1.35. This is in line with the friction coefficient measured at a normal force of 72 N for all three surfaces and regions. To determine if the friction coefficient further diminishes at higher contact pressure, more measurements at higher normal loads need to be conducted.

6.5 Validity of results

From the previous sections some conclusions regarding the dependency of contact stiffness, dissipated energy and friction coefficient as a function of normal force, excitation force and possibly contact area can be drawn. However, due to the misalignment of the contact blocks and the filtering of the tangential force due to the stiffness of the rigid stage, some comments on the validity of these results need to be made. Despite the efforts to create a contact interface that remains in full contact during measurements, and all steps taken to validate the testing device for this purpose, some inherent stiffness problems remain. Due to the rigid stage not being stiff enough, the measured tangential force needs to be post-processed to such a degree that some of the data is lost in the process. This results in the ability to draw hysteresis loops from which conclusions can be drawn, but not the full effect of changing interface conditions can be measured. It is therefore strongly advised to update the design of the testing device, such that the stiffness of the rigid mass is greatly increased, and a new alignment mechanism is in place for the rigid stage, similar to the double leaf springs of the moving stage. This will increase the accuracy of the measurements and therefore creates stronger arguments on how the contact conditions change.

Chapter 7

Conclusion and recommendations

7.1 Research questions

This final chapter will conclude this research by answering the research question stated in the introduction, here presented again for convenience:

How can a contact surface be designed, such that the tangential stiffness, dissipated energy and friction coefficient can be predicted accurately to improve existing contact models?

To answer the research question, this thesis will answer the following sub-questions:

1: How can a testing setup be designed, which reliably produces a dominant single degree of freedom motion, and is able to accurately measure a sliding contact?

2: How can a framework be designed, which is able to extract the relevant contact parameters from experimentally gathered contact interface data?

3: How are the joint contact parameters affected by the loading conditions, based on data gathered from the constructed testing device and experimental framework?

7.2 Conclusion

This research presents a newly designed testing device to study hysteresis for comparatively large, designed contact surfaces. Compared to other hysteresis testing devices in literature, this testing rig distinguishes itself by pursuing large contact area testing and evaluating the contact properties for contact surfaces used in industry. By using precision mechanics principles a dominant single degree of freedom motion across the contact is realised, on which accurate displacement measurements are realised by using accelerometers. To ensure that the measurements accurately capture the joint dynamics, validation and identification steps are performed on the assembled test device to determine the suitable contact conditions, which resulted in a frequency operating range of 15-200 Hz, while applying a maximum contact pressure of 172 KPa to the contact surface. To extract the relevant contact properties from the experimental data, a framework has been developed that automatically cycles through loading conditions and filters the experimental data to create the hysteresis curves. Using this framework, the contact stiffness, dissipated energy and friction coefficient can be extracted for each individual loading condition applied by the testing device.

Based on the experimental data, the effect of contact pressure, tangential force and excitation frequency on the contact properties has been studied, to determine how the contact parameters are affected by a variety of loading conditions. To this end, three distinct regions for the three different designed contact areas are investigated. The results gathered are in line with literature and showed promising results for future testing. A comparison of these regions between different sets of contact conditions is performed, which shows trend lines for the tangential stiffness, dissipated energy and friction coefficient which correspond with the observed joint dynamics and are in line with results found in literature. Based on these trend results, a prediction can be made on what effect loading conditions have on the contact stiffness, friction coefficient and dissipated energy. However, due to a small misalignment of the contacting surfaces, no definitive answer can be given as to how the geometry of a contact surface can be designed to accurately predict the contact properties. Based on the experimental results, it is possible to predict the dynamic contact behaviour of a line contact, and how the loading conditions influence the contact properties. To achieve an understanding on how a large, designed contact geometry influences the contact properties, the alignment of the two contacting surfaces should be improved in the testing device.

7.3 Recommendations

To improve the usability of the testing device and the accuracy of the extracted contact properties, several recommendations are made for future research.

7.3.1 Increasing setup stiffness

One of the major challenges in creating reliable hysteresis curves was the filtering technique subjected to the measured tangential stiffness. Although the device was carefully designed to retain a high stiffness for the tangential force sensor, this showed to be insufficient in practice. The reinforced structure still introduced unwanted dynamics, primarily due to the thin-walled tube that was used. This resulted in the appearance of highly non-linear effects on the tangential data, rendering the correct visualisation of the hysteresis curves impossible. Therefore, several filtering techniques were applied to the measured force. However, to achieve a more reliable and direct hysteresis curve of the joint dynamics, it is strongly advised that a design iteration is made to the device which increases the support stiffness of the tangential force sensor. This can be achieved by stiffening the structure which supports the tangential force sensor by adding more material, or a closed body approach can be investigated, similar to Li et al. [10].

7.3.2 Application of excitation force

During the first measurements, it became apparent that the shaker used to excite the system is unable to apply enough force onto the joint to force the contact into the macro slip regime, especially at higher frequencies. It is therefore advised that another excitation source is used, either a shaker with a higher force rating or a piezoelectric with closed-loop position feedback control. Additionally, an alignment apparatus and decoupling mechanism needs to be in place which only allows for forces tangential to the contact surface, as proposed by [10]. Due to the double leaf spring design, any forces not in line with the contact plane result in a stiffening effect of the system, resulting in low displacements of the contact surface.

7.3.3 Contact surface alignment

After a close investigation of the contact surfaces after testing, it showed that fretting had occurred due to misalignment of the contact. This fretting resulted in excessive wear of the contact, which changed the contact properties of the surfaces significantly. This misalignment is mainly due to the rigid stage vibrating loose from the force transducer, and results in a line or point contact instead of the desired flat on flat contact. This also makes any distinction between designed contact surfaces unreliable. For the application of this testing device, it is therefore strongly advised that future research focuses on constructing an alignment section for the rigid stage, so no dislocation of the contact surface can occur.

7.3.4 Increasing contact pressure

The current application of normal force onto the contact surface is performed by two force plungers. However, individually these have a maximum force application of 36 N when fully indented. This means that a maximum normal force of 72 N can be exerted onto the contact, resulting in a maximum contact pressure of 172 KPa for the smallest contact surface. Other research commonly reaches much higher normal forces [10, 8], resulting in contact pressures up to 350 MPa. It is therefore recommended that future investigations for larger measurement ranges also include another application of the normal force, which can further increase the contact pressure. In literature, higher contact pressures are typically achieved by using hydraulic actuators, capable of producing higher forces than achieved in this research. It is advised to design a decoupling mechanism, such that the stiffness of these actuators is not translated onto the contact.

7.3.5 Displacement measurements

Currently, the testing device uses accelerometers on both surfaces close to the contact to measure the displacement of each block. However, due to the limited accuracy of the accelerometers, an area of improvement is the implementation of a separate LDV measurement system. It is advised that the same approach as performed by Li et al. [10] is implemented to directly measure the relative displacement between the two surfaces. To this end, the line of sight for the laser has already been implemented in the design of the testing device, such that setting up this technique should be relatively straightforward. As also discussed by Li et al. [10], this technique is more reliable than the usage of accelerometers or two separate LDVs, while still obtaining the relative motion of the jointed bodies instead of only the motion of the moving body.

7.3.6 Repeatability and time dependency

To determine the repeatability of the performed experiments, it is recommended to test specimens with the same surface conditions subjected to identical loading conditions, to verify that the experimental setup produces repeatable results. This could not be verified during this study, due to time and material limitations to produce additional specimens. For future research, it is also recommended to perform prolonged testing on one contact surface at set loading conditions, such that the effect of continuous cyclic load can be determined. These tests would also be able to determine how the surface topology changes after a set amount of loading cycles, and relate asperity deformation and wear profiles to a variation in contact properties.

Bibliography

[1] A. Fantetti, C. Pennisi, D. Botto, S. Zucca, and C. Schwingshackl, "Comparison of contact parameters measured with two different friction rigs for nonlinear dynamic analysis," in *International Conference on Noise and Vibration Engineering*, Leuven, Belgium, Jul. 2020, pp. 2165-2174. [Online]. Available: https://www.researchgate.net/publication/343111953_Comparison_of_contact_parameters_measured_with_two_different_friction_rigs_for_nonlinear_dynamic_analysis

[2] D. J. Ewins, "A survey of contact hysteresis measurement techniques," in *The Mechanics of Jointed Structures*, M. R. W. Brake, Editor, New York, NY, USA: Springer, 2018, ch. 12, pp. 149-179, [Online]. Available: https://link.springer.com/chapter/10.1007/978-3-319-56818-8_12

[3] D. J. Ewins, "Exciting vibrations: the role of testing in an era of supercomputers and uncertainties," *Meccanica,* vol. 51, no. 12, pp. 3241-3258, Nov. 2016, doi: 10.1007/s11012-016-0576-y

[4] T. J. A. De Vries, J. Holterman, and M. P. Loster, "Smart disc - application in an ASML water stepper," in *Proceedings Philips Conference on Applications of Control Technology PACT'01,* Eindhoven, The Netherlands, Feb. 2001, pp. 1-10. [Online]. Available: https://research.utwente.nl/en/publications/smart-disc-application-in-an-asml-wafer-stepper

[5] R. L. Spangler, F. M. Russo, and D. A. Palombo. "Compact integrated piezoelectric vibration control package," in *Smart Structures and Materials 1997: Smart Structures and Integrated Systems*, San Diego, CA, USA, Mar. 1997, pp. 728-740, doi: 10.1117/12.275697

[6] M. A. Beijen, M. F. Heertjes, H. Butler, and M. Steinbuch. "Disturbance feedforward control for active vibration isolation systems with internal isolator dynamics," *Journal of Sound and Vibration,* vol. 436, pp. 220-235, Dec. 2018, doi: 10.1016/J.JSV.2018.09.010

[7] M. Scheel, T. Schulz, and M. Krack. "Potential and limitation of a nonlinear modal testing method for friction-damped systems," in *Nonlinear Structure and Systems, Volume 1: Proceedings of the 37th IMAC, A Conference and Exposition on Structural Dynamics 2019*, G. Kerschen, M. R. W. Brake, and L. Renson, Editors, Cham, Switzerland: Springer, 2020, ch. 11, pp. 95-97, doi: 10.1007/978-3-030-12391-8_11

[8] C. W. Schwingshackl, E. P. Petrov, and D.J. Ewins, "Measured and estimated friction interface parameters in a nonlinear dynamic analysis," *Mechanical Systems and Signal Processing*, vol 28, pp. 574-584, Apr. 2012, doi: 10.1016/j.ymssp.2011.10.005

[9] C. Pennisi, "Experimental measurements to extract friction contact parameters for aero-engine applications," M.S. thesis, Dept. Mechanical Engineering, Politecnico di Torino, Torino, Italy, 2019. [Online]. Available: https://webthesis.biblio.polito.it/13360/1/tesi.pdf

[10] D. W. Li, C. Xu, D. Botto, Z. S. Zhang, and M. Gola, "A fretting test apparatus for measuring friction hysteresis of bolted joints," *Tribology International,* vol. 151, pp. 1-10, Nov. 2020, doi: 10.1016/j.triboint.2020.106431

[11] D. L. Peña, C. Ibáñez, V. Albero, A. Espinós, A. Hospitaler, and M. L. Romero, "Influence of spalling on the biaxial bending resistance of reinforced concrete columns exposed to fire," in *11th International Conference on Structures in Fire (SiF2020),* Brisbane, Australia, Nov.-Dec. 2020, pp. 204-211, doi: 10.14264/384eb39

[12] M. Pastor, M. Binda, and T. Harčarik, "Modal Assurance Criterion", *Procedia Engineering,* vol.48, pp. 543-548, Dec. 2012, doi: 10.1016/j.proeng.2012.09.551

[13] F. Tubita, A. Fantetti, L. Blanc, and F. Thouverez, " Effect of fretting-wear on dynamic analysis. Comparison between experimental results and numerical simulations for a vibratory friction rig.", in *IX International Conference on Computational Methods for Coupled Problems in Science and Engineering,* E. Oñate, M. Papadrakakis and B. Schrefler, Eds., Chia, Italy, June 2021, pp. 1-12, doi: 10.23967/coupled.2021.020

[14] S. Filippi, A. Akay, and Muzio M. Gola, "Measurement of tangential contact hysteresis during microslip," *J. Tribol,* vol. 126, no. 3, pp. 482–489, Jun. 2004, doi: 10.1115/1.1692030

[15] J. B. Hopkins and M. L. Culpepper, "Synthesis of multi-degree of freedom, parallel flexure system concepts via freedom and constraint topology (FACT) - part I: principles," *Precision Engineering*, vol. 34, no. 2, pp. 259-270, Apr. 2010, doi: 10.1016/j.precisioneng.2009.06.008

[16] J. B. Hopkins and M. L. Culpepper, "Synthesis of multi-degree of freedom, parallel flexure system concepts via freedom and constraint topology (FACT) - part II: practice," *Precision Engineering*, vol. 34, no. 2, pp. 259-270, Apr. 2010, doi: 10.1016/j.precisioneng.2009.06.007

[17] M. E. Kartal, D. M. Mulvihill, and D. Nowell, "Determination of the frictional properties of titanium and nickel alloys using the digital image correlation method," *Experimental Mechanics,* vol. 51, pp. 359–371, Mar 2011, doi: 10.1007/s11340-010-9366-y

[18] Y. Liu, "Choose the best element size to yield accurate FEA results while reduce FE model's complexity", *British Journal of Engineering and Technology,* vol. 1, no. 7, pp. 13-28, May 2013, issn: 2326 – 425X

[19] H. Wittel, D. Muhs, D. Jannasch and J. Voβiek, "Schroefverbindingen," in *Roloff/Matek: Machineonderdelen, 5th edition.* Den Haag: Sdu Uitgevers bv, 2011, 96.

[20] Z. B. Xu, J. F. Peng, J. H. Liu, X. Y. Liu, W. L. Zhang, and M. H. Zhu, "Study on tribo-chemical and fatigue behavior of 316L austenitic stainless steel in torsional fretting fatigue," *Proceedings of the Institution of Mechanical Engineers, Part J: Journal of Engineering Tribology*, vol. 234, no. 1, pp. 84-93, Jan. 2020, doi: 10.1177/1350650119864482

[21] H.A. Sherif and S.S. Kossa, "Relationship between normal and tangential contact stiffness of nominally flat surfaces", *Wear*, vol. 151, no. 1, pp. 49-62, Nov. 1991, doi: 10.1016/0043-1648(91)90345-U

[22] M. L. Raffa, F. Lebon, and G. Vairo, "Normal and tangential stiffnesses of rough surfaces in contact via an imperfect interface model", *International Journal of Solids and Structures,* vol. 87, no. 1, pp. 245-253, Jun. 2016, doi: 10.1016/j.ijsolstr.2016.01.025

[23] N. Yoshioka and C.H. Scholz, "Elastic properties of contacting surfaces under normal and shear loads: 1. Theory", *Journal of Geophysical Research: Solid Earth,* vol. 94, no. B12, pp. 17681-17690, Dec. 1989, doi: 10.1029/JB094iB12p17681

[24] A. Baltazar, S. I. Rokhlin, and C. Pecorari, "On the relationship between ultrasonic and micromechanical properties of contacting rough surfaces", *Journal of the Mechanics and Physics of Solids*, vol. 50, no. 7, pp. 1397-1416, Jul. 2002, doi: 10.1016/S0022-5096(01)00119-3

[25] S. E. Prasad, D. F. Waechter, R. G. Blagow, H. W. King, and Y. Yaman, "Application of piezoelectrics to smart structures," in *Il Eccomas Thematic Conference on Smart Structures and Materials,* Lisbon, Portugal, Jul. 2005, pp. 1-16/ [Online]. Available: https://sensortechcanada.com/wp-content/uploads/2021/08/2005-01-Application-of-Piezoelectrics-to-Smart-Structures.pdf

[26] L. X. Peng, Z. Q. Gao, Z. Y. Ban, F. Gao, and W. P. Fu, "Dynamic Tangential Contact Stiffness and Damping Model of the Solid-Liquid Interface," Machines, vol. 10, no. 8, pp. 804-830, Sep. 2022, doi: 10.3390/machines10090804

[27] F. P. Bowden and D. Tabor, "The friction and Lubrication of Solids." Oxford University Press, Clarendon Press, pp. 5-17, 1986.

[28] M. Bazrafshan, M. B. de Rooij, and D. J. Schipper, "The effect of adhesion and roughness on friction hysteresis loops," International Journal of Mechanical Sciences, vol. 155, pp. 9-18, May 2019, doi: 10.1016/j.ijmecsci.2019.02.027

[29] D. M. Mulvihill, H. Brunskill, M. E. Kartal, R. S. Dwyer-Joyce, and D. Nowell, "A comparison of contact stiffness measurements obtained by the digital image correlation and ultrasound techniques," Experimental Mechanics, vol. 53, pp. 1245–1263, Feb. 2013, doi: 10.1007/S11340-013-9718-5

[30] A. Bajpai, P. Saxena, and K. Kunze. "Tribo-mechanical characterization of carbon fiber-reinforced cyanate ester resins modified with fillers," Polymers, vol. 12, no. 8, pp. 1-13, Jul. 2020, doi: 10.3390/polym12081725

[31] *Ansys Help Viewer*. (Ver. 2022 R2), ANSYS, Inc.

Appendices

Appendix A

Mathematics behind a FRF

To construct the FRF of a system, either an analytical approach or an experimental approach can be used. The experimental approach, where the acceleration is measured against excitation force is predominately used in this thesis, however this section will explain the mathematics behind an FRF.

The simplest representation of a structure is defined as a Single Degree of Freedom (SDOF) mass-spring-damper system, depicted in Figure A.0.1.

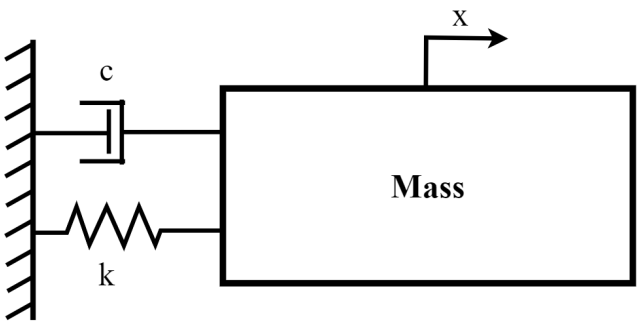

Figure A.0.1: Mass spring damper system

Harmonic excitation

This system is excited by a harmonic force, which in this example will be acting onto mass of the system. The amplitude and phase of the receptance the of this system are derived as follows. First start with the equation of motion of the system which is excited by a harmonic force input,

$$\sum F = m\ddot{x} \tag{A.1a}$$

$$m\ddot{x}(t) + c\dot{x}(t) + kx(t) = Fe^{i\omega t} \tag{A.1b}$$

$$\ddot{x} + \frac{c}{m}\dot{x} + \frac{k}{m}x = \frac{F}{m}e^{i\omega t} \tag{A.1c}$$

if we use the standard definitions

$$\zeta = \frac{c}{2m\omega_n} \quad \text{and} \quad \omega_n = \sqrt{\frac{k}{m}} \tag{A.2}$$

gives the expression

$$\ddot{x} + 2\zeta\omega_n\dot{x} + \omega_n^2 = \omega_n^2\frac{F}{k}e^{i\omega t} \tag{A.3}$$

Using the general solution for a harmonic excitation and the first and second derivative of this function,

$$x(t) = Xe^{i\omega t} \tag{A.4a}$$

$$\dot{x}(t) = i\omega Xe^{i\omega t} \tag{A.4b}$$

$$\ddot{x}(t) = -\omega^2 Xe^{i\omega t} \tag{A.4c}$$

and combining these expressions with Equation A.3 gives rise to the expression

$$\left(-\omega^2 + 2\zeta\omega_n\omega i + \omega_n^2\right) Xe^{i\omega t} = \frac{\omega_n^2}{k} Fe^{i\omega t}. \tag{A.5}$$

If both sides are divided by $e^{i\omega t}$, the final equation is referred to as the receptance, i.e. the position response of a system to a force,

$$H(\omega) = \frac{X(\omega)}{F(\omega)} = \left[\frac{1}{k}\right]\left[\frac{\omega_n^2}{\omega_n^2 - \omega^2 + 2\zeta\omega\omega_n i}\right] \tag{A.6}$$

The corresponding magnitude and phase needed to construct the FRF are then defined as

$$|H(\omega)| = \left|\frac{X(\omega)}{F(\omega)}\right| = \left[\frac{1}{k}\right]\left[\frac{\omega_n^2}{\sqrt{\left(\omega_n^2 - \omega^2\right)^2 + \left(2\zeta\omega\omega_n\right)^2}}\right] \tag{A.7a}$$

$$|H(\omega)| = \left[\frac{1}{m}\right]\left[\frac{1}{\sqrt{\left(\omega_n^2 - \omega^2\right)^2 + \left(2\zeta\omega\omega_n\right)^2}}\right] \tag{A.7b}$$

and

$$\phi(\omega) = \arctan\left(\frac{2\zeta\omega\omega_n}{\omega_n^2 - \omega^2}\right). \tag{A.8}$$

Harmonic base excitation

Another possible scenario is that the base to which the spring and damper are attached is moving, a base excitation. This scenario is illustrated in Figure A.0.2.

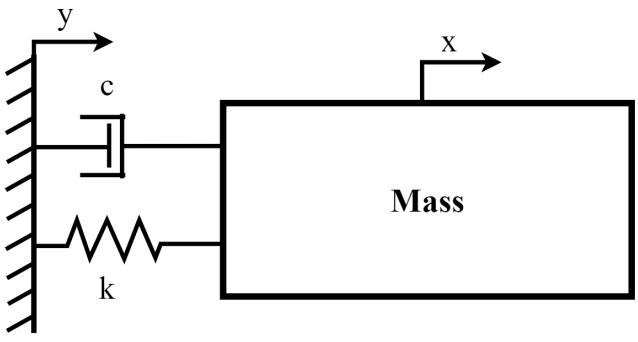

Figure A.0.2: Mass spring damper system with base excitation

The equation of motion, with the standard definitions given in Equation A.2, is described as

$$\ddot{x}(t) + 2\zeta\omega_n\dot{x}(t) + \omega_n^2 x(t) = 2\zeta\omega_n\dot{y}(t) + \omega_n^2 y(t) \tag{A.9}$$

where $x(t)$ describes the movement of the mass and $y(t)$ describes the movement of the base. Using the same definition for a harmonic response as given in Equation A.4 and performing the same operation for the base movement,

$$y(t) = Ye^{i\omega t} \tag{A.10a}$$

$$\dot{y}(t) = i\omega Ye^{i\omega t} \tag{A.10b}$$

$$\ddot{y}(t) = -\omega^2 Ye^{i\omega t}. \tag{A.10c}$$

Substituting Equation A.10 into the equation of motion gives

$$\left[\omega_n^2 - \omega^2 + 2\zeta\omega_n\omega i\right] Xe^{i\omega t} = \left[\omega_n^2 + 2\zeta\omega_n\omega i\right] Ye^{i\omega t} \tag{A.11}$$

Removing the harmonic term again gives rise to the receptance as

$$H(\omega) = \frac{X(\omega)}{Y(\omega)} = \frac{\omega_n^2 + 2\zeta\omega_n\omega i}{\omega_n^2 - \omega^2 + 2\zeta\omega_n\omega i}. \tag{A.12}$$

This can be simplified further as defining Ω_d to be the ratio between excitation and natural frequency,

$$\Omega_d = \frac{\omega}{\omega_n} \tag{A.13}$$

resulting in

$$H(\omega) = \frac{X(\omega)}{Y(\omega)} = \frac{1 + 2\zeta\Omega_d i}{1 - \Omega_d^2 + 2\zeta\Omega_d i}, \tag{A.14}$$

with the magnitude written as

$$|H(\omega)| = \frac{|X(\omega)|}{|Y(\omega)|} = \sqrt{\frac{1 + (2\zeta\Omega_d)^2}{\left(1 - \Omega_d^2\right)^2 + (2\zeta\Omega_d)^2}} \tag{A.15}$$

and the phase as

$$\phi(\omega) = \arctan\left(\frac{2\zeta\Omega_d^3}{1 - \Omega_d^2 + (2\zeta\Omega_d)^2}\right). \tag{A.16}$$

Appendix B

Roughness measurements

To determine the change in surface roughness before and after testing, a confocal roughness test has been performed on the contacting blocks before and after testing. The milled surface of an untested contact block is presented in Figure B.0.1, which shows an Ra value of 0.8 µm. After the surfaces

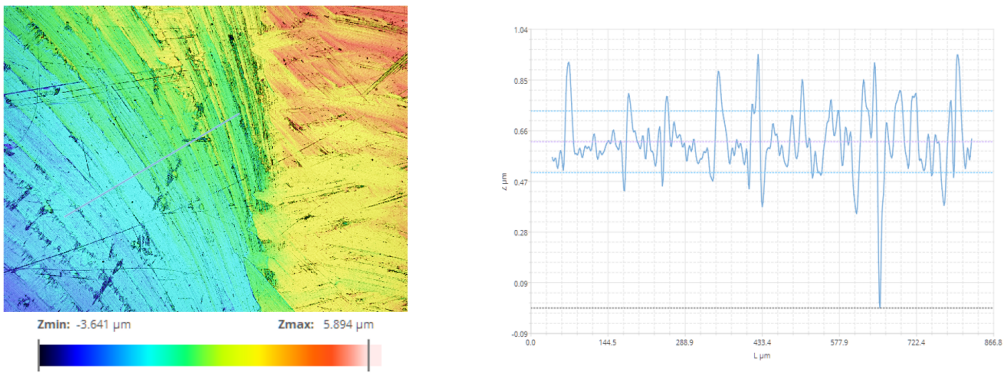

(a) Topology of an untested surface

(b) Roughness profile of a machined surface

Figure B.0.1: Surface profile of an untested surface

have been tested for contact properties, large wear scars were present on the surface. This is due to the misalignment of the specimens during testing, which results in a point or line contact that experiences significant fretting. The overall roughness of the surface thus does not change, but large cavities are formed, as is also illustrated in Figure B.0.2.

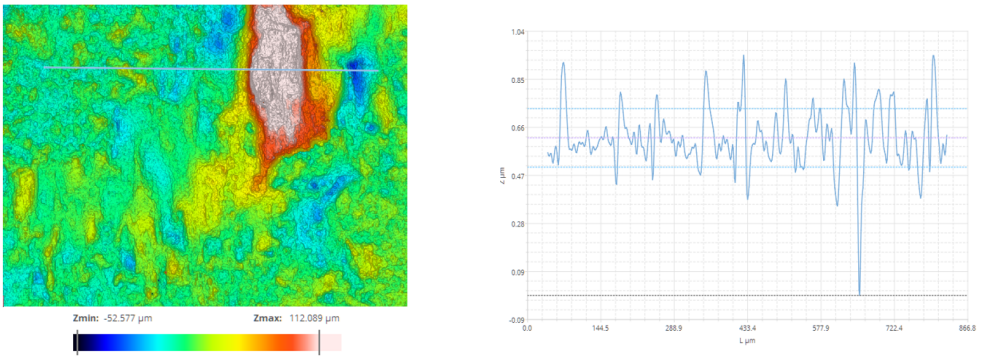

(a) Surface topology of a tested surface

(b) Roughness profile of tested surface

Figure B.0.2: surface profile of tested surfaces

Appendix C

Reliability matrix

			Frequency											
Volt	**Load [N]**	**Area [mm²]**	**15**	**27**	**39**	**51**	**63**	**75**	**87**	**99**	**111**	**123**	**135**	**147**
0.6	9	418.9												
1.2	9	418.9												
1.8	9	418.9												
0.6	18	418.9												
1.2	18	418.9												
1.8	18	418.9												
0.6	36	418.9												
1.2	36	418.9												
1.8	36	418.9												
0.6	9	837.8												
1.2	9	837.8												
1.8	9	837.8												
0.6	18	837.8												
1.2	18	837.8												
1.8	18	837.8												
0.6	36	837.8												
1.2	36	837.8												
1.8	36	837.8												
0.6	9	1256.6												
1.2	9	1256.6												
1.8	9	1256.6												
0.6	18	1256.6												
1.2	18	1256.6												
1.8	18	1256.6												
0.6	36	1256.6												
1.2	36	1256.6												
1.8	36	1256.6												

Figure C.0.1: Reliability score for the experimental data

Appendix D

Details Finite Element Model

Mesh and contact definition

For the FEM model constructed to determine the static and dynamic behaviour of the proposed testing setup, various elements are used. Most commonly used elements are SOLID186 and SOLID187. An illustration of both is presented in Figure D.0.1. Element SOLID186 is a higher order 3D 20-node

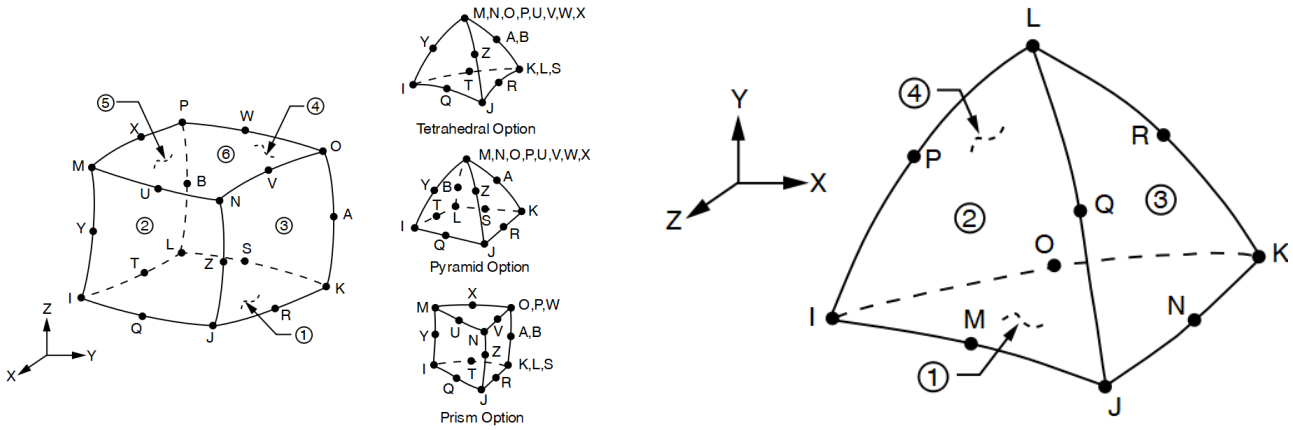

(a) Geometry of SOLID186

(b) Geometry of SOLID187

Figure D.0.1: Elements used in Finite Element Model

solid element that exhibits quadratic displacement behaviour [31], making it a suitable element for the loading conditions present within the model. Element SOLID187 is a comparable, higher order 3D 10-node element with similar quadratic displacement behaviour. Due to the geometry of the element it is well suited to model irregular meshes, which was necessary after the mesh refinement and the geometry of the model. To model the contact surfaces a combination of both CONTA174 and TARGE170 elements are used, which are typically used to represent contact and sliding behaviour [31]. Each contact was defined as a multiple point constraint, and the status of each contact is presented in Figure D.0.2.

The final mesh consisted of 556113 nodes and 331133 elements. An illustration of the final mesh is presented in Figure D.0.3.

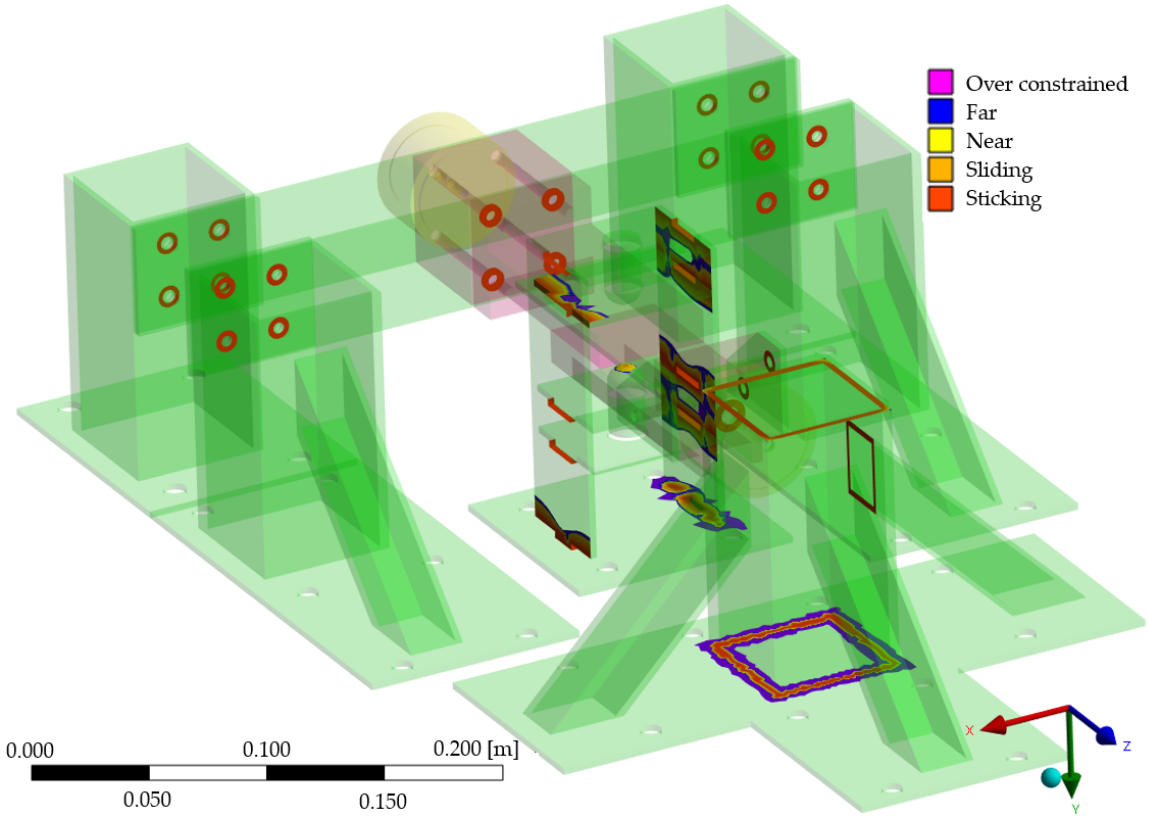

Figure D.0.2: Status of each contact within the model

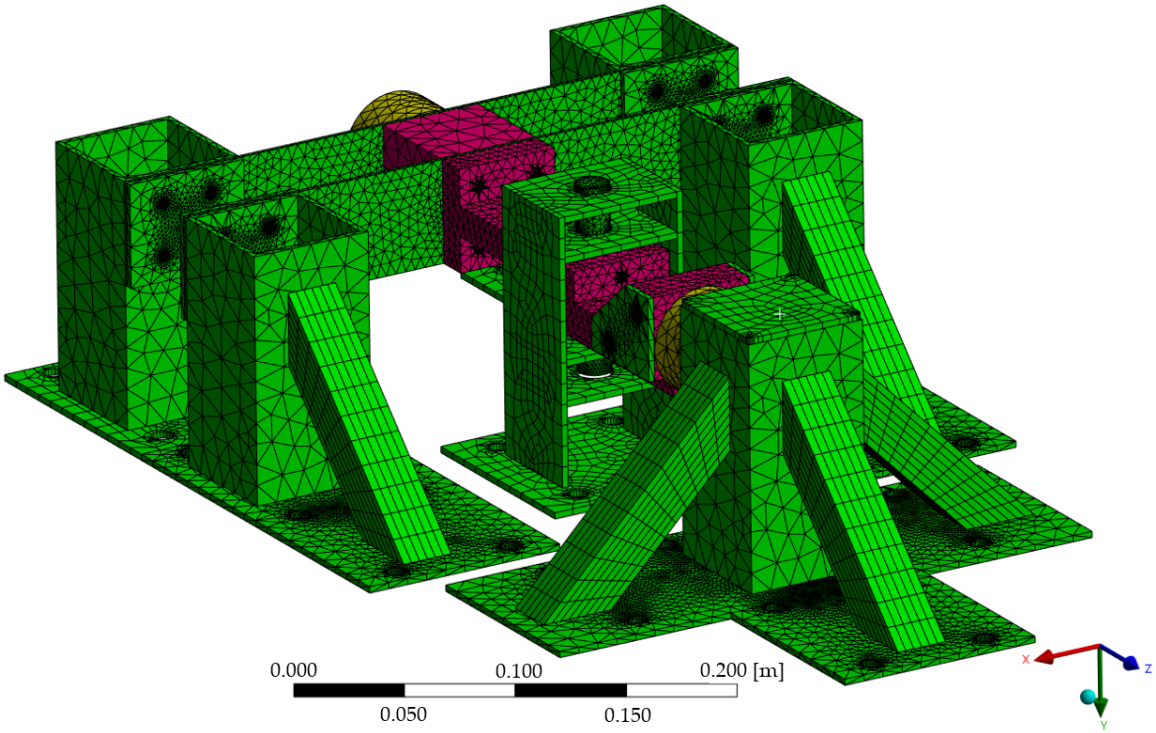

Figure D.0.3: Final created mesh

Modal participation factor

To determine how each identified mode of the system affects the movement of the system over a specific frequency range, the participation factor and effective mass of each mode in the separate global axis provide an insight how much energy is present in the mode. The participation factor for the first eight modes are presented in Table D.1, Table D.2 and Table D.3 in x, y and z direction respectively.

Table D.1: Participation factor in x-direction

Mode	Frequency [Hz]	Partic. Factor	Effective mass [kg]
1	118.3	0.10900E-04	0.118813E-09
2	246.9	0.69713	0.485991
3	344.5	0.74035	0.548116
4	356.6	0.57568E-02	0.331411E-04
5	365.6	0.51167	0.261803
6	461.5	0.59075E-02	0.348987E-04
7	539.1	1.2658	1.60228
8	707.1	-1.5653	2.45014

Table D.2: Participation factor in y-direction

Mode	Frequency [Hz]	Partic. Factor	Effective mass [kg]
1	118.3	-0.27551E-02	0.759066E-05
2	246.9	-0.32715E-02	0.107026E-04
3	344.5	-0.39446E-02	0.155602E-04
4	356.6	-0.15401E-01	0.237177E-03
5	365.6	-0.14687E-02	0.215711E-05
6	461.5	1.2477	1.55680
7	539.1	-0.11427E-02	0.130583E-05
8	707.1	0.15226E-03	0.231823E-07

Table D.3: Participation factor in z-direction

Mode	Frequency [Hz]	Partic. Factor	Effective mass [kg]
1	118.3	1.4207	2.01842
2	246.9	-0.34588E-02	0.119630E-04
3	344.5	0.19372E-02	0.375272E-05
4	356.6	-0.85100E-01	0.724209E-02
5	365.6	0.37625E-03	0.141563E-06
6	461.5	-0.11546	0.133306E-01
7	539.1	0.26173E-03	0.685049E-07
8	707.1	-0.22899E-02	0.524357E-05

From the effective mass in each direction for each mode, it is clear that the first mode predominantly moves the system in z-direction, which is a logical conclusion following from the design of the system. Another example from this data is that it shows that for mode two and three most energy is used to excite the system in x-direction. A similar approach can be used to extract and describe the movement of the system in rotation around the global x, y and z- axis.